Study of degradation and damage in a pearlitic steel rail during cyclic grinding maintenance and subsequent wheel-rail contacts.

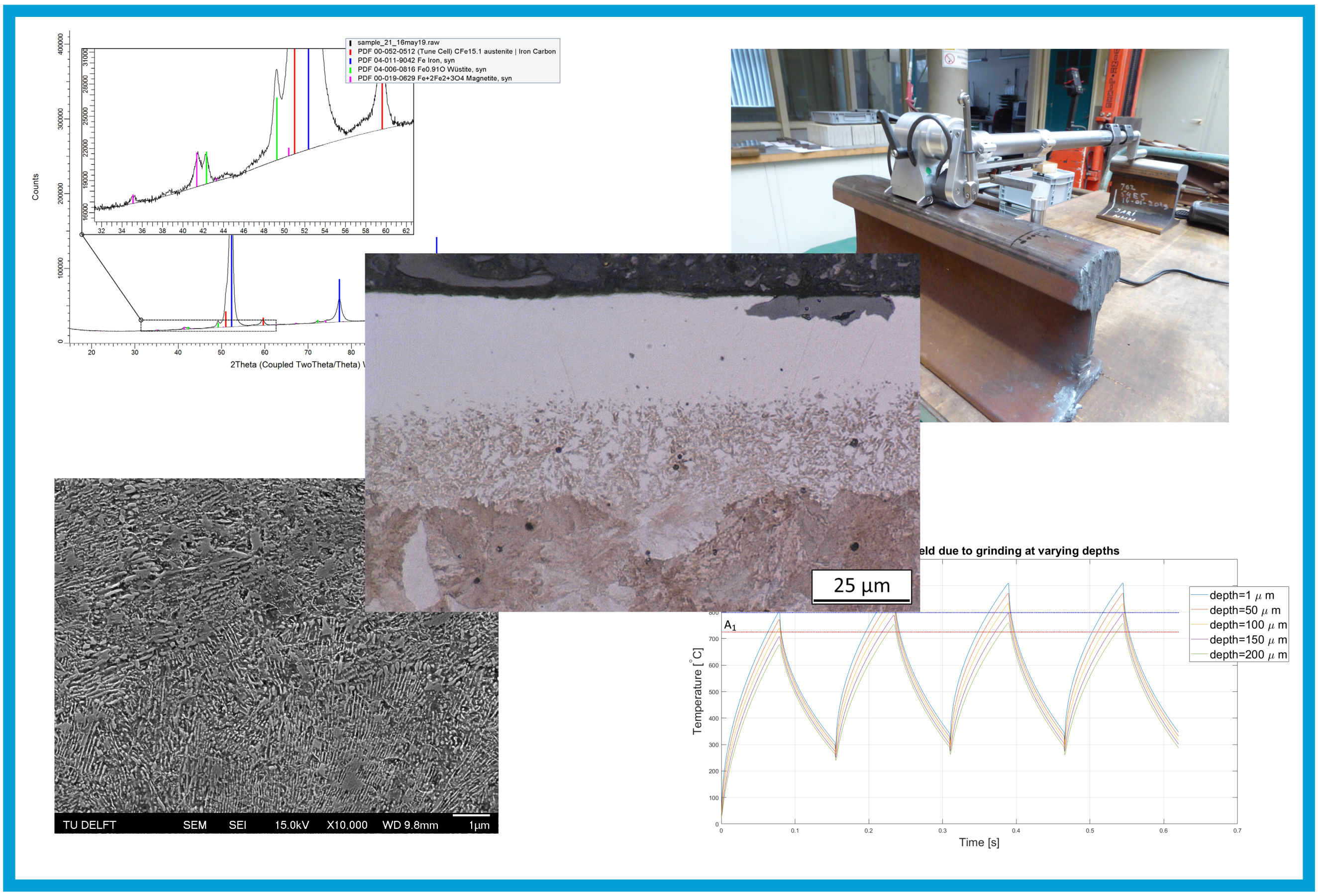

Jari Boesten

Study of degradation and damage in a pearlitic steel rail during cyclic grinding maintenance and subsequent wheel-rail contacts.

Jari Boesten
Student number: 4359127
Date: 25^{th} of November 2019

Thesis

submitted in partial fulfilment of the requirements for the degree of:

Master of science

in

Material Science and Engineering,
Specialization: Materials in Engineering Applications

Thesis Committee:
Chair: Prof. Dr. Ir. J. Sietsma
University supervisor: Dr. Ir. A. Kumar
Committee member: Prof. Dr. Ir. Z. Li

Department of Materials Science & Engineering
Faculty Mechanical, Maritime & Materials Engineering
Delft University of Technology
Delft, the Netherlands

Picture on cover: a selection of characterization techniques used in this study.

Acknowledgement

I would like to express my gratitude to several people, whose contribution to this work was essential for its completion. First of all, my gratitude goes to Dr. Ir. A. Kumar, who supervised the project from beginning to completion. His guidance in defining the research goals, gaining the required lab and writing skills and keeping a critical eye on the gathered results and their interpretation have been most valuable. My second thanks goes to Prof. Dr. Ir. J. Sietsma, who gave me the opportunity and facilities to work on this project. His experience and guidance have been valuable in keeping the project on the right track. Thirdly, my thanks goes to Ir. Schotsman, who provided the rail specimen to be studied and gave access to his work and experience.

Completion of this project would also not have been possible without help and guidance from all the staff at the TU Delft Material Science and Engineering labs. My gratitude goes to Mr. S. van Asperen and Mr. K. Kwakkenaar who gave training in using optical microscopy and SEM techniques. Special thanks also goes to Drs. R. Huizinga, for executing and helping in interpretating all the XRD experiments. Acknowledgement is also given to Dr. G. Agarwal for his suggestions and help regarding finite element modelling.

This project was carried out in collaboration with Dekra Rail. I would like to thanks all my colleagues for helping me to define the research objectives, sharing their critical thoughts with me, giving full access to all their facilities and resources and encouraging me to take an interest in the field of railway engineering. Special thanks goes to Mr. J. van der Stelt, who helped me in carrying out the visual and macro inspections of the rail surface. Additionally, my thanks goes to Mr. M. Linders and Dr. M. Hinsch for giving insight in wheel-rail contact interactions and Vampire ©simulations. The worlds of Dekra Rail and the TU Delft can sometimes be very different, but I have enjoyed working in both of them.

My final, and maybe greatest, thanks should go to my parents, brother and girl friend. Completing my studies would not have been possible without their support, patience and encouragement.

List of symbols and abbreviations

The following list presents the most important symbols and abbreviations used throughout this report in alphabetic order:

- 2θ= angle between the X-ray Diffraction measurement beam and specimen surface.
- α= Ferrite.
- BCC: Body Centred Cubic.
- BCT: Body Centred Tetragonal.
- BEL: Brown Etching Layer.
- γ= (retained) Austenite.
- θ= Cementite.
- DC: Dissolving Cementite.
- DC/α= Dissolving Cementite/Ferrite.
- EBSD: Electron BackScatter Diffraction.
- EDS: Energy Dispersive X-ray Spectroscopy.
- FCB: Flange Contact Band.
- FCC: Face Centred Cubic.
- FEA: Finite Element Analysis.
- GB: Ground Band.
- GC: Gauge Corner.
- CSG: Conventional Steel Grades.
- LD: Longitudinal Direction.
- M/γ=Martensite/retained austenite.
- MGT: Mega Gross Tons.
- MHH: Maximum Head Hardness.
- M_s: Martensite Starting temperature.
- NDT: Non-Destructive Testing.
- PCB: Primary Contact Band.
- PDP: Plastically Deformed Pearlite.
- RCF: Rolling Contact Fatigue.
- SC: Spheroidized Cementite.
- SCB: Secondary Contact Band.
- SDP: Severely Deformed Pearlite.
- SE: Secondary Electron.
- SEM: Scanning Electron Microscopy.
- TC: Thinned Cementite.
- TD: Transverse Direction.
- TEM: Transmission Electron Microscopy.
- VIRM II-mBvk: Verlengd InterRegio Materieel II Motorrijtuig (Extended Inter Region Train II Engine car).
- WEL: White Etching Layer.
- Wire-EDM cutting: Wire-Electrical Discharge Machining.
- XRD: X-Ray Diffraction.
- Z: Z-direction.

Abstract

Cyclic grinding maintenance of rails removes surface degradations and damages and restores the original rail profile, which deteriorated during wheel-rail contacts. Thus, cyclic grinding increases the service life of a rail and prevents catastrophic rail failure. Besides the advantages of cyclic grinding, concerns have risen that grinding itself might set favourable conditions for crack initiation during subsequent wheel-rail contacts. In this research, White Etching Layers (WEL) and Brown Etching Layers (BEL) at the running surface and sub-surface of a pearlitic Maximum Head Hardness (MHH) steel grade rail were found to have formed due to heating during grinding. A comprehensive understanding of the formation of these layers during cyclic grinding, their evolution during subsequent wheel-rail contacts and their respective microstructures has been established in this work. Additionally, the initiation and growth of cracks found at the running surface of the rail has been studied in relation to these layers, cyclic grinding and wheel-rail contacts.

WEL formed during grinding consists out of martensite, retained austenite and partially dissolved cementite. The formation of this layer increases the hardness at the rail surface from approximately 400 HV to 1000 HV. BEL is occasionally found as a stratified layer underneath the WEL. BEL consists out of martensite, retained austenite and pearlite containing partially dissolved cementite. The hardness of this layer was approximately 800 HV. Formation of the WEL and the BEL occurs due to frictional heating of the material at the rail surface above the A_1 temperature during grinding. Heating above the A_1 temperature during wheel-rail contacts after grinding is unlikely due to the insufficient amounts of wheel creepage expected at the rail specimen.

Austenite formation starts at the ferrite/cementite interface due to the high Gibbs free energy at this interface. Complete austenization occurs in the WEL, while only partial austenization occurs in the BEL. Partial austenization causes some regions of pearlite in the BEL to only partially dissolve. Carbon diffuses from the cementite into the austenite, causing the cementite to dissolve in order to maintain its carbon equilibrium concentration. The partial austenization at greater depths beneath the rail surface is explained by the temperature field induced by grinding. Heat diffuses from the rail surface into the material, causing the peak temperatures to decrease at increasing depth beneath the surface. Additionally, these temperatures are sustained for a shorter amount of time before quenching occurs. Quenching of the material after contact with the grinding stone leads to a transformation from austenite to martensite.

Grinding induces residual longitudinal tensile stresses at the rail surface. These residual tensile stresses form due to the specific volume difference between the austenite and martensite formed during the transformations. Thermal expansion and shrinkage of the material during heating by grinding and plastic deformation at the ground surfaces also aids in the creation of these residual tensile stresses. The manufacturing process of the MHH base material creates a residual compressive stress at the rail surface, which hinders the development of Rolling Contact Fatigue (RCF) cracks. Grinding thus counteracts this feature of the MHH base material. Additionally, grinding creates a high surface roughness which introduces stress concentrations at the running surface of the rail. Pitting corrosion at the rail surface enhances this effect.

The MHH base material has several effects on the formation of WEL and BEL. Firstly, the inter lamellar spacing of the pearlite in MHH is small when compared to more conventional steel grades such as R260Mn and R350HT. This small spacing increases the number of nucleation sites for austenite. Secondly, the small inter lamellar spacing of the MHH material reduces the maximum carbon diffusion length during austenization. These two aspects are expected to increase the formation of austenite in MHH when compared to R260Mn and R350HT. However, the A_1 and A_3/A_{cm} temperatures of MHH are higher than those of R260Mn and R350HT. The fraction of austenite after heating to an absolute temperature is expected to reduce for the MHH when compared to R260Mn and R350HT as a consequence of this difference in the A_1 and A_3/A_{cm} temperatures. Further research will be required to determine if the effects of the inter lamellar spacing or the effects of the difference in the A_1 and A_3/A_{cm} temperatures on the formation of austenite are more dominant. Finally, The small inter lamellar spacing of the MHH gives this material a high yield strength. Additionally, grinding induces a smaller amount of plastic deformation into the rail material than wheel-rail contact. Thus, only in a few cases does plastic deformation aid the formation of the studied WEL and the dissolution of cementite.

The cementite in the studied WEL and BEL has several morphologies. WEL formed due to grinding shows thinning of the original cementite, due to the thermal dissolution of this phase. The cementite dissolves to an

increasingly larger extent at decreasing depths below the rail surface, since higher peak temperatures and longer heating times are induced here by grinding. Heat induced by subsequent repeated wheel-rail contacts spheroidizes the residual cementite in the WEL. Additionally, heating during wheel-rail contacts tempers the WEL at the rail surface, reducing its hardness down to 850 HV. This tempering most likely occurrs due to the diffusion of carbon from the martensitic lattice to defects sites. The formation of new carbides and growth of the residual spheroidized cementite aids in the tempering process.

Additional effects of wheel-rail contacts after grinding are observed. Firstly, the residual longitudinal tensile stresses induced by grinding reduces due to the tempering of the martensitic WEL, removal of material at the rail surface by wear and large compressive stresses induced by the weight of the train. Secondly, the high surface roughness created by grinding and pitting corrosion are removed due to wear. Thirdly, complete spallation of the WEL induced by grinding occurs at the most severely wheel loaded section of the running surface. Fourthly, large plastic deformation of the material at the rail surface causes the initiation and growth of cracks due to ratcheting. Finally, the initial stages of mechanically induced WEL formation are observed at the most severely wheel loaded section of the running surface. The cementite of the original pearlite dissolves via thinning and fragmentation. It is expected that further wheel loading of this material will lead to a layer of nanostructured ferrite with carbon mainly facilitated at defects sites in the lattice.

Finite element modelling is used to gain insight into the spallation of WEL from the rail surface during wheel-rail contact. The yield strength of the WEL is approximately a factor 2 higher than the yield strength of the base pearlite. The WEL will experience a limited amount of plastic strain during wheel loading, while a peak in plastic strain exists in the base pearlite at the WEL/pearlite interface. Repeating wheel-rail contacts thus leads to the formation of RCF cracks at this interface, leading to the spallation of the WEL. Stratified layers of WEL, BEL and base pearlite did not show RCF crack formation at their interfaces. The BEL accommodates parts of the stresses that were previously accommodated by the WEL or base pearlite. As a consequence, the plastic strain of the pearlite is reduced. Thus, the probability of RCF crack formation at the pearlite interface reduces by the addition of a BEL.

Cracks initiated at the rail surface initially grow at a constant angle with the running surface, in the direction of the largest stress induced by wheel-rail contact. At a later stage, cracks bend towards the running surface and branch due to a changing stress field at increasing distance from the wheel-rail contact point. Oxide inside the crack indicate that water was present in these cracks during their growth. This water reduces the friction between the crack flanks, increasing the crack growth rate and the probability of branching.

Contents

Chapter 1: Introduction

1.1 The social importance of minimizing damages in rails

The railways are an essential part of the infrastructure in the Netherlands; transporting 1.3 million people daily [77] and experiencing an annual growth in passengers numbers of 2% [27, p. 40]. Thus, it is expected that the number and velocity of trains on the Dutch railway networks will increase over the coming years. An example of this is the political ambition to increase the number of trains per hour between the nine largest Dutch cities from four to six [51]. High performances of the rail infrastructure are required to accommodate this increase in traffic density. An important aspect of this performance is maximizing the rail life time, while also minimizing maintenance time and costs.

The life time of a rail is mainly determined by wear accumulated on the running surface of the rail head and plastic deformation of heavily loaded sections of track [2]. Additionally, Rolling Contact Fatigue (RCF) caused by repeating wheel-rail contacts can lead to the formation of cracks at the running surface of a rail [2, 55]. When left unattended, these cracks can grow and significantly reduce the life time of a rail [2, 67] by causing sudden rail failure and thus threatening passenger safety [55]. High hardness rail steel grades have been developed to reduce these degradation mechanisms, leading to an increase of rail service life [2]. A further increase in service life can be achieved by implementing cyclic grinding maintenance regimes.

Cyclic grinding maintenance removes RCF damages and restores the rail profile by removing material from the top of the rail. However, concerns have risen that grinding might set conditions which are favourable for the development of RCF cracks [58, 63, 67]. It is mentioned that grinding induces a high surface roughness, which can act as stress concentrations [63]. Furthermore, crack initiation at locations of thermally induced surface stresses are reported [63]. Special attention has been given to layers of transformed base material at the rail surface and subsurface, known as White Etching Layers (WEL) and Brown Etching Layers (BEL) [58, 63, 67]. These hard and brittle layers are often associated with crack initiation in the surrounding base material [4, 32, 62, 67] and thus a reduction in rail service life. The formation of WEL is traditionally related to heat input and plastic deformation during wheel-rail contact. However, the role of grinding in the formation of WEL is so far poorly understood and requires further investigation.

1.2 Aim and structure of the report

This study considers WEL, BEL and regions of plastic deformation which have formed during cyclic grinding maintenance of a rail. The formation mechanism during grinding, resulting microstructure and evolution during subsequent wheel-rail contacts of these layers are discussed. Several RCF cracks were observed on the running surface of the rail. The initiation and growth mechanism of these cracks in relationship to the grinding maintenance, wheel-rail contact and WEL, BEL and plastic deformation is investigated. The studied rail specimen was fabricated out of Maximum Head Hardness (MHH) steel grade. The influence of this steel grade on grinding maintenance, WEL and crack initiation is still largely unknown and thus requires further investigation. The goals of this research can thus be summed up as follows:

- Understand the relation between the microstructure and the mechanical properties of the MHH base material, regions of plastic deformation, WEL and BEL.
- Understanding the formation mechanisms of the WEL, BEL and regions of plastic deformation.
- Understand how the microstructure of the MHH base material affects the formation process, microstructure and properties of the WEL, BEL and regions of plastic deformation.
- Understand how wheel-rail contacts affect the WEL, BEL and regions of plastic deformation after their formation.
- Understand how damage initiation and growth is related to RCF, WEL, BEL and regions of plastic deformation.

The structure of this report is as follows. Firstly, the results of a literature review will be briefly presented in chapter 2. This research discusses the pearlitic rail steels, the microstructure and formation process of WEL and BEL, the basic mechanics of wheel-rail interactions, grinding maintenance and the relationship between WEL and common RCF damages.

Secondly, chapter 3 presents the history of the available rail specimen and the methods used in its characterization. The rail specimen was removed due to the detection of RCF damage shortly after cyclic grinding maintenance. The rail was fabricated out of MHH steel grade. Previous metallographic investigation related the surface conditions after grinding to the initiation of cracks during subsequent wheel-rail contacts [63]. Additionally, the presence of WEL was determined [63]. The rail sample will initially be characterized on a macro scale via visual inspection and measurements of the surface micro roughness, surface hardness and the rail profile. Further metallographic examination will be done to characterize the MHH base material, cracks and any WEL, BEL and plastic deformation present at the rail surface. Optical microscopy, Vickers microhardness, SEM, EDS and XRD will be used during this characterization.

Thirdly, the results of each experiment will be presented in chapter 4. Additionally, Thermo-calc©simulations will quantify the properties of the MHH steel grade. Fourthly, chapter 5 will discuss the results presented in 4 to answer the proposed research questions. Additional simulations on the wheel-rail interactions at this specific rail specimen, temperature field during grinding and mechanical behaviour of stratified layers of WEl, BEL and base pearlite will further enhance the understanding of the microstructural evolution of these layers. The appendices in chapter A1 will discuss these simulations in more detail. Finally, chapter 6 will give a brief summary newly generated knowledge and point out where further research can still be done.

Chapter 2: Literature Review

This literary research aims to introduce the reader to degradation mechanisms in rail materials by discussing a number of subjects. Firstly, the properties, microstructure and manufacturing process of pearlitic rail steel grades will be discussed. Emphasis will be put on the MHH steel grade. Additionally, the most important phase transformations in the $Fe - C$ system will be presented. The second part of the literature review will discuss the properties, microstructure and formation process of WEL. A distinction will be made between the thermal and mechanical aspects of WEL formation. The properties and microstructure of BEL, a layer occasionally found in combination with WEL, will also be discussed. Thirdly, the basic mechanics of wheel-rail interactions and cyclic grinding maintenance will be investigated, since both of these loading types are believed to cause WEL and BEL formation. Finally, damage initiation mechanisms observed at WEL and the most common RCF damages found at rail surfaces are discussed. This will give the reader an overview of the detrimental effects of WEL and RCF at the running surface of a rail.

2.1 Pearlitic rail steel grades

Over the years, multiple rail steel grades have been developed to reduce the effects of degradation mechanisms such as wear, plastic deformation and RCF at the running surface of the rail [2]. It is thus important to understand which chemical alloying elements, microstructural features and manufacturing steps give these steels their mechanical properties. Additionally, these microstructures can be transformed into WEL and BEL under the influence of mechanical and thermal loading during the service life and maintenance of the rail. Understanding the microstructures of these steel grades thus gives a good starting point in understanding the formation process of WEL.

Table2.1 shows the chemical composition, mechanical properties and usage of the most common rail steel grades on the Dutch network [12, p. 20] [75, p. 43]. This research will focus on damage phenomena in a MHH steel grade rail, which falls under the R370CrHT grade. While the other steel grades have a pearlitic hypo-eutectoid microstructure, this grade has a hyper-eutectoid chemical composition.

Table 2.1: *The chemical composition, mechanical properties and usage of the most common rail steel grade on the Dutch network. Information is taken from [12, p. 20] and [75, p. 21]*

.

Steel grade	**Composition [wt.%]**						**Rm [MPa]**	**ε [%]**	**Running surface HBW**	**Curve radius [m]**
	C	Si	Mn	P max.	S max.	Cr				
R260	0.60 to 0.82	0.13 to 0.60	0.65 to 1.25	0.03	0.030	<0.15	880	10	260 to 300	>3000
R260Mn	0.53 to 0.77	0.13 to 0.62	1.25 to 1.75	0.03	0.030	<0.15	880	10	260 to 300	>3000
R350HT	0.70 to 0.82	0.13 to 0.60	0.65 to 1.25	0.03	0.030	<0.15	1175	9	350 to 390	<300
R370CrHT	0.68 to 0.84	0.38 to 1.02	0.65 to 1.15	0.025	0.025	0.40 to 0.60	1280	9	370 to 410	<3000

The role of the alloying elements present in table3.1 can be summed up as follows. Firstly, carbon increases the strength of the steel while also reducing its ductility [8, 21, p. 301]. Secondly, manganese, silicon and chromium allow for the formation of pearlite at a higher cooling rate. This higher cooling rate leads to a smaller inter lamellar spacing of the cementite in the pearlite, resulting in a higher strength and lower ductility [14, 59, 83, p. 11]. These elements will additionally solid solution harden the metal [14]. Finally, Sulphur and Phospor are contaminations originating from the blast furnace process. The content of these contaminations must be kept low. An additional role of the manganese is binding to the sulphur, reducing unwanted effects of this contamination [83, p. 11].

2.1.1 The microstuctural properties of MHH rail steel

MHH was specially developed to reduce wear and plastic deformation by creating a material with a high hardness [14]. This high hardness has the additional benefit that more loading cycles are required to initiate RCF cracks at the running surface of the rail. Furthermore, the manufacturing process of a MHH rail creates a small, occasional compressive, residual stresses at the running surface of the rail, as will be discussed later in the text [14]. This stress state will hinder the growth of cracks [14]. In addition, the pearlitic microstructure of the MHH contains lamellae of ductile, low carbon BCC ferrite and brittle, high carbon orthorhombic cementite (Fe_3C). Combining these two constituents gives a good balance between ductility and high hardness, improving the mechanical properties [59, 83, p. 9]. The hardness of this microstructure is further enhanced at the running surface of R350HT and R370CrHT grades rails by head hardening the rail via rapid cooling after hot rolling [21, 75, p. 17]. This treatment reduce the inter lamellar spacing of the pearlite, which increases the yield strength via the Hall-Petch relationship [59, 83, p. 11].

Several weak spots exist within the microstructure. Firstly, dislocations can pile up at the incoherent interface between non-metallic inclusions and the surrounding matrix. This can cause interface decohesion, leading to stress concentrations in the matrix [83, p. 14]. Furthermore, these non-metallic inclusions often have a different thermal expansion coefficient than the surrounding material, causing additional stresses during heat treatment of the material [83, p. 14]. Secondly, weakening of the material during heat treatment and hot rolling can occur in the form of decarburization. High temperature oxidation of carbon at 1200°C will occur more rapidly than the oxidation of iron, leading to a carbon depleted zone at the outer surfaces of the rails. This zone will show lesser mechanical properties and thus requires removal by milling [88].

2.1.2 Phase transformations in pearlitic steel

Pearlite is formed by slowly cooling FCC austenite. For MHH, cooling starts at point A in 2.1. Cementite will first form at the grain boundaries of the austenite when the A_{cm} temperature is passed (point B). The fraction of cementite keeps increasing as the material is cooled further towards the A_1 temperature. During this cooling, the carbon content in the austenite will decrease towards the eutectoid composition. The remaining austenite transforms to pearlite when passing the A_1 temperature (point C) [8, p. 128]. A higher cooling rate results in a smaller inter lamellar spacing since carbon diffusion limits the kinetics of this phase transformation [46].

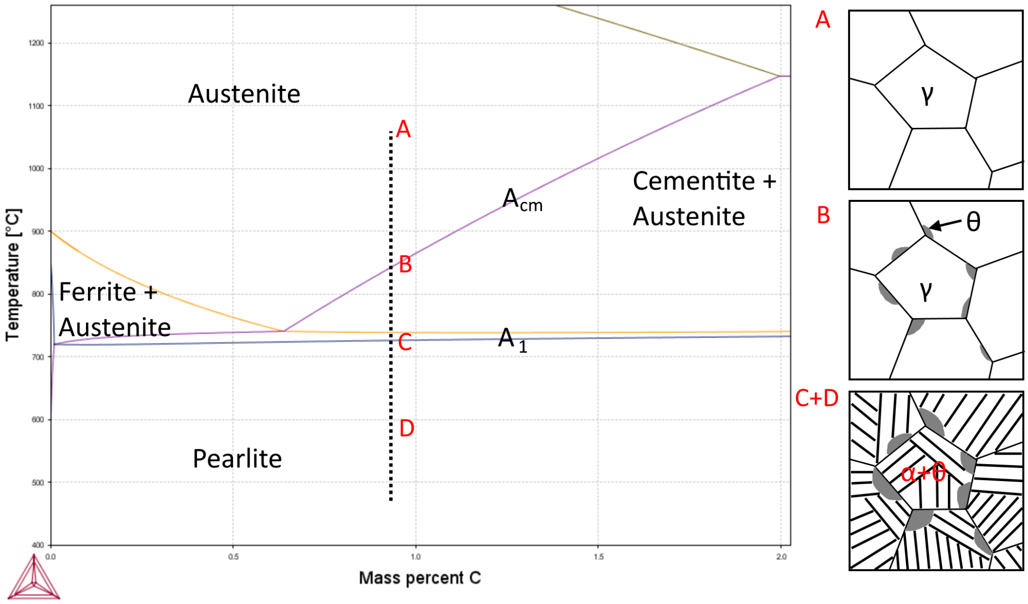

Figure 2.1: The equilibrium phase diagram of the MHH steel grade, as calculated with Thermo-calc ©. The drawing on the right schematically shows the transformation from austenite to pearlite. The phases in the schematic drawing are indicated by γ (austenite), θ (cementite) and α (ferrite).

Pearlite will only form during cooling from the austenite region if sufficiently slow cooling are maintained, for example by following cooling trajectory C shown in the CCT diagram of figure 2.2. A massive transformation via shearing is initiated if cooling from the austenite region occurs too rapidly, for example by following cooling trajectory A in the CCT diagram. This high cooling rate does not allow for the diffusion of carbon [15, p. 414]. The FCC austenite crystal is transformed to a BCC crystal with carbon accommodated at the octahedral interstitial sites [15, p. 414]. The BCC crystal has to strain to facilitate carbon, leading to a Body Centred Tetragonal (BCT) crystal [15, p. 414]. This phase is known as martensite and has brittle characteristics [8, p. 129]. A martensitic transformation will only occur at sufficient under cooling, when temperature drop below the M_s-temperature. The fraction of martensite will increase as the under cooling increases. The remaining austenite is retained in the microstructure. The M_s-temperature will decrease at increasing austenite carbon content [15, p. 414]. Several factors contribute to the brittleness of martensite. Firstly, the shear transformation from austenite to martensite causes a high dislocation density. Plasticity upon subsequent mechanical loading will remain low since the motion of dislocations is hindered by the high amount of other dislocations and interstitial carbon in the BCT lattice [15, p. 413]. Secondly, Straining of the BCT lattice is required to accommodate carbon at its octahedral interstitial sites. This, in addition to shearing during the martensitic transformation, can lead to residual stresses in the material [15, p. 418].

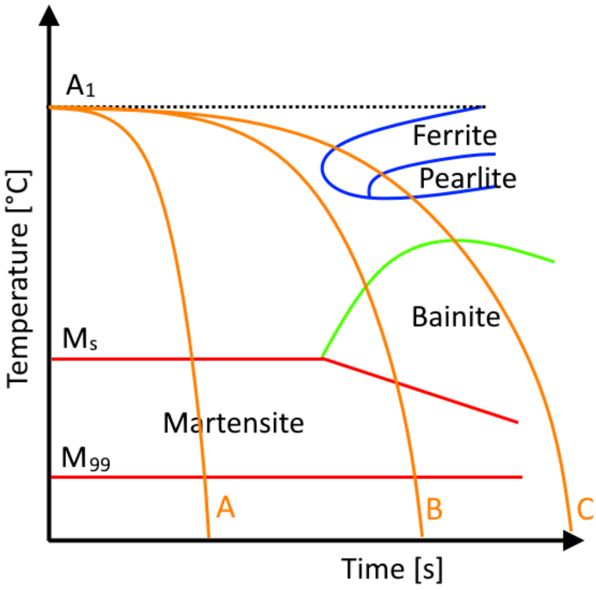

__Figure 2.2:__ A schematic CCT diagram for steel [63]. The cooling trajectories are indicated in orange, while the martensite, ferrite/pearlite and bainite regions are indicated in red, blue and green respectively. The cooling rate decreases as the cooling trajectory reaches further to the right.

2.1.3 The manufacturing process of steel rails

The rail manufacturing process of steel rails can be described in a number of steps. Firstly, hot metal is continuously cast into billets and reheated to 1250°C in a walking beam reheating furnace. Secondly, the rail is hot rolled into shape in several steps and leaves this process step at a temperature of 860°C. Thirdly, the rail is cooled to 40°C and subsequently straitened in the vertical and horizontal direction [63, 74, p. 16]. Head hardening occurs by increasing the cooling rate during this last step [21, 75, p. 17]. Different sections of the rail profile have different volume to external surface ratio's. Since cooling occurs via convection, different cooling rates will occur at each section [59]. This leads to a high compressive stress just below the running surface of the rail after head hardening [59]. However, subsequent straightening of the rail induces a large residual tensile stress at the running surface, which could aid in the growth of fatigue cracks during later wheel-rail contacts [63, p. 14].

The manufacturing process of MHH steel is modified to prevent this unwanted tensile stress at the running surface of the rail. After hot rolling, the steel is first straightened to gain the required geometrical tolerances. Subsequently, the steel is re-austenized via induction and cooled to pearlite in ambient air at a rate of 1°C/s, thus retaining the residual compressive stresses at the running surface of the rail [63, p. 14]. A high amount of process control is required to maintain geometrical tolerances during this step [14, 63, p. 15].

2.2 The properties, microstructure and formation of White Etching Layers

White Etching Layers are hard and brittle regions at the running surface of rails. Saxena et al. [62] state that WEL has a toughness of $16 \pm 1.2 MPa\sqrt{m}$, which is similar to the toughness of martensite. Kumar et al. [32] describe WEL as a semi-brittle layer with a fracture toughness of $21.5 \pm 3 MPa\sqrt{m}$ to $25.4 \pm 2.3 MPa\sqrt{m}$. The critical length for an initiated defect to propagate in the WEL is low as a result of this brittle character[62]. Thus, WEL is often described as a mechanism for crack initiation and is regarded as detrimental to the life span of rails [4, 31, 32, 67, 83, p. 15]. Furthermore, the WEL is insensitive to etching with Nital, giving it a white appearance under the optical microscope [85]. WEL's are not found in the original microstructure and thus forming during service [83, p. 15]. It is believed that two aspects play a role in the formation of WEL. Firstly, large heat inputs during wheel passage or grinding maintenance could austenize the rail material, leading to the formation of a martensitic structure when quenching follows [53, 54, 67, 83, 85]. A second aspect in the formation of WEL is the repeating plastic deformation occurring during wheel passage. This causes the dissolution of pearlite, resulting in a nanostructure of ferrite with carbon mainly facilitated at the dislocation cores [1, 39, 50]. The WEL formation process is often a hybrid of thermal and mechanical formation mechanisms [31, 85]. Thus, both types of WEL and their formation mechanisms are discussed in more detail in the following sections.

2.2.1 Thermal aspects of WEL formation

WEL induced by heating above the A_1 temperature typically has a thickness of 20 μm to 100 μm [53, 54, 85] and a hardness varying from 600 HV to 950 HV [53, 54, 85]. The hardness is occasionally found to increase with increasing depth and peaks at the boundary between the WEL and base pearlite. This suggest that tempering of the layers has occurred during wheel passage [85]. The WEL is further characterized by a sharp boundary between the base pearlite and the WEL, indicating that the temperature field only surpassed the austenization temperature above this boundary [54, 89]. Figure 2.3a shows a typical example of this type of WEL [54]

Further evidence that the WEL was formed by austenization and subsequent quenching can be found when looking at the phases present in the WEL. A combination of martensite, retained austenite, ferrite and cementite is detected in the WEL [53, 85]. The presence of austenite in the WEL indicates that heating above the A_1 temperature occurred. However, the A_3 temperature was not always surpassed, thus retaining some of the original ferrite or cementite in the WEL. Subsequent quenching causes the existing austenite to partially transform to martensite. A tetragonallity is often found in the lattice of this martensite, indicating that carbon is facilitated at the octahedral interstitial sites [15, 53, 85]. Wu reported additional carbon peaks up to 9.5 at.%, indicating that carbon is facilitated at additional locations in the microstructure [83, p. 57]. Firstly, The carbon has a high interaction energy with dislocations and can thus be facilitated here [31, 83]. Secondly, the carbon can be facilitated in the retained austenite present in the WEL [83, p. 57]. Thirdly, grain boundaries in the WEL can facilitate carbon [83, p. 57]. Kumar at al. mention that removal of the carbon from the martensite can soften the martensitic martix, leading to semi-brittle behaviour of the WEL [32]. However, the fraction of both retained austenite and the grain boundaries is believed to be to low to explain all the carbon peaks [83, p. 57]. Carbon rich zones in the WEL at locations of the original cementite lamellae are thus a fourth location at which carbon is facilitated [83, p. 57]. However, the carbon concentration in these zones was lower than the cementite carbon equilibrium concentration of 25 at.%, indicating that a fraction of the carbon has diffused out of the cementite [83, p. 57]. Finally, the measured carbon peaks can only be fully explained by the accommodation of carbon by martensite twins [83, p. 57]. Carbon in the WEL can further be accommodated at dislocations, twins, grain boundaries and retained austenite or cementite [83, p. 57].

The transformation for pearlite to austenite is an important step in the formation of WEL. During heating, austenite will nucleate at the ferrite-cementite boundary and grow into the surrounding microstructure [5, 36]. A sharp carbon concentration gradient exists at the cementite-austenite interface. Carbon will diffuse from the cementite to the austenite to reduce this gradient [34]. As a consequence, cementite dissolutes to maintain its carbon equilibrium concentration [34]. Thus, carbon diffusion from the cementite into the austenite is the rate limiting aspect of the austenite transformation [34]. A smaller inter lamellar spacing of the pearlite will reduce the maximum distance that carbon has to diffuse. Thus, decreasing the lamellar spacing will increase the austenite growth rate [36]. Chromium, present in MHH, is expected to be mainly facilitated in the cementite and to stabilize this phase [34, 36, 37]. As a consequence, the presence of chromium in the MHH steel grade can increase the A_1 temperature.

A point of debate is whether austenization temperatures are reached during wheel-rail contact [53], since this would require large amounts of creepage [47]. However, the forces exerted by the wheel on the rail can aid in austenizing the material. The weight of the train will cause a compressive stress at the rail surface, lowering the austenization temperature [53]. Furthermore, plastic deformation of the pearlite during wheel-rail contacts can aid in the cementite dissolution, increasing the rate of austenization as discussed in the next section.

2.2.2 Mechanical aspects of WEL formation

WEL induced by mechanical loading usually has a thickness of 10 to 50 μm and a hardness ranging from 700 HV to 1200 HV [1, 39, 50]. Figure 2.3b shows this type of WEL [4]. A region of plastically deformed, hardened, pearlite exists under the WEL [4]. The WEL itself is described as a region where grain refinement of ferrite has taken place, resulting in a nanostructure of ferrite [1, 39, 50]. Lojkowski et al. [39] describe the dissolution of the original cementite lamellae due to plastic deformation. The mechanisms for this dissolution will be discussed in the next paragraph. Only a limited amount of carbon from the cementite can be facilitated in the lattice of the ferrite [39, 89]. This gives the ferrite phase a close resemblance to martensite [39, 89]. Additional carbon is facilitated at the dislocation cores [1, 39, 50, 89]. Mechanically induced WEL has a high dislocation density and large misorientation between the nano scale ferrite grains [1]. Dislocations in this WEL are immobile due to pinning by carbon, numerous grain boundaries in the ferritic nanostructure and other dislocations [89].

The mechanisms of cementite dissolution during mechanical loading are not fully explained yet. however, several mechanisms are suggested in the literature. Firstly, plastic deformation creates vacancies in the ferrite, which can facilitate carbon from the cementite due to a high interaction energy between the vacancy and carbon atom (0.85 eV/atom [31]) [72]. Secondly, plastic deformation of the softer ferrite leads to strain incompatibilities with the harder cementite, leading to the fragmentation of this carbide [22, 31]. The smaller cementite particles become unstable due to the Gibbs-Thomson effect and will thus dissolute [22, 33, 61, 72]. The Gibbs-Thomson effect describes that a smaller particle will have a higher interface area per unit of volume, increasing its Gibbs free energy [72]. This gives the particle a large driving force for dissolution [31]. Fragmentation occurs via thinning, fragmentation or cutting by moving dislocations during plastic deformation [6, 22, 31]. Thirdly, the interaction energy between a dislocation and a carbon atom is larger than the interaction energy between cementite and a carbon atom (0.85 eV/atom and 0.5 eV/atom respectively [31]). Thus, it is favourable for the carbon to be facilitated at the dislocation instead of the cementite [31]. Fourthly, dislocations pile up at the cementite during the plastic deformation of the ferrite and can provide a fast diffusion path for carbon from cementite into the ferrite [31, 39, 72]. Additionally, dislocations moving due to plastic deformation can cut a cementite particle. The favourable interaction energy between the dislocation and carbon causes the carbon to be dragged along by the dislocation, transporting it into the ferrite matrix [49]. Finally, a balistics model describes the ferrite as visco-elastic compared to the hard cementite. During plastic deformation, ferrite erodes parts of the cementite away [22].

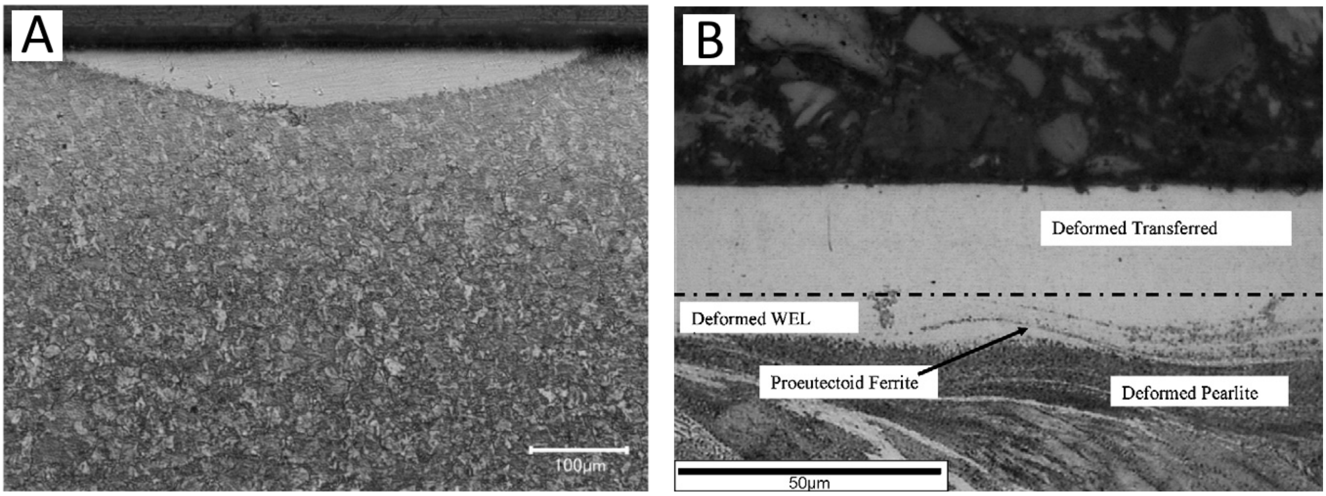

Figure 2.3: *(a): A thermally induced WEL captured via optical microscopy. The white layer indicates the insensitivity of WEL to etching with Nital. Figure is taken from [54]. (b): A mechanically induced WEL with deformed pearlite underneath. The deformation causes work hardening, grain refinement of the ferrite and dissolution of the cementite. Figure is taken from [4].*

.

2.2.3 Brown Etching Layer

Brown Etching Layers (BEL) occasionally forms as a stratified layer under the WEL [70, 73, 83]. BEL has a hardness between 500 HV and 700 HV [70, 83]. The microstructure and formation process of BEL are still a source of debate in the literature. Wu states that BEL contains martensite, austenite and partially dissolved cementite [83, p. 116]. The cementite follows the same orientation as the cementite lamellae of the original pearlite [83, p. 116]. Cracks might grow from the BEL into the base pearlite along these lamellae, enhancing crack growth into the base pearlite [83, p. 116]. Wu also states that BEL can be formed due to a temperature increase above the A_1 temperature and rapid subsequent cooling, leading to martensite [83, p. 119]. Additionally, plastic deformation contributes in the formation of BEL, but plays a less significant role than the thermally induced phase transformation [83, p. 119].

Kumar et al. [31] present to different theories for the formation of BEL. Firstly, it is suggested that cementite dissolutes under the influence of plastic deformation and heating below the A_1 temperature. Subsequent heating above the A_1 temperature leads to partial austenization. After quenching a mixture of martensite, retained austenite, ferrite and partially dissolved cementite makes up the microstructure of the BEL [31]. A second mechanism describes the dissolution of cementite and formation of austenite under the influence of plastic deformation and heating above the A_1 temperature [31]. A microstructure with martensite, retained austenite, carbon enriched ferrite and partially dissolved cementite is formed after subsequent quenching [31]. Heating during subsequent wheel-rail contacts only reach the martensite tempering regime [31]. This causes the formation of secondary carbides, which reduces the hardness of the BEL [31].

Steenbergen et al. [70] state that BEL has a bainitic structure with patches of globular cementite and that the hardness of the layer depends on the fraction of each of these phases. However, the presence of bainite in BEL seems unlikely. The schematic CCT diagram of figure 2.2 indicates that long cooling times are required to form this phase. It is unlikely that these can be achieved during the short duration of wheel-rail contact.

2.3 Service conditions associated with WEL formation

The formation of WEL is often associated with wheel loading and cyclic grinding maintenance of the running surface. Both types of loading are discussed in this section of the text.

2.3.1 Interactions between the wheel and rail

A hertzian contact model still forms the basis for describing the interactions between the wheel and rail on a fundamental level [11, 66]. More extensive models describes the shape and size of the contact patch, the compressive stress on the rails due to the weight of the train and the traction forces that can be transferred between the wheel and rail [11, 66]. The weight of the train induces a compressive stress field that has a parabolic shape and mainly depends on the curvature of the two bodies and the applied force [11, 66], as shown in figure 2.4a [47]. Traction applied to the rail via the contact patch causes an additional shear stress component. This shear stress partially follows the parabolic shape of the compressive stress [47, 87]. The shear stress starts at zero at the leading edge of the wheel-rail contact patch and increases to a maximum [47, 87]. Subsequently, shear stress reduces again to zero at the trailing edge of the wheel-rail contact patch[47, 87], as shown in figure 2.4b [47, 87]. A part of the contact area is in adhesion, while the remaining part is in slip. This is schematically shown in figure 2.6b. The ratio between these two parts depends on the friction coefficient between the wheel and rail and influences the amount of traction that can be transferred from the rail to the wheel.

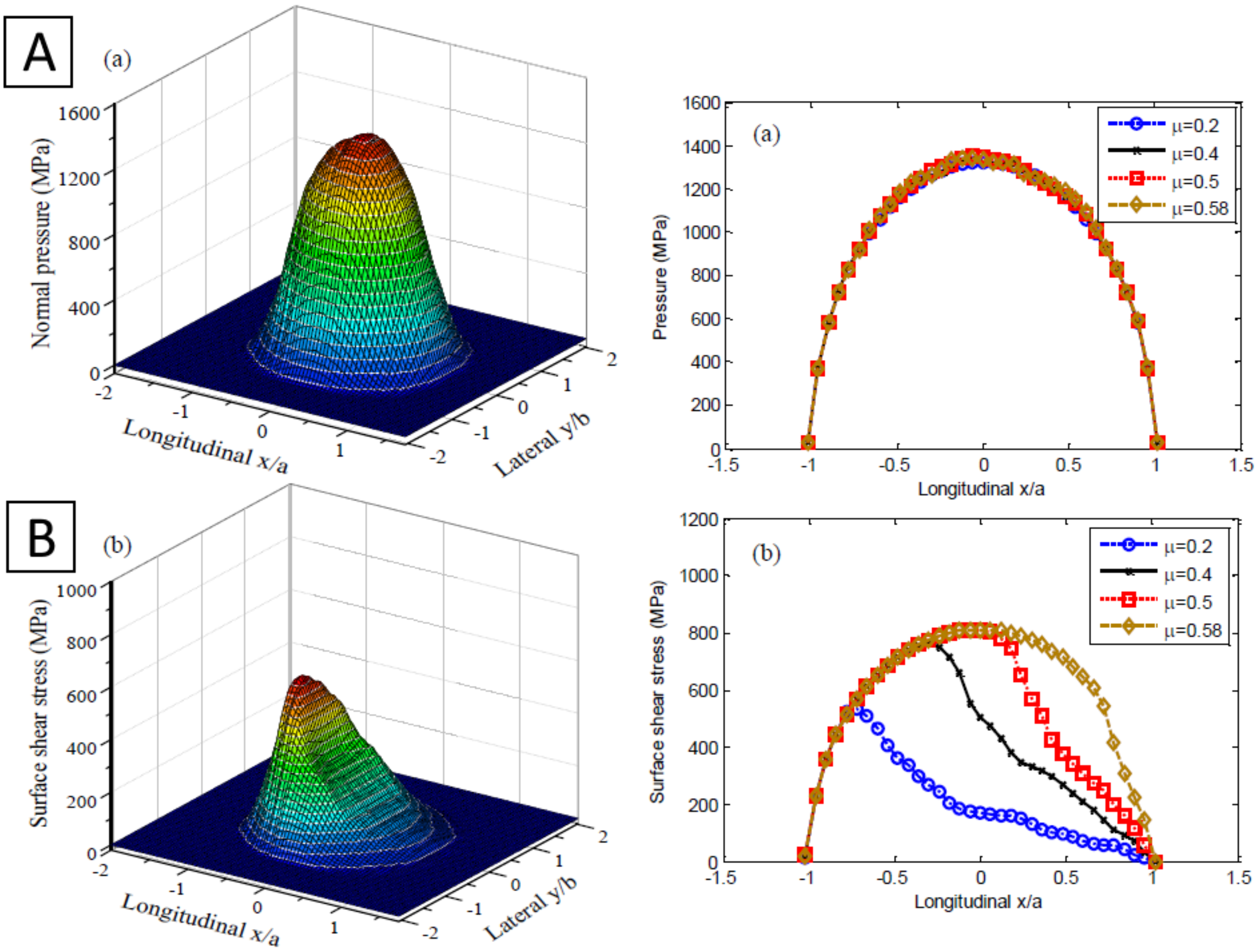

Figure 2.4: *The calculated stresses in the contact area of the wheel rail contact point. (a): The contact pressure due to the weight of the vehicle as a function of friction coefficient. (b): The shear stress created due to wheel creepage at different friction coefficients. The bottom left side figure shows the shear stress field at a friction coefficient of 0.2. Figure is taken from [47].*

Creepage will induces shear stress and frictional heat into the rail surface [47, 87]. The temperature profile follows the shear stress profile, as seen when comparing figure 2.4b and 2.5. Figure 2.5 shows a maximum temperature increase of 311°C at a friction coefficient of 0.58. Extrapolating the data shows that a creepage of 2.4% is needed to allow for a temperature increase of 600°C during wheel contact [47]. Naeimi et al. [47] state that this temperature increase is sufficient to put the material in the austenization region, considering the large compressive stresses present in the material at the moment of wheel-rail contact. The amount of creepage depends on parameters like the weight and motion of the train [47]. High values of creepage are only expected when breaking of the train occurs, allowing for temperature increases that would make austenization likely [47].

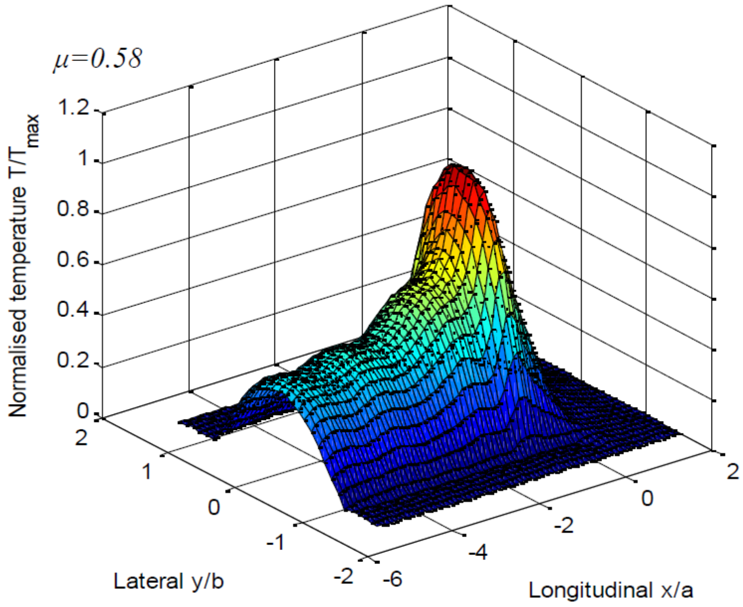

Figure 2.5: *The normalized temperature field in the contact area between the rail and wheel. The value of T_{max} was found to be 311 °C; the maximum calculated temperature in this simulation. Figure is taken from [47].*

Two contact points between the wheel and the rail are expected in the upper leg of a curve. Point A is the primary contact point and supports the weight and traction forces of the train. The exact location of this point depends on the amount of lateral displacement of the train, caused by the inertia of the train while travelling through the curve and possible lateral oscillation of the train. Point B in figure 2.6a shows the contact between the wheel flange and the gauge side of the rail. This contact point prevents derailment and the rail and will only be created at a large lateral displacement of the train [18]. Wear of the rail and wheel profile can change the shape, size and location of the contact points or even create extra contact points [18].

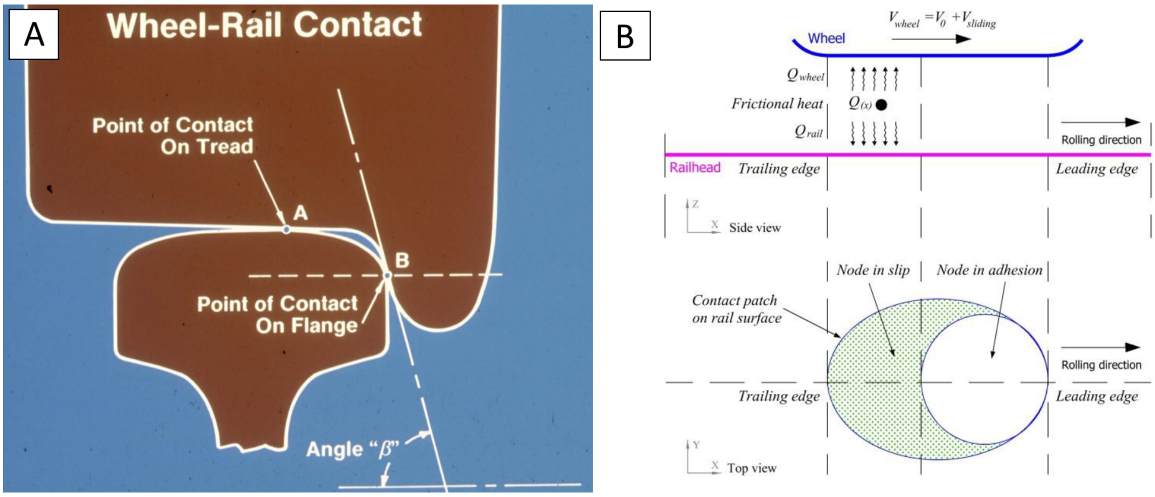

__Figure 2.6:__ (a): A schematic view of the contact points between a wheel and a rail. The current situation shows two contact points between the rail and the wheel. This situation occurs when considering the upper rail in a curve. Figure is taken from [18]. (b): The contact area between the wheel and rail is schematically shown. The part of the contact area that is in creepage accommodates the heat transfer. Figure is taken from [47].

2.3.2 Grinding maintenance of rails

Grinding maintenance removes material from the top of the rail via the abrasive action of rotating ceramic stones. These stones are suspended from the underside of a train and are pressed against the rail surface while the train moves along the rails at a constant speed. By applying multiple stones on multiple sections of the rail surface, a polygon approaches the original rail profile. This covers the rail surface in facets and grinding marks. These marks are repeated every few centimeters, due to the rotating action of the stones[58, 67]. Figure 2.7 schematically shows the grinding process and the surface features left on the rail surface by this maintenance process.

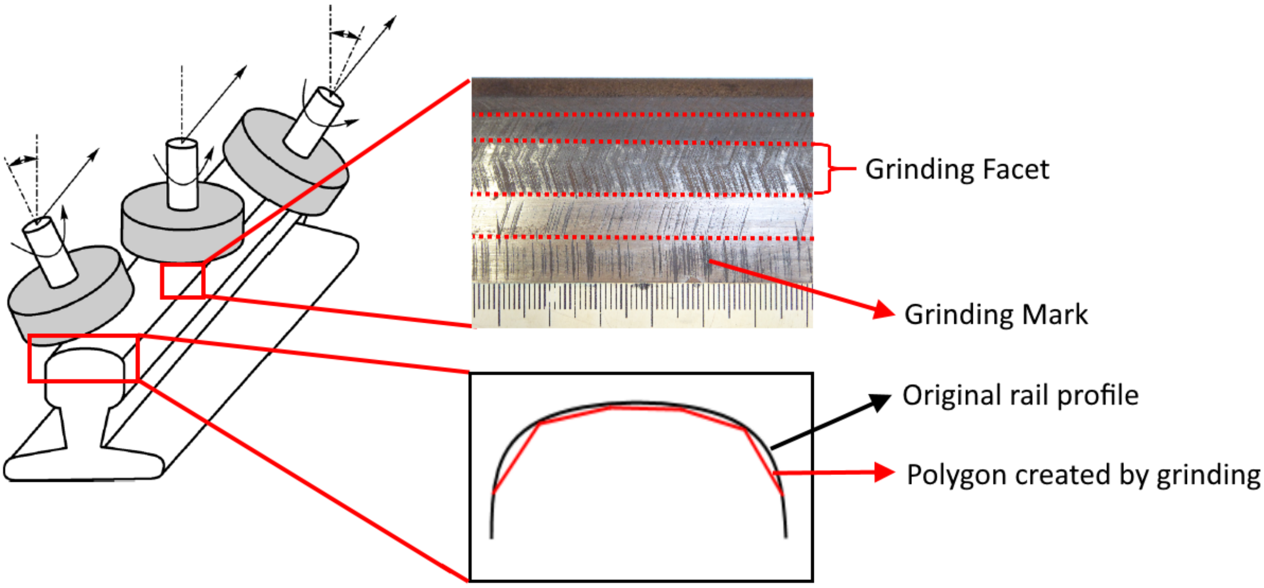

__Figure 2.7:__ A schematic drawing which shows the position an motion of the grinding stones relative to the rail surface.

In recent years, concerns have risen that grinding maintenance might induce RCF damage. Squat like defects are reported to reoccur at the same periodicity as the repeating grinding marks, suggesting that they were initiated by the conditions set during the grinding [63, 67]. Several sources also mention plastic deformation and WEL formation during the grinding [58, 63, 67]. This WEL can exist as isolated islands at the grinding marks, or as thick continuous patches [57, 58, 63]. Softer steel grades, such as R260, show that the WEL's are often spalled out of the rail by subsequent train wheel loading. Harder steel grades, such as MHH, show that the WEL's are pressed into the surrounding material, initiating cracks [58, 67].

Malkin and Guo quantified the power input and cutting depth during grinding with a number of formula's [41]. Koshal [30], Kalpakjian [26] and Kalousek et al [25]. further specified these formula's for rail grinding. In this study, these formula's will be used to calculate the temperature field during grinding, as shown in detail in appendix A1.2. The power input during grinding is can be calculated via [57, p. 27] (in W):

$$P \leq b * \left(\frac{\delta T_{max} * \lambda}{1.13 * \varepsilon * \sqrt{a}}\right)^{4/3} * \left(\frac{d_e}{C_{vw}}^{1/3}\right) * v_w^{0.433} \tag{2.1}$$

Where b is the facet width in m, δT_{max} is the maximum amount of temperature increase during grinding in °C. λ is the thermal conductivity of the metal in W/mK and ε is the energy partition coefficient [-]. a is the thermal diffusivity in m^2/s and d_e is the diameter of the grinding stone in m. C_{vw} is the specific energy in J/m^3. v_w is the speed of the grinding vehicle in m/s [57, p. 27].

The depth of the grinding marks is given as [57, p. 27] (in m):

$$a_e = \frac{P}{b * C_{vw} * v_w^{0.672}} \tag{2.2}$$

The same parameter can also be expressed as [57, p. 27]:

$$a_e \leq d_e * \left(\frac{4R_a^2 * v_s * Cr}{v_w}\right)^2 \tag{2.3}$$

Where R_a is defined as the surface roughness of the running surface after grinding in m. v_s is the tangential speed of the grinding stone in m/s. C is the number of contact points in m^{-2} and is defined as $45mm^{-2}$ for standard MESH 16 stones. r is the width-thickness ratio of the grinding chips and is given as 15 [-] [65, p. 59].

2.4 The relation between RCF, WEL and crack damages

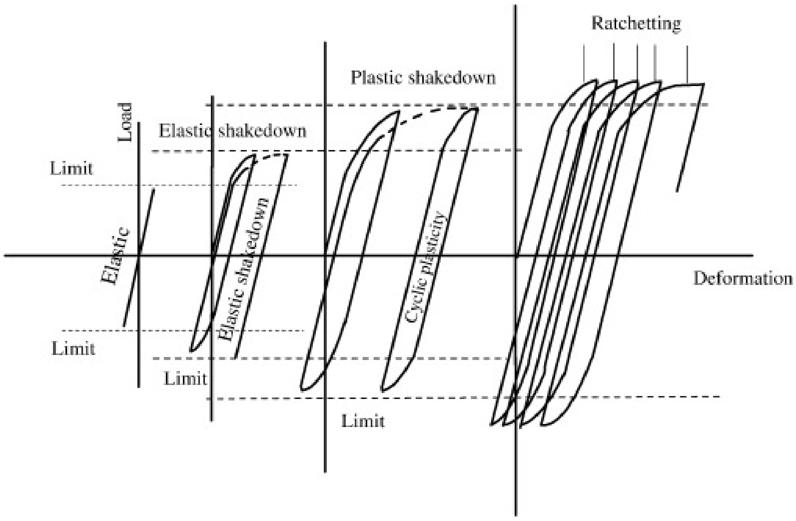

Figure 2.8: A schematic representation of elastic loading, elastic shakedown, plastic shakedown and ratcheting.

A rail can experience million of wheel-rail contacts in its life time. Ideally, these contacts only load the material in the elastic regime. In this regime, the material strains due to stretching of the atomic bonds. The atoms return to their original position after removal of the load. Elastic shakedown occurs when the material is loaded above its yield stress. This creates hardening of the material due to the movement of dislocations during plastic straining and the created residual stresses. These two effects raise the yield stress and ensure that the material stays in the elastic regime during subsequent load cycles. Plastic shakedown occurs when the subsequent load cycles also exceed the yield stress created by the elastic shakedown, known as the elastic limit. This causes the accumulation of plastic strain over the subsequent load cycles, creating a new plastic shakedown limit. Exceeding this limit will cause a phenomenon known as ratcheting. Ratcheting is the net change of strain due overloading and will result in the exhaustion of the plasticity of the material. This will eventually lead RCF crack initiation and possibly rail failure [83, p. 12]. Figure 2.8 schematically shows all these loading phenomena.

Cracks can additionally initiate at WEL, due to the brittle nature of these layers [4]. Cracks are mostly found to initiate at the rail surface in the WEL, in a vertical orientation [4, 31, 70]. These cracks might rotate in a horizontal direction when the stress field induced by wheel-rail contact changes at increasing distance from the wheel-rail contact point[84]. Horizontally growing cracks can occasionally cause spallations of the WEL [4]. In other cases, these cracks continue to grow at an angle of approximately 45° with the rail surface. A vertical fracture of the entire rail can occur when the crack exceeds its critical length [4]. The bonding between the base pearlite material and the WEL plays an import role in its potential to initiate cracks [67]. WEL could be removed from low hardness steel grades during wheel-rail contact, while remaining attached to high hardness steel grades [67]. In stratified layers of WEL and BEL, cracks initiate at the WEL-BEL interface and at the BEL-pearlite interface [70]. Formed cracks grow along the grain boundaries, the interfaces between the cementite lamellae and ferrite of the original pearlite and at the interfaces globular inclusions [70, 83]. Cracks can be stopped at an interface between stratified layers of WEL, BEL and the base pearlite [70, 83].

Zerbst et al. [84] describe that crack growth continues downwards with an angle of 10 to 40° with the rail surface. This is the direction in which the stress induced by wheel-rail contact is maximum [84]. The growth rate of cracks formed by ratcheting will initially reduce due to build up of a crack closure mechanism [84]. Crack growth will subsequently accelerate under the influence of mode I and mode II types of loading created by wheel-rail contact [84]. Subsequently, the crack growth rate will reduce again due to friction exerted by the crack flanks on each other [10, 63, p. 22]. Liquids present in the cracks can increase the crack growth rate by reducing this crack flank friction, which enhances mode II and III loading of the crack [84]. Additionally, the liquid can exert a pressure on the crack flanks, creating a additional mode I loading [84]. Finally, corrosion products are expected to form inside the crack in the presence of liquids [24]. These products may have a larger volume than the original metal and thus exert an additional Mode I loading on the crack [24]. The final stage of crack growth is initiated by crack branching under Mode II type loading [84]. Branching of a crack occurs if the crack growth rate is sufficiently high [84] and will dissipate the energy of at a crack over multiple crack branches [42]. Crack branches could grow upwards, causing spallation at the running surface of the rail. Another possibility is downwards crack growth under an angle of 60 to 80° with the running surface [84]. The crack mainly propagates under mode I type loading by bending and shear stresses induced by wheel-rail contact, superimposed by thermal and residual stresses [84]. Fracture of the entire rail occurs when the crack has grown beyond a critical length, exceeding the fracture toughness of the material [84].

2.4.1 Types of RCF damage in rails

A damage classically associated with RCF is a squat. Squats form on the running surface or gauge corner of the rail, as shown in figure 2.9a [69]. They exist out of a leading crack, growing due to severe plastic strain accumulation, and a trialling crack, growing in a brittle manner along the deformed texture. These cracks grows in the longitudinal and transverse direction of the rail, forming a typical V-shape. Beneath the surface, the cracks grow downwards at an angle of approximately 20°. Overlapping of the cracks occurs, causing the surface above the cracks to depress [69]. Squats grow further down into the rail web and cause a rail fracture [23, 68]. The role of WEL in squat formation is still uncertain, since some sources state that crack initiation could occur at the WEL [23, 69]. Others state that micro slip, tangential contact stresses and existing cracks play a far more significant role than the WEL [69].

A defect that is commonly confused with squats is a stud. Both of these defects have a similar shape during early growth stages. Studs also have a V-shape and grow from the gauge corner to the field side of the rail, as shown in figure 2.9b [16]. Beneath the rail surface, crack growth occurs in the transverse direction of the rail and in a downwards direction at an angle of 20° with the rail surface [16]. These crack turn in a horizontal direction at a depth of approximately 3 mm and cause spallation of the the rail surface, as shown in figure 2.9c [16]. These spallations cause an increase in dynamic loading on the rail during wheel passage. However, studs do not cause full rail fracture since they do not continue to grow in a downwards direction [16, 17]. Studs initiate at locations where thermal damage and WEL at the running surface are caused by the heat input during creepage of the wheel [16]. Creepage can occur due to poor adhesion between the wheel and rail [16]. Studs aren't related to the exhaustion of plasticity and thus cannot be classified as a typical RCF damage [16, 17].

Another kind of RCF defect found on the surface of rails are head checks. These damages received great attention after 4 people lost their lives and 70 people were injured during the Hatfield (UK) railway accident on the 17th of October, 2001 [9]. Head checks are parallel cracks that grow on the gauge corner of upper legs in rail curves, as shown in Figure 2.9d [55]. These cracks grow under an angle with the longitudinal direction of the rail and usually have a spacing in the order of centimetres. Head checks are caused by geometric spin and lateral contact forces between the wheel and rail gauge corner [55]. Cracks initiate under the surface and grow upwards. Anti-head check rail profiles have been developed to move the wheel rail contact towards the top of the rail, preventing stresses and crack initiation at the gauge corner [55]. WEL does not play a role in the formation of head checks. However, the profile of the rail discussed in this research is an anti-head check profile. Thus, the location of damages might have shifted towards the top of the rail due to the shift in wheel-rail contact location [58].

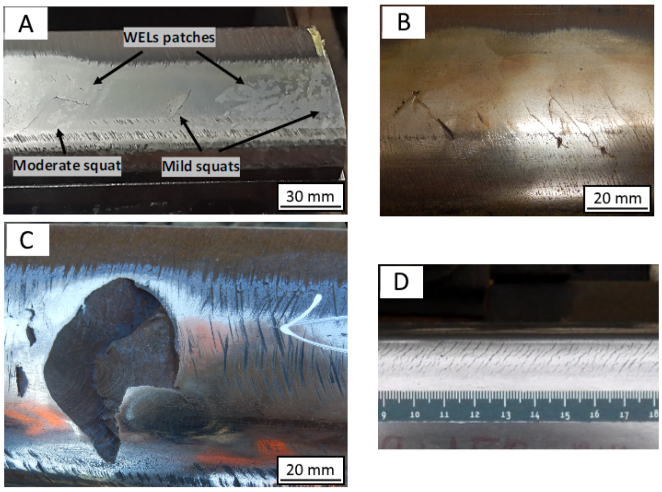

Figure 2.9: *(a): A squat found in the proximity of WEL. The squat has a typical V-shape and shows a depression in the rail surface in later stages of growth [23]. (b): Studs show a close resemblance to squats in the early stages of their formation. However, while squats tend to grow downwards and cause rail fracture, studs remain at the surface [16]. (c): A spallation caused by a stud. This type of damage will not lead to rail fracture, but can increase dynamic loading by passing wheels [16]. (d): Head checks often show a typical morphology with parallel cracks forming under a fixed angle at the gauge corner of the rail [55].*

Chapter 3: Materials and methods

3.1 Materials: History of the rail specimen

This research discusses a rail specimen installed on a 1.75% slope leading up to a fly-over near the Dutch town of Blauwkapel. The specimen was located in the upper leg of a right-handed curved track having a radius of 2257 m. Additionally, the rail was installed with a cant of 45 mm (1.8°), allowing for trains to pass at a speed of 140 km/h (39 m/s). A 54E 5 Anti-Head Check profile was used on this section of track. The steel grade of the rail is MHH, with a chemical composition as shown in table 3.1 [63, p. 29].

Table 3.1: *The range of compositions specified for MHH [12, p. 21] and the composition of the specimen discussed in this research [63] in wt.%.*

		C	Si	Mn	P	S	Cr	Al	V	N	H_2 [ppm]
EN-EN 13674-1:2011	**Min**	0.72	0.40	0.80			0.40				
	Max	0.82	0.80	1.10	0.020	0.020	0.60	0.004	0.030	0.009	1.5
Specimen Blauwkapel		0.78	0.65	0.93	0.012	0.009	0.53	0.001	0.003	0.003	1.7

The rail was manufactured in 2011 and installation at Blauwkapel took place in 2012 [63, p. 31]. Table 3.2 shows the measured traffic at the fly-over for 2016 [63, p. 32]. It is estimated that traffic will increase with 1 or 2% every year [27, p. 40].

Table 3.2: *The recorded traffic in 2016, at the location of the rail specimen [63, p. 32].*

	Total Trains	Total tons	Total Axles
Passenger trains	**25,945**	**10,873,288**	**761,761**
Ascending	26,711	11,294,514	794,856
Descending	197	58,689	4,306
Freight trains	**692**	**383,993**	**29,274**
Ascending	666	377,230	28,777
Descending	26	6,763	497
Others	**271**	**95,922**	**8,127**
Ascending	271	95,922	8,127
Descending	0	0	0
Total:	**26,908**	**11,353,203**	**799,162**

Cyclic grinding maintenance was specified to be performed every 15 Mega Gross Tons (MGT), corresponding to once every 16 months [63, p. 32]. Postponement or cancellation of the grinding maintenance may occur, adding a maximum of 10 to 15 MGT to the specified maintenance interval [63, p. 32]. Table 3.3 indicates the performed grinding maintenance [63, p. 33]. In 2014 and 2015, no grinding maintenance was executed due to unforeseen circumstances, thus exceeding the limit of 30 MGT [63, p. 33].

Table 3.3: *An overview of the cyclic grinding maintenance performed on the rail specimen [63, p. 33]. The contract of 2011 specifies that 0.20 mm of material is removed with a 48 stones grinding machine, moving at a vehicle speed of 8-10 km/h [63, p. 33]. The contract of 2015 states that 0.17 mm of material is removed with a 64 stones grinding machine, at a vehicle speed of 12-15 km/h [63, p. 33].*

Year	Number of maintenances	According to contract
2012	2	2011
2013	1	2011
2014	0	-
2015	0	-
2016	1	2015
2017	1	2015

Automated ultrasonic and eddy current NDT inspections are executed every six months [63, p. 30]. Surface defects were first detected during an inspection in April 2016. One year later, the size of these defects had exceeded safety thresholds and a manual ultrasonic inspection was performed on the 21^{st} of April 2017. The rail was subsequently removed on the 19^{th} of June 2017 [63, p. 30]. The rail had experienced 3 MGT [63, p. 50] of train loading since the last grinding maintenance and 61 MGT of train loading during its five years of operation [63, p. 31]. This is significantly lower than the specified life time for curved sections of track, which lies between 400 and 800 MGT [63, p. 31].

3.2 Macro characterization methods

A visual inspection of the rail surface was done to identify damages and other characteristics left by cyclic grinding and wheel-rail contacts. Micro roughness measurements of the rail surface were done with a Mitutoyo Sj-210 surface roughness measurement tool [71], according to ISO 1997. A Gauss filter with cut off ratios λ_s and λ_c of 8 and 2.5 respectively was used. The N value (number of samples per measurement) was selected to be 4 and the measurement speed was chosen to be 0.75 m/s. Subsequently Leeb rebound hardness measurements were done with an Equotip [13] to estimate if any surface hardening had taken place during service of the rail. Finally, the profile of the rail was measured and compared to a reference profile, using a Miniprof profile measurement device and related software [44]. Figure 3.1 shows each of these characterization methods.

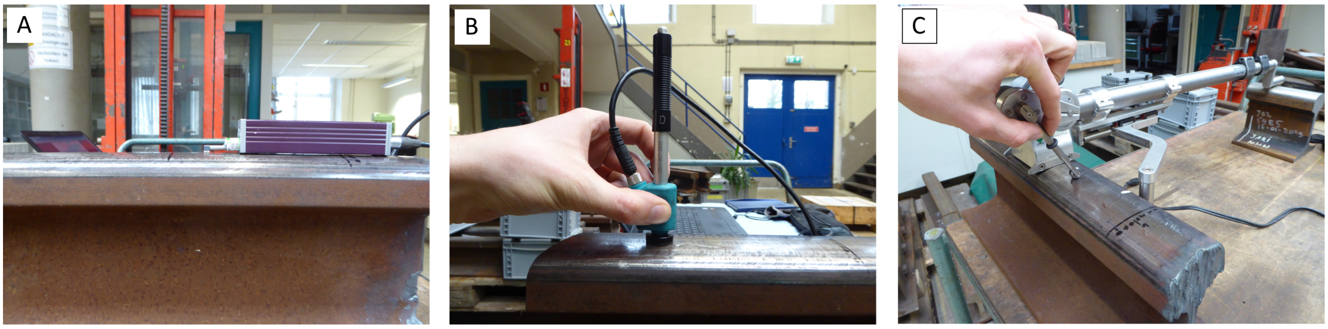

Figure 3.1: *(a): A surface roughness measurement tool on the running surface of the rail. (b): The Leeb rebounce hardness test being applied to the rail surface. (c): Measuring the rail profile with a Miniprof tool.*

3.3 Metallographic examination methods

Figure 3.2a shows the running surface of the rail specimen. The section of the running surface which underwent only grinding and the section which underwent grinding and additional wheel-rail contacts are marked in blue. Additionally, the location of the cross-sections made for metallographic examination are shown in red. The arrow indicates the direction of examination. Wire-EDM cutting [81] was used to extract these specimens, thus preventing thermal or mechanical damage to the material. These specimens were subsequently embedded in Streuers PolyFast hot mounting resin. A maximum curing temperature of 180°C and heating time of 8 min were used to prevent thermally damaging of the specimens. Mild grinding with 80, 180, 320, 800, 1200 and 2000 grid paper followed. Finally, the specimens were polished with 3 and 1 μm diamond polish and etched with 2% Nital.

A Keyence VHX 5000-900F digital microscope was used to optically examine the morphology of the base pearlite, WEL, BEL, plastic deformation of the pearlite and cracks. Additionally, the thickness of WEL, BEL and deformed pearlite was measured using the Keyence software. Vickers micro hardness measurements were done on a Struers DuraScan G5 tester. A 025 N load and 10 seconds indentation time were used for micro hardness indenting. These micro hardness indents were subsequently measured using the Keyence VHX 5000-900F digital microscope. A JEOL JSM 6500F Scanning Electron Microscope (SEM) was used to characterize the microstructures of the WEL, BEL and underlying pearlite with Secondary Electron (SE) Imaging. Cracks, inclusions and corrosion were characterized with SE imaging and Energy Dispersive X-ray Spectroscopy (EDS).

The specimen labelled as "MHH base" in figure 3.2b was used to characterize the MHH base material using optical microscopy, Vickers micro hardness, SE imaging and EDS. The inter lamellar spacing of the cementite was measured with the method described in [78]. This specimen underwent the same preparation method as described previously. However, grinding wheel cutting was used to extract the specimen.

Specimens characterized with X-ray Diffraction (XRD) are schematically shown in green in figure 3.2. All of these specimen were extracted by grinding wheel cutting. The specimen labelled ”XRD 1” in figure 3.2 is used to characterize the as manufactured MHH base material. The XRD 2 specimen partially covers the section of the running surface which only underwent grinding and partially covers the section of the running surface that underwent additional wheel-rail contacts. The XRD 3 specimen underwent both grinding and wheel-rail contacts and contains a large patch of WEL. The XRD 1 specimen was ground and polished until 1 μm to remove the effects of corrosion. Specimens ”XRD 2” and ”XRD 3” were only mildly ground with 2000 grid paper to remove surface corrosion.

XRD was used to analyse phase present in a patch of WEL at the surface of specimen XRD 3. A Bruker D8 Advance diffractometer with Bragg-Brentano geometry, graphite monochromator and Vantec position sensitive detector were used during this analysis. Co Kα radiation was created at 45 kV and 35 mA. The 2θ step size was set at 0.035° and measurements were done every 4 seconds. Additionally, the longitudinal residual stress state at three rail surfaces was measured using the $sin^2(\psi)$ method [45]. Specimen XRD 1 was used to measure residual stresses after manufacturing of the MHH base material. Specimen XRD 2 was used to measure the stress state after grinding and after additional wheel-rail contacts. A Bruker D8 Discover with an Eulerian cradle and parallel beam geometry was used for these measurements. Co Kα radiation was created at 45 kV and 25 mA. An area with sides of 2mm was exposed to this radiation.

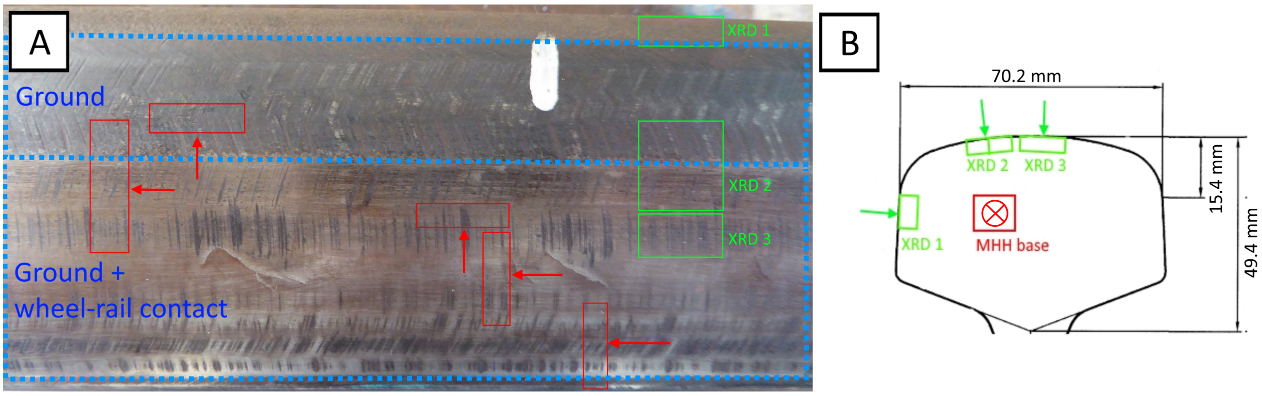

Figure 3.2: *(a): The location of the extracted microscopy specimens is shown in red. The examined surfaces are indicated by the arrows. The XRD specimens are indicated in green. The blue lines indicate the sections of the running surface which underwent only grinding or grinding and additional wheel-rail contacts. (b): The specimen used for the microscopical characterization of MHH is indicated in red. The green specimens are used for characterization with XRD. The arrows indicate the direction of observation.*

3.4 Computer simulations

Several computer simulations were done to support results gathered during the experimental work. Firstly, Thermo-Calc ©simulations were done to construct the property diagram of MHH and calculate the martensite transformation temperatures. The results of this simulation are shown in section 4.1. Secondly, Vampire ©[38] wheel-rail contact simulations were done to characterize the wheel-rail contact points, transferred forces and creepage. Thirdly, an analytical model was created in Matlab ©to calculate the temperature field during grinding as a function of time and depth below the rail surface. Fourthly, Finite Element Analysis (FEA) modelling was done in Comsol Mulitphysics 5.4a ©to characterize the stress and strain in stratified layers of WEL, BEL and the base pearlite. Detailed descriptions of the Vampire ©, Matlab ©and Comsol ©models are given in appendix A1.

Chapter 4: Results

4.1 Thermo-Calc simulation of the MHH base material

Thermodynamic simulation of the MHH base material were done using Thermco-Calc 2019a ©software and the TCFE9 database. The chemical composition of the rail specimen, as given in table 3.1, was simplified to: 0.78 wt.% C, 0.65 wt.% Si, 0.93 wt.% Mn, 0.53 wt.% Cr and 97.11 wt.% Fe. The resulting property diagram is shown in figure 4.1. It is expected that 11.6% of the pearlite is comprised of cementite as per thermodynamic equilibrium calculation. The A_1 and A_3 temperatures at atmospheric pressure and slow heating rates were determined to be 725 $^{\circ}C$ and 798 $^{\circ}C$ respectively.

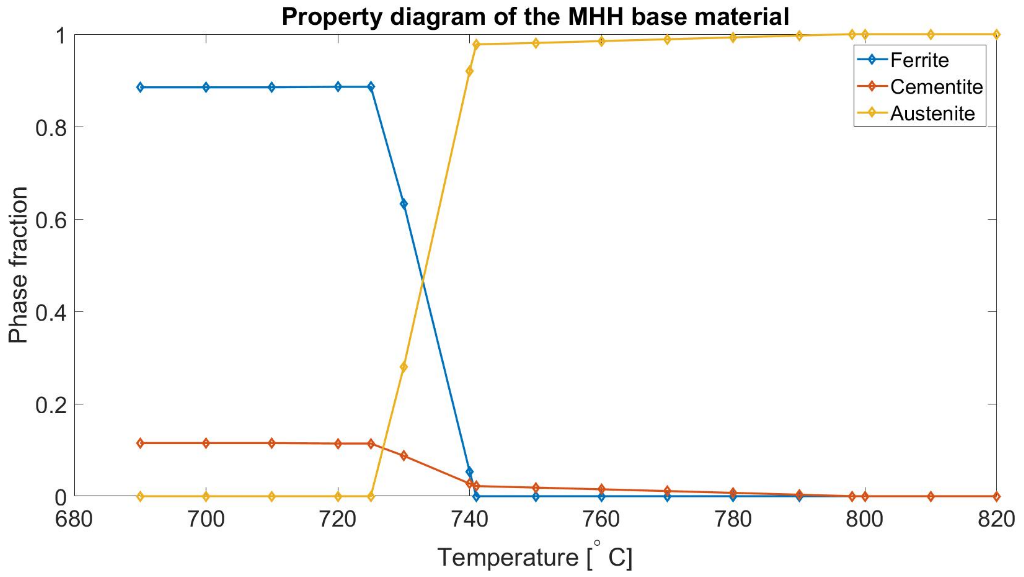

Figure 4.1: *The property diagram of MHH at atmospheric pressure, constructed using Thermo-Calc ©.*

The martensite temperatures were calculated using Thermo-Calc 2019a ©with TCFE9 and MOBFE4 databases. The average prior austenite grain size was estimated to be 20 μm. The resulting Ms-temperatures as a function of austenite carbon content are shown in figure 4.2. The carbon content of the retained austenite in the studied WEL was determined to be 0.90 ± 0.10 wt.%, as shown in section 4.7 and appendix B2. Figure 4.2 shows that approximately 90 % of the retained austenite transforms to martensite at this carbon content. It has to be noted that the hydrostatic stresses created due to the volume difference between austenite and martensite have not been considered in this calculation [7]. The true Ms-temperatures could thus be much lower than shown in the figure.

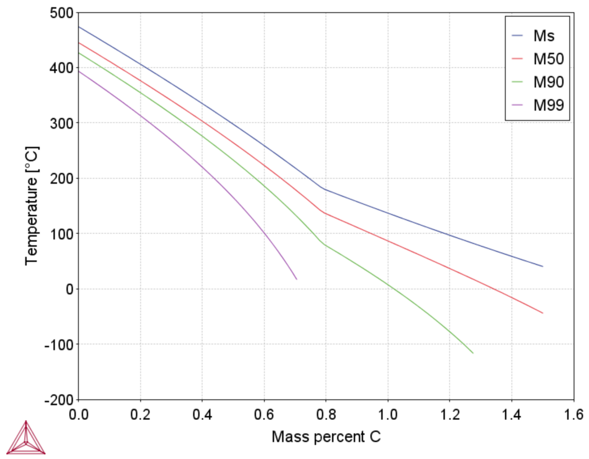

Figure 4.2: *The martensite temperatures for MHH at atmospheric pressure, as a function of austenite carbon content. The austenite carbon content was determined to be* 0.90 ± 0.10 *wt.% (appendix B2).*

4.2 Macro examination of the rail surface

A Vampire ©simulation defines the contact points between a wheel and measured rail profile, as shown in figure 4.3a. The contact points given by the simulation correspond to the wear pattern on the surface rail shown in figure 4.3b. Thus, several wheel-rail contact bands can be defined using the Vampire ©simulation. In the curve, wheel contact will mainly occur at the primary contact band (PCB). Contact will shift from the PCB to the secondary contact band (SCB) when a train travels over the section of track at a lower speed than the majority of the trains [63, p. 30] or due to a possible lateral oscillating motion of the train [80]. Vampire ©shows that the contact patch will have a larger area at the SCB, thus lower stresses at the surface are expected. Between the PCB and SCB, the tertiary contact band (TCB) shows a region where only a small amount of wheel contact takes place, dominantly at the edges of the grinding facet. Due to the anti-head checking profile of the rail, no contact occurs at the gauge corner (GC). Vampire ©also shows that the leading wheels on the bogies will make flange contact below the GC, at the flange contact band (FCB). No wheel-rail contact takes place at the ground band (GB), thus leaving the original grinding marks intact in this section of the running surface. Finally, it is seen that the weight of the train moves to the rear wheels during ascending. This leads to a maximum total creepage of 0.628%. Here, the total creepage is defined as the projection of the longitudinal and lateral creepage. When relating this value to the work of Naeimi et al. [47], it can be estimated that a temperature increase of $200°C$ occurs during wheel-rail contact.

Figure 4.3b shows the running surface of the rail after etching with 2% Nital. Patches of WEL can be identified by their white colour and are marked in red in the figure. The WEL exists in between the grinding marks on the GB and in long streaks and patches on the SCB and TCB. WEL on the PCB or GC could not be clearly identified. Cracks are mainly found at the PCB and might initiate at the grinding marks on the adjacent facets [63, p. 50]. These crack show a morphology similar to a squat or head check and repeat approximately every six cm, with the same periodicity as the grinding marks. Figure 4.3b additionally introduces an axis system which will be used throughout this report.

Micro roughness measurements show that grinding induces a high surface roughness ($R_a = 5.42 \pm 1.20\mu$m), which is worn off during repeating wheel-rail contacts. Wear was most dominant at the PCB ($R_a = 1.06 \pm 0.74\mu$m). Less wheel-rail contacts occurred at the SCB and TCB, thus still leaving some of the original grinding marks. At the gauge corner, contact only took place at the facet edges, causing them to quickly wear away. Flange contact only caused limited wear on the side of the rail head. A small amount of work hardening during wheel loading caused the surface hardness after grinding to increase from 362 ± 13 HV to 409 ± 40 HV. However, these values do no exceed the specified maximum of 427 HV [12, p. 21]. Rail profile measurements (see appendix A1.1) show that material removal by grinding and wear was most dominant at the GC and PCB.

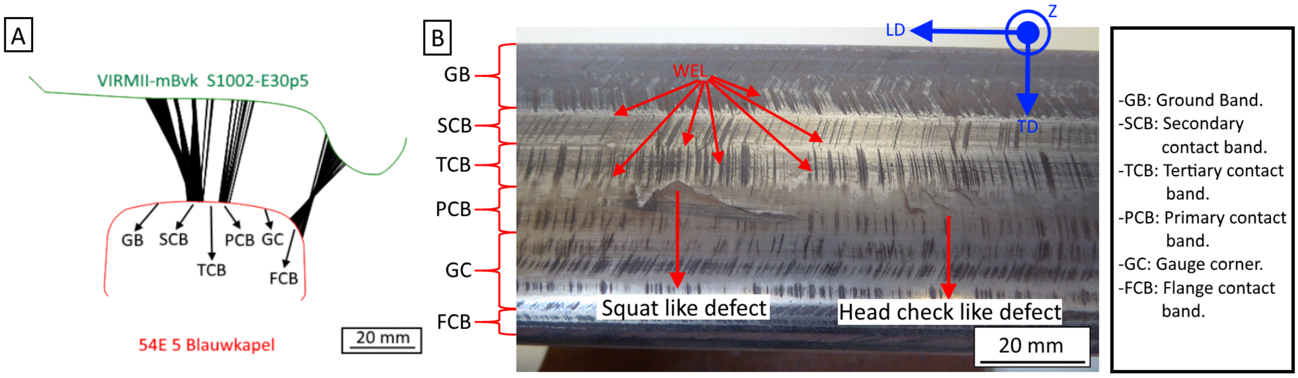

Figure 4.3: *(a): The vampire ©simulation shows the possible contact points between the wheel and rail profile as a function of lateral displacement of the wheel. The defined bands on the running surface are indicated by the arrows. The abbreviation are given in the box on the far right side of the figure. (b): A macro view of the etched running surface of the rail. The blue arrows define the set of axis used in this report. The axis are defined in the longitudinal direction (LD) of the rail, in the transverse direction (TD) towards the gauge site. The z-direction points vertically upwards from the running surface of the rail. Finally, the defined contact bands are indicated. Grinding marks are recognized as dark, transverse cuts. WEL is marked in red and can be seen in the form of white discolouration on the rail surface. Two types of cracks are identified on the rail surface: one with a squat like morphology and one with a head check like morphology.*

4.3 Optical Microscopy

The fully pearlitic microstructure of the MHH base material is shown in figure 4.4. The presence of pro-eutectoid cementite cannot be determined at this magnification. Long, slender, MnS inclusions exist in the material [83, p. 111], orientated in the longitudinal direction of the rail. These inclusions are formed during the steel making process and are elongated in the longitudinal direction of the rail during hot rolling.

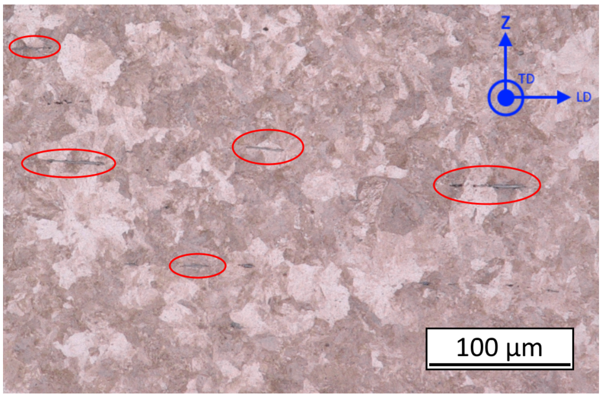

Figure 4.4: *The microstructure of MHH is fully pearlitic. Black, slender inclusions are orientation in the longitudinal direction of the rail. These inclusions have been encircled in red in this figure.*

Two types of WEL, BEL and/or plastically deformed pearlite are found in the GB. The first of these types is shown in Figure 4.5a. A thin layer of WEL with a layer of plastically deformed pearlite underneath is seen. The WEL has a highly irregular shape, probably due to the high surface roughness created by grinding and pitting corrosion during the service life of the rail. Figure 4.5b shows the plastic deformation underneath the WEL in greater detail. Only localized regions of plastic deformation were found in the GB. Figure 4.5c shows the second layer type, existing out of stratified layers of WEL and BEL. The thickness of the WEL and the BEL varies greatly. Additionally, corrosion at the surface is seen in both homogenous and pitting form.

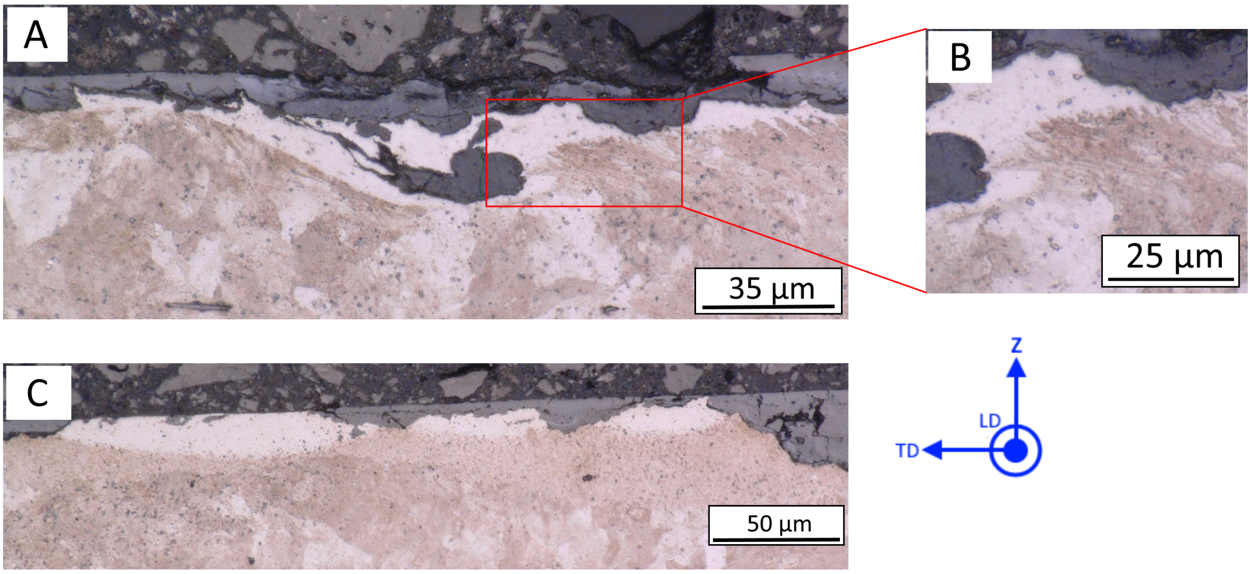

Figure 4.5: *(a): A thin layer of WEL in the ground band. The layer shows a irregular morphology and deformed pearlite underneath. (b): Stratified layers of WEL and BEL in the ground band. Great variation exists in the thickness of the layers.*

WEL and BEL were also found in the SCB and showed distinctly different morphologies than in the GB. Figure 4.6a shows that stratified layers of WEL and BEL in the SCB have a more constant thickness than in the GB. Figure 4.6b shows a region where WEL is mixed with brown splinters, as marked in red in the figure. The fraction of these splinters increases with increasing depth. Above this region of WEL with brown splinters, a layer of WEL with its regular white colour reaches until the rail surface. Secondary Electron (SE) imaging will be required to gain more detail on the microstructure of these splinters. Finally, figure 4.6c shows a layer of WEL with undeformed pearlite underneath in the SCB. A crack is seen to grow along the interface of the WEL and base pearlite. localized corrosion of the WEL at one of the crack flanks is observed. EDS techniques will be required to confirm the presence of oxides at this section of the crack flank. All of the layers in the SCB showed sharp transitions between the WEL, BEL and base pearlite. No deformed pearlite was found to exist under any of these layers. Material removal in the SCB via corrosion occurred in a smaller extent than in the GB. This, together with wear of the surface in the presence of wheel-rail contact, results in a WEL with a smooth top surface. Figure 4.6d shows that long patches of WEL with underformed pearlite underneath are dominant in the TCB. Pitting corrosion of the WEL is again seen. A crack grows into the base material under a 45°angle with the rail surface, at a corrosion site of the WEL and base pearlite. The crack continues its growth in a horizontal direction at a depth of 70 μm, suggesting that the stress field induced by wheel-rail contact changes at this depth [84]. Further crack growth might cause spallation of the material above [16].

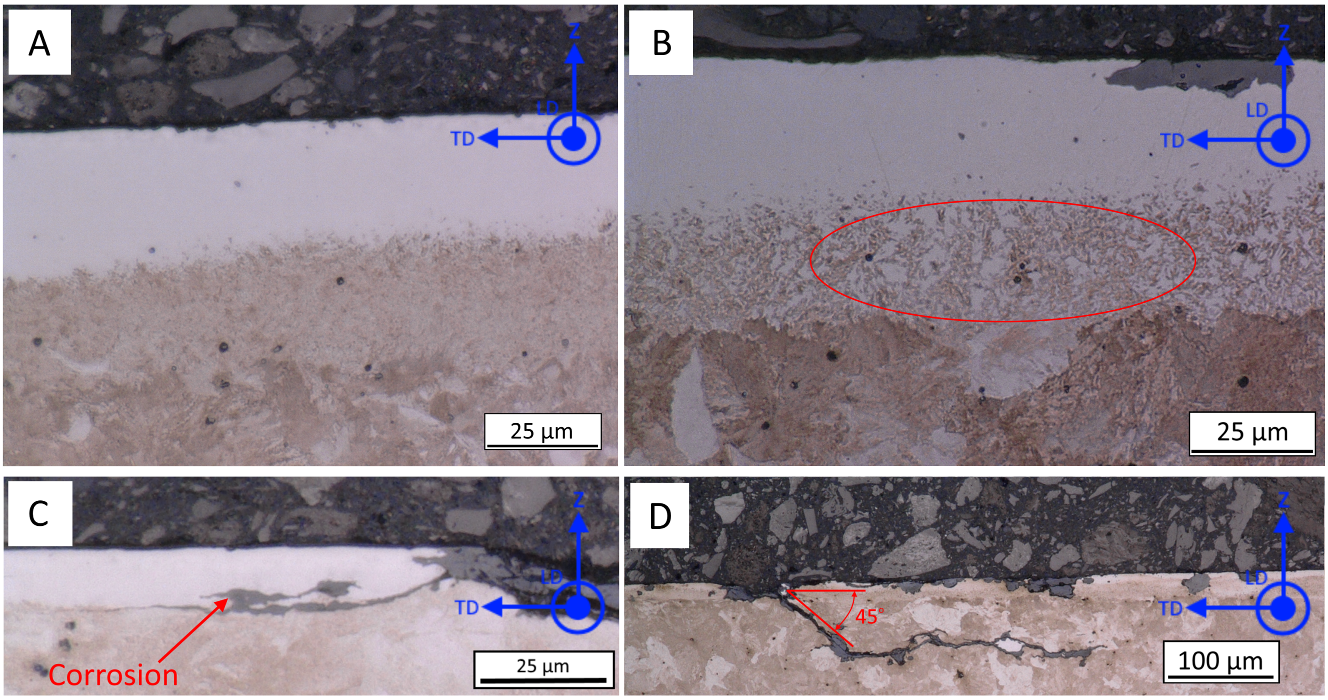

Figure 4.6: (a): A stratified layer of WEL and BEL in the SCB. Wheel-rail contacts have removed surface roughness, corrosion and irregularities. (b): A stratified layer of WEL with a region of WEL and brown splinters underneath (marked in red) in the SCB. (c): A crack growing at the interface of the WEL and the base pearlite in the SCB. (d): A thin layer of WEL with undeformed base pearlite underneath in the TCB. A crack is seen to initiate at the WEL under a 45° angle with the rail surface. The crack changes its direction of growth due to a changing stress [84] field when reaching a depth of 70 μm.

Figure 4.7a shows a transverse cross-section of the PCB, containing two cracks. These cracks start growing at the rail surface at an angle of 20° and 37° respectively. A visual inspection of the rail surface indicates that the small crack in figure 4.7a has a width of approximately 3 mm, while the larger crack has a width of approximately 6 mm. Uniform corrosion has occurred at the crack flanks close to surface of the rails. At a depth of 0.5 to 1 mm, both cracks turn in a horizontal direction and start branching since the stress field induced by wheel-rail contact changes with increasing distance from the wheel-rail contact point [84]. Future wheel-rail contacts can induce further growth of these branches. However, at this stage it cannot be determined if crack branch growth will continue in a horizontal or upwards direction, possibly leading to spallation of the material at the running surface [63, p. 52]. Fracture of the rail can occur if branches increase their angle with the rail surface during further growth. Another possibility is the arrest crack growth since the energy for crack growth is dissipated over each of the crack branches [10].

Red letters in figure4.7a mark the locations of the magnifications shown in figure 4.7b through e. Figure 4.7b shows the first growth stages of a crack at the rail surface. The crack follows the curvature of the surrounding deformed pearlite, suggesting it was initiated by ratcheting. Crack growth at the rail surface starts at a 15° with the rail surface due to the curvature of the deformed pearlite. This angle later increases to 55° and further crack growth is expected to occur under the angle of the maximum resolved shear stress induced by wheel-rail contacts [84]. A slightly white discolouration was found at the running surface, near to the initiation site of the crack. SEM analysis will determine if any microstructural changes of the base pearlite have taken place here. No patches or layers of WEL are found at the surface of the PCB, suggesting that the WEL induced by grinding has spalled or wore off during subsequent wheel-rail contacts.

Figure 4.7c shows that more developed cracks also follow the curvature of the deformed pearlite at the running surface of the rail, suggesting growth via ratcheting. The initiation mechanism of these cracks cannot be determined. These cracks are sufficiently large to only be partially removed by the last cyclic grinding maintenance and thus could have existed prior to this maintenance. Additionally, the role of WEL in the initiation of these cracks cannot be determined due to the removal of this layer by wheel-rail contacts. Both uniform and localized corrosion is seen at the crack flanks. Figure 4.7d shows corrosion in the form of silver oxide particles inside the crack. Additionally, localized corrosion can be seen along the flanks of the crack and the crack branches. Water trapped inside a crack enhance the corrosion at the crack flanks [24]. The presence of oxides thus suggests that water was present in the crack at some stage during the service life of the rail. EDS analysis will be required to confirm the presence of oxides. Furthermore, additional cracks surrounding the main crack at its point of branching, suggesting that a network of cracks is developing due to the changing stress field [84]. Figure 4.7e shows WEL at the boundary of the PCB and TCB. This indicates that removal of WEL only occurred at the most severely wheel loaded sections of the running surface. Plastic deformation of the pearlite is less extensive in the TCB than at the PCB since this band was less severely loaded. Pitting corrosion of the WEL and cracking at the interface of the WEL and the base pearlite are again seen at the TCB.

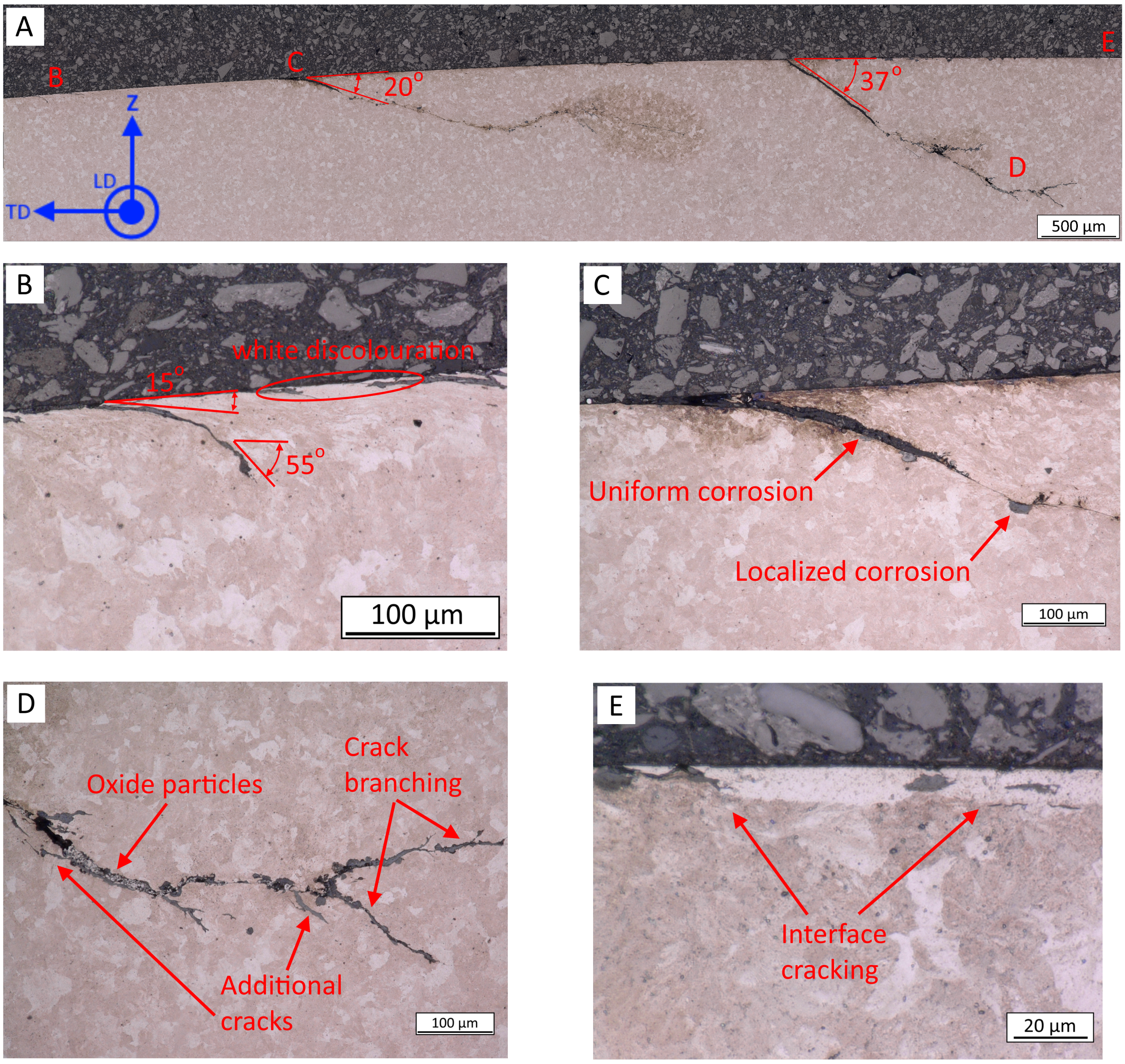

Figure 4.7: *(a): Two cracks at the PCB. The red letters indicate the location of the figures b through e. (b): Crack initiation following the curvature of the deformed pearlite. White discolouration is at the rail surface near the crack. (c): The crack opening of a more developed crack at the PCB. This crack also follows the curvature of the surrounding deformed pearlite and shows both uniform and localized corrosion. (d): crack branching and corrosion of the crack flanks. Additional cracks surround the main crack and its branches. (e): A layer of WEL at the transition from the PCB to the TCB. Cracking at the interface of the WEL and base pearlite and (subsurface) pitting corrosion are seen.*

Figure 4.8 shows that WEL at the GC is very similar to that found in the GB; a thin layer of WEL with plastically deformed pearlite underneath is found here. This plastic deformation is created during grinding, since Vampire ©showed that wheel-rail contact at the gauge corner only rarely occurred. The WEL itself is spalled in half and traps liquids used during sample preparation.

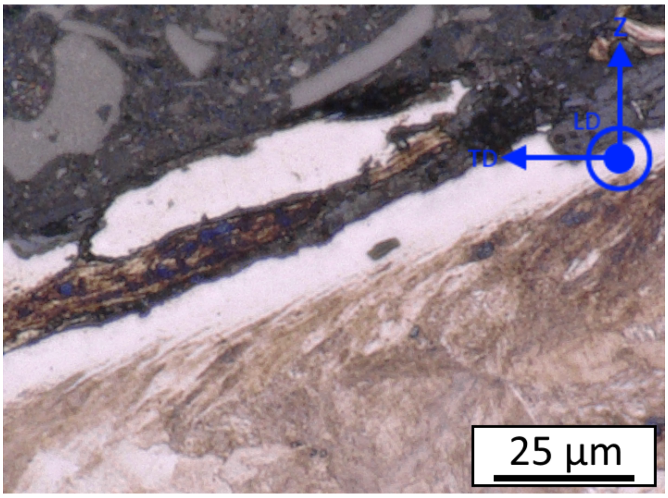

Figure 4.8: *A fractured WEL with deformed pearlite underneath at the gauge corner of the rail.*

4.3.1 Thickness of the WEL, BEL and deformed pearlite

The thickness of all the observed layers was measured and collected in table 4.1. The high scatter in the measurements of the GB was caused by the high surface roughness induced by grinding, surface corrosion and spallation at the rail surface. Wear due to wheel-rail contact reduced the surface roughness of the WEL and thus the spread in this measurement.

Starting at the GB, the thickness of WEL with plastically deformed pearlite or BEL underneath was similar. The BEL in the GB had a larger average thickness than the WEL and showed a large spread, possibly due to unsteady heating conditions during grinding. In the SCB, the thickness of the WEL had increased compared to the GB, while the thickness of the BEL stayed constant. The WEL at the TCB was slightly thinner than that at the SCB. The presence of plastic deformed pearlite in the SCB or TCB could not be determined with optical microscopy. The WEL and BEL had a sufficiently large thickness in these contact bands to cover the region under the rail surface were plastic deformation was found in the GB and at the GC. Thus, plastic deformation in the SCB en TCB was possibly hidden by the WEL and BEL.

The layer of plastically deformed pearlite at the PCB had a much larger thickness than that at the GB, suggesting it was created by wheel-rail contacts after grinding. Finally, the thickness of the WEL and plastic deformed pearlite at the GC was similar to that found in the GB. Plastic deformation at the GB can only have originated from the grinding, since no wheel-rail contact took place here. The similar thicknes sof the plastic deformation at the GC suggests that they both originated from the grinding process.

Table 4.1: *The measured thickness and variance of each the WEL, BEL and plastically deformed pearlite.*

Thickness of the layers [μm]				
Location of the layer	**WEL**	**BEL**	**Mixture of WEL islands**	**Deformed pearlite**
Ground band	12.3 ± 6.1	22.5±12.0	–	9.0 ± 3.2
Secondary contact band	36.5 ± 4.8	20.0 ± 3.6	25.3 ± 6.7	–
Tertiary contact band	23.8 ± 9.6	–	–	–
Primary contact band	–	–	–	31.1 ± 7.9
Gauge corner	11.4 ± 5.9	–	–	11.0 ± 0.3

4.4 Vickers micro hardness

Vickers micro hardness measurements were done at varying depths in the GB and SCB. Figure 4.9 shows a set of one of these measurements. Figure 4.10 shows a graph of the hardness measurements as a function of depth beneath the surface. The left-hand graph shows the data gathered from the GB. WEL and BEL had a hardness of 1000 HV and approximately 800 HV respectively. These values were found to be independent of the depth below the surface. The hardness values of the base pearlite were scattered between 400 HV and 500 HV and did not show a clear dependence on the depth below the surface. When comparing this to a reference hardness measurement of 402 HV for the MHH steel grade, it can be concluded that only a slight amount of work hardening has taken place. The scatter can be caused by the orientation of the pearlite colony at the location of the measurement. These colonies are made up of ductile ferrite and brittle cementite lamellae. These lamellae will react differently to the force of the indentation, depending on their orientation with respect to the vector of the force.

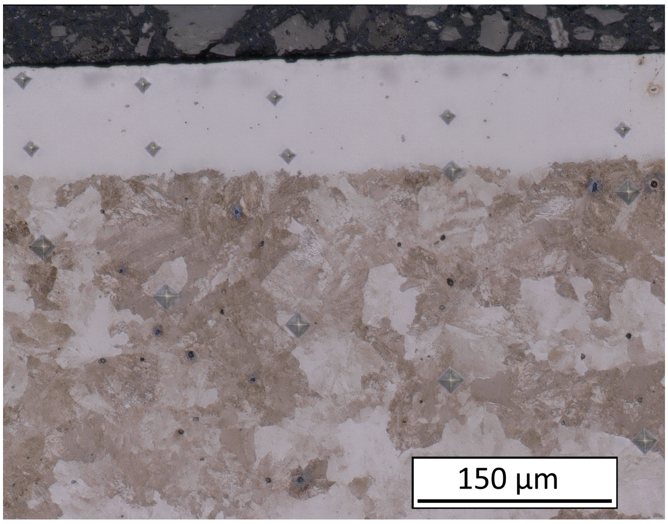

Figure 4.9: *The Vickers micro hardness measurements can be recognized by the diamond shaped indentations at varying depth in the WEL and base pearlite.*

The right hand graph in figure 4.10 shows the hardness measurements from the SCB. The hardness of the WEL increased from 850 HV at the rail surface, to 1000 HV at a depth of 25 μm. This suggests that the WEL at the rail surface has been tempered during wheel-rail contacts. The hardness of the BEL varied between 630 HV and 700 HV, possibly due to the varying fraction of martensite, retained austenite and desolving or deformed pearlite in the BEL [31, 70, 83]. Further SEM analysis will be required to conclude on this. The hardness of the mixture of WEL and brown splinters depends on the fraction of these two constituent. As the fraction of WEL decreases at greater depth, the hardness of the layer decreases. Finally, The base pearlite again shows a slight work hardening independent of the depth below the surface and scatter in the data due to the orientation of the individual colonies.

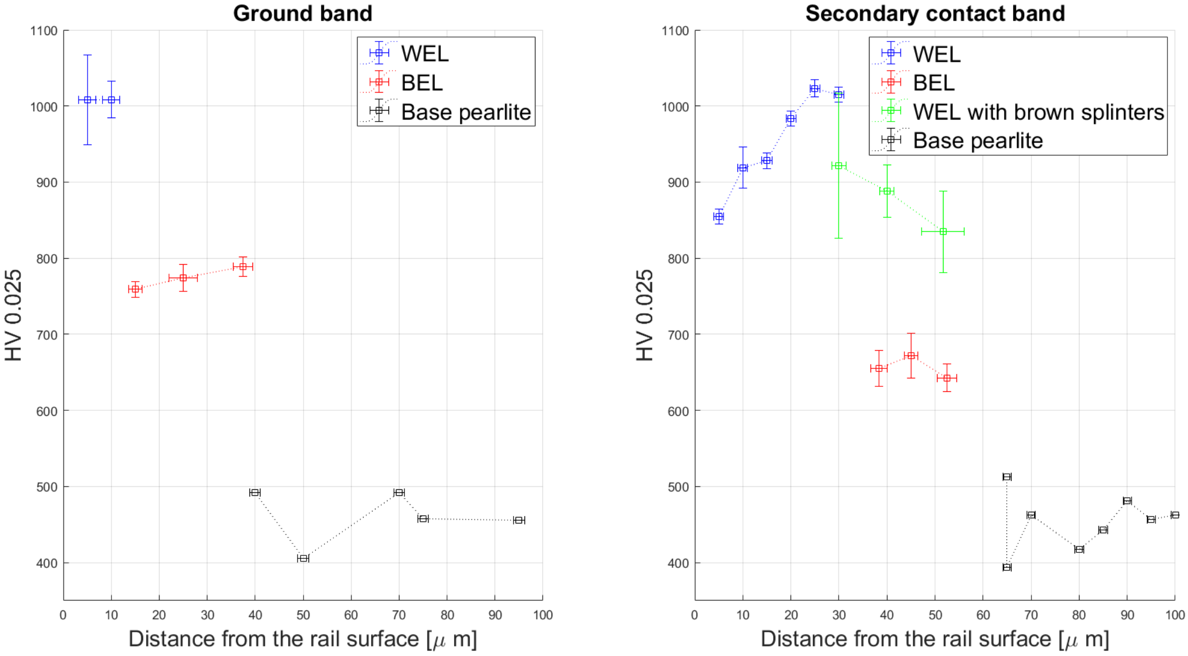

Figure 4.10: *The graph on the left shows the Vickers micro hardness of WEL, BEL and base pearlite in the ground band. The graph on the right shows the measurements done in the secondary contact band.*

4.5 Scanning Electron Microscopy

4.5.1 The MHH base pearlite

Figure 4.11 shows the pearlitic microstructure of the MHH base material. A total of 40 measurements shows that the average inter lamellar spacing is 99 ± 54 nm [78]. The large spread of this value is caused by the many different orientations of the lamellae with respect to the micrograph. The projections of lamellae of cementite orientated perpendicular to the micrograph have an appearance similar to a circle and can be seen in the red circle in the figure. Pro-eutectoid cementite was occasionally observed at the grain boundaries of the prior austenite grains. These prior austenite grain boundaries are marked by the red dotted line in the cut-in of figure 4.11. EDS analysis confirms that the slender, black inclusions have a MnS composition, as shown in the EDS spectrum in figure 4.11.

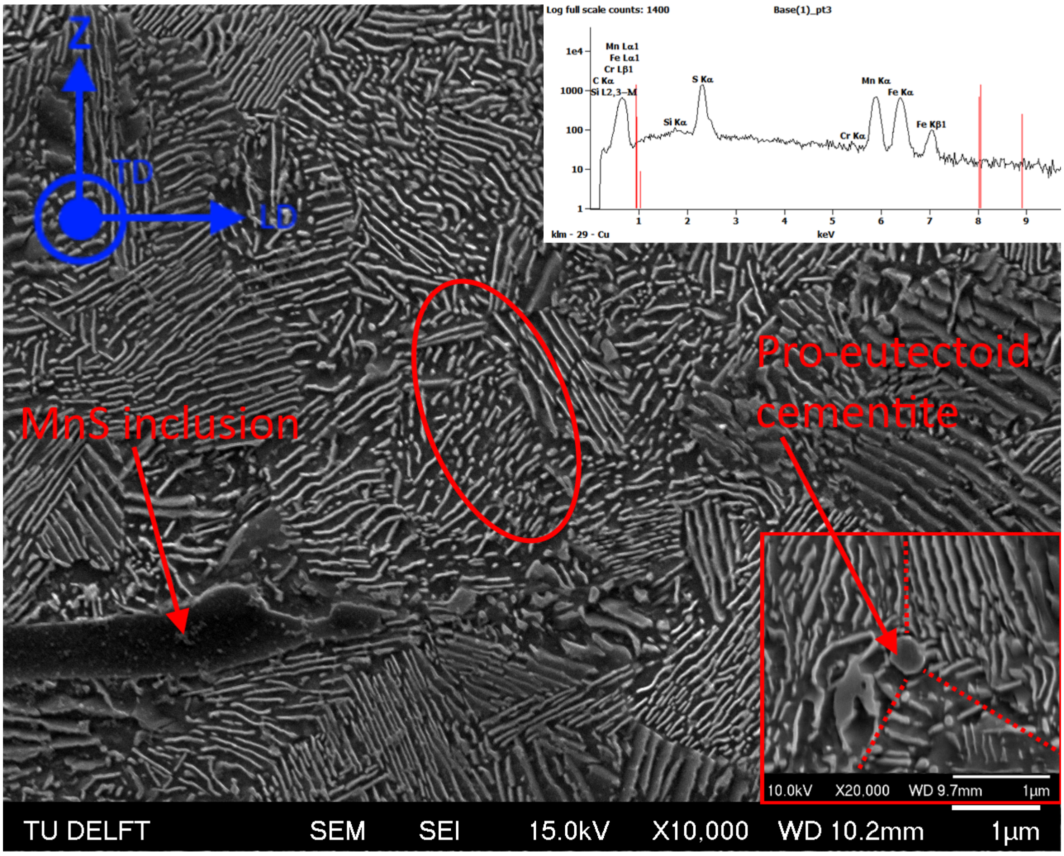

Figure 4.11: *The MHH base material, showing occasional regions of projected cementite (encircled in red), MnS inclusions (EDS spectrum shown in the top right) and pro-eutectoid cementite at the prior austenite grain boundary. These prior austenite grain boundaries are indicated by the red dotted lines in the cut-in figure.*

4.5.2 WEL with deformed pearlite underneath

Figure 4.12 shows WEL with a region of deformed pearlite underneath from the GB. Plastic deformed pearlite (PDP) is identified by the curving of the cementite lamellae. This curvature become sharper closer to the rail surface, suggesting that the amount of plastic deformation increases towards the rail surface. The lamellae below the WEL do not show fragmenting or thinning due to this plastic deformation. A dense martensitic layer suddenly covers the deformed pearlite.

The rapid transition from deformed pearlite to martensite suggest that the nucleation and growth of austenite occurred almost instantly. The presence of plastic deformed pearlite just under the interface with the WEL suggesting that this plastic deformation might have played a role in the formation of the WEL [31]. Individual grains in the WEL are to small to be resolved with SE Imaging. Thinned and fragmented lamellae of dissolving cementite (DC) are seen in the martensitic WEL. These cementite lamellae follow the curvature of the plastically deformed cementite lamellae underneath the WEL-pearlite interface. The number and size of the dissolving cementite lamellae reduces closer to the surface of the rail, until they are to small to resolve with SE imaging. This indicates that the dissolution of the cementite occurred to a larger extent closer to the rail surface.

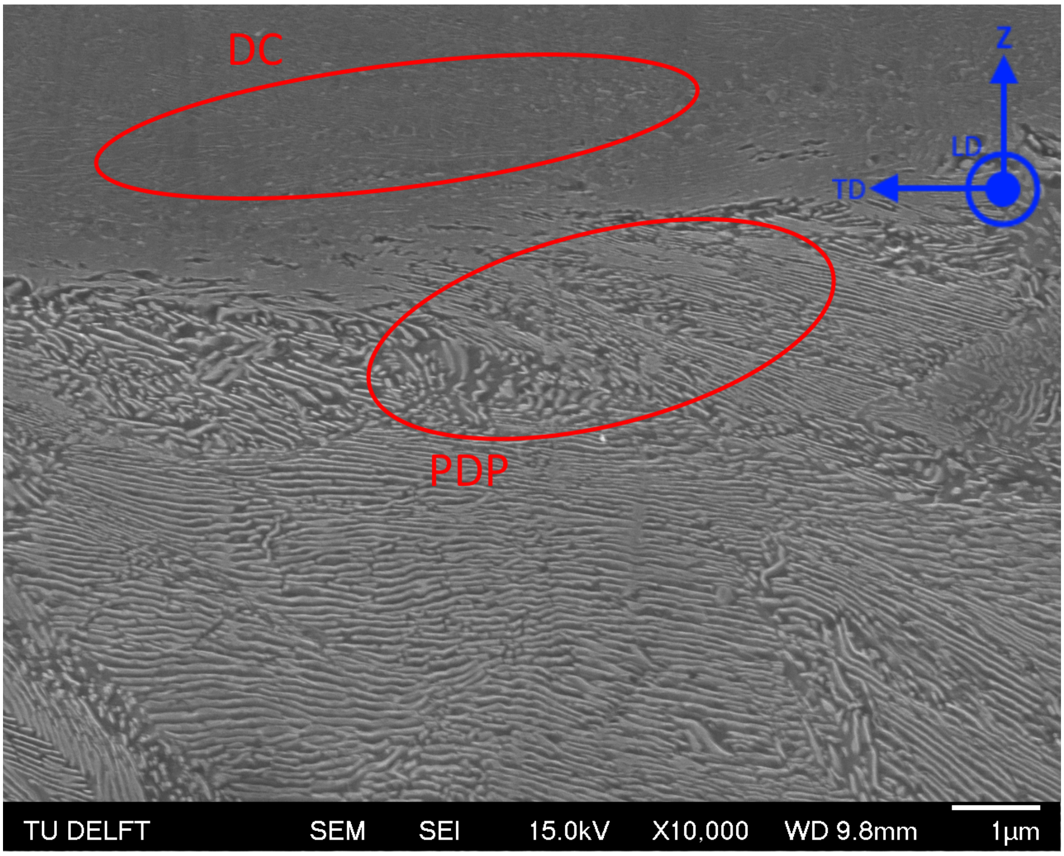

Figure 4.12: *A layer of WEL with plastically deformed pearlite underneath at the GB. Regions of plastically deformed pearlite (PDP) are seen below the WEL/pearlite interface. Dissolving cementite (DC) in the WEL shows thinning and fragmentation and follows the curvature of the PDP below the WEL/pearlite interface.*

4.5.3 WEL without deformed pearlite underneath

Figure 4.13 shows a picture of the WEL pearlite interface in the TCB and confirms the absence of plastic deformation underneath the WEL in this band, since the pearlite lamellae do not show bending. Additionally, several signs of temperature induced phase transformation are observed here. Firstly, The start of austenite formation is seen at the interface of the cementite and ferrite, just below the interface with the WEL (labelled as ”γ” in figure 4.13) [5]. Secondly, at the interface of the WEL, grains of martensite and retained austenite can be seen. These grains increase in size and are more numerous closer towards the rail surface, indicating that austenite nucleation and growth has occurred to a larger extent close to the rail surface. These austenite grains transform to martensite and retained austenite during subsequent cooling, they are thus denoted as ”M/γ” in the figure. Thirdly, the martensitic WEL fully covers the original pearlite as the distance to the rail surface further decrease. This indicates that austenization before quenching was completed above a certain distance to the rail surface. Fourthly, regions of thinned and spheroidized cemen-

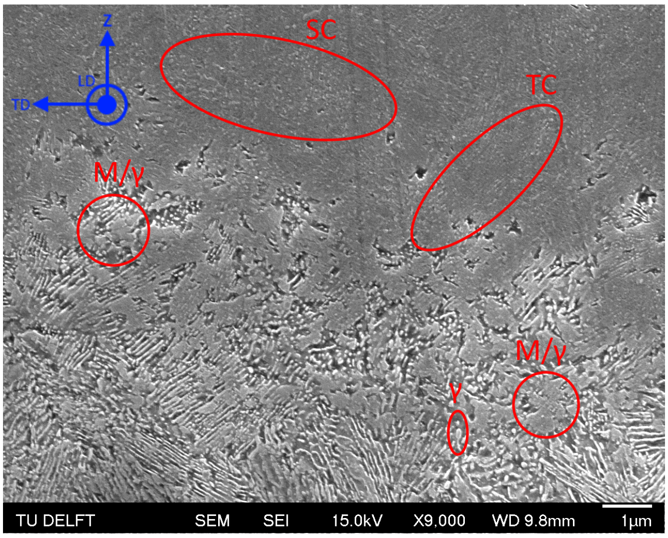

Figure 4.13: *A SE image of the interface between a WEL and undeformed pearlite in the TCB. Grains of austenite are transformed to martensite and retained austenite after quenching. The cementite in the WEL shows thinning (TC) and spheroidization (SC).*

tite are seen within the WEL itself. The thinned cementite (TC) follows the spacing and orientation of the original microstructure. The spheroidized cementite (SC) does not show a clear spacing or orientation. Closer to the rail surface, the cementite had dissolved to such an extent that it could not be resolved with SE imaging.

4.5.4 WEL and BEL in the ground- and secondary contact band

Figure 4.14a shows a region of pearlite underneath stratified WEL and BEL in the GB. Similar microstructure were found in the SCB. The initial stages of austenite growth (γ) can be seen at the tips of the cementite lamellae (marked in red in figure 4.14a). These tips lie at the boundary of a pearlite colony [5]. Figure 4.14b shows the BEL itself. BEL consists of a matrix of partially dissolved pearlite. Grains containing martensite and retained austenite (M/γ) are spread out in this pearlite. Regions of partially dissolved cementite (DC) can be seen in the remaining pearlite. Occasionally, the initial stages of austenite growth can be seen at the dissolving cementite lamellae [5]. Figure 4.14c shows the interface between a BEL and the WEL. The fraction of austenite formed during heating in the BEL increases closer to the rail surface. This results in larger and more numerous grains of martensite and retained austenite after quenching. WEL forms when the complete austenization of the original pearlite has occurred. Subsequent cooling leads to the formation of a continuous layer of martensite and retained austenite. At the interface, the last regions of dissolving cementite and ferrite (DC/α) can be seen besides the martensitic grains.

Dissolving cementite is found in the WEL of the SCB and GB. However, the morphology of this cementite is different in both bands. Partially dissolved cementite in the GB is thinned, but still shows the orientation and spacing of the original lamellae, as shown in figure 4.14d. Cementite lamellae in the SCB are occasionally thinned, while still showing the original orientation and spacing. However, at other locations, the cementite is (partially) spheroidized. These two varients are shown in figures 4.14d and e. This suggests that spheroidization of the cementite only occurs during wheel-rail contacts. Figure 4.14f shows a WEL near the rail surface in the GB. The cementite has dissolved to a further extent closer to the rail surface and can no longer be resolved with SEM. Additionally, retained austenite can no longer be resolved in the martensitic matrix.

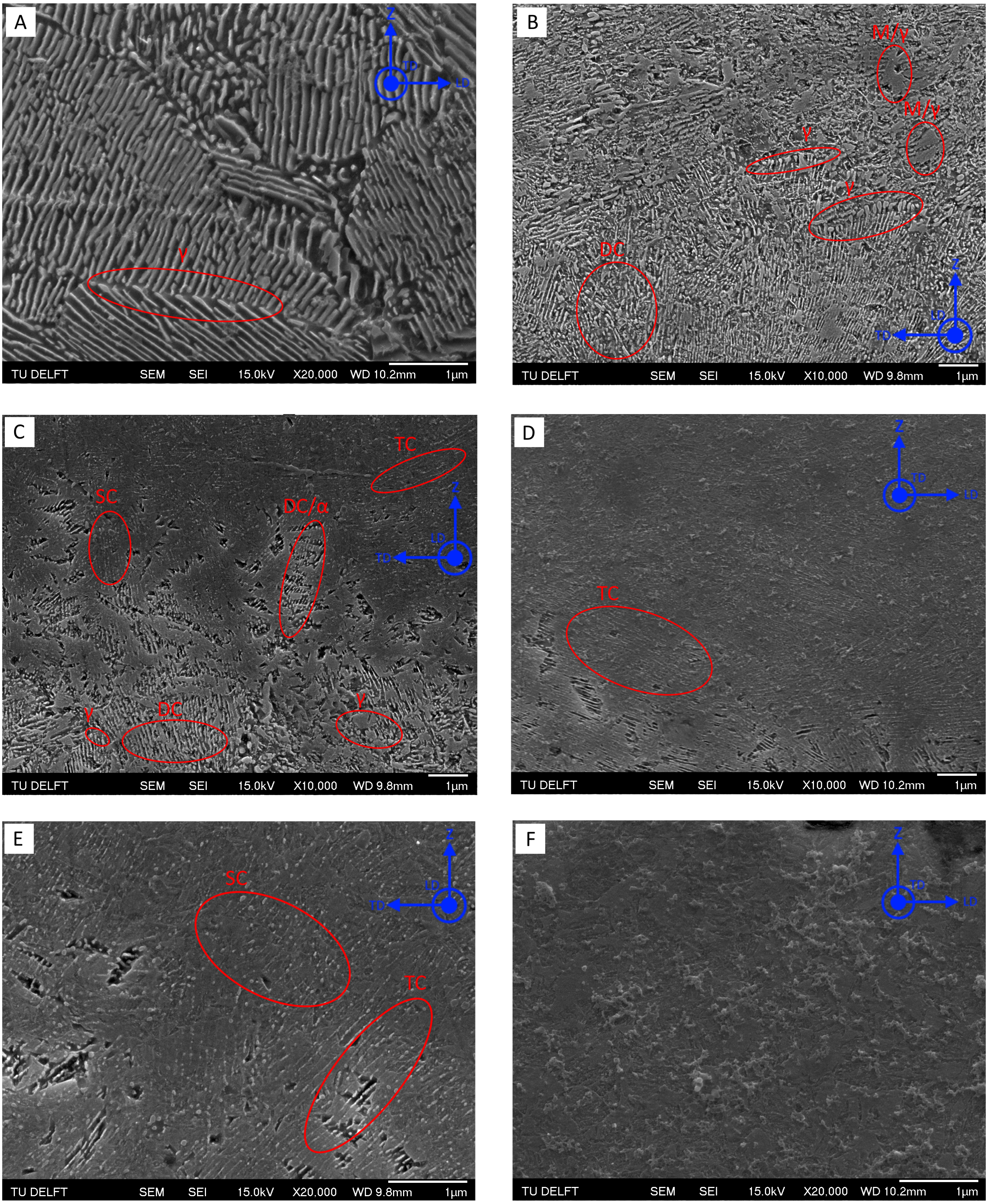

Figure 4.14: *(a): A SEM micrograph of the base pearlite under the BEL in the GB. The initial stages of austenite growth can be seen at the tips of cementite lamellae. (b): A SEM micrograph of the BEL. Grains of martensite and retained austenite (M/γ), austenite formation (γ) and dissolving cemenite (DC) is found in the microstructure. (c): a SEM micrograph of the microstructure at the interface between the BEL and the WEL. Regions of dissolving cementite and ferrite are seen at this interface (DC/α). (d): A SEM micrograph of the WEL in the GB, showing thinned cementite (TC). (e): A SEM micrograph of the WEL in the SCB, showing thinned (TC) and partially spheroidized cementite (SC). (f): A SEM micrograph of a WEL close to the rail surface in the GB. The presence of retained austenite and cementite cannot be resolved with SEM.*

4.5.5 WEL mixed with dissolving pearlite

The optical micrograph of figure 4.6b showed a region of WEL that was mixed with brown splinters in the SCB. Figure 4.15a shows a SE image of the sharp interface between the WEL and the base pearlite at this region. This sharp interface indicates that austenization during heating was almost instant here. During subsequent quenching, a continuous layer of martensite and retained austenite is formed. It can be clearly seen that the cementite in this WEL is thinned and originates from the base pearlite. This cementite was occasionally spheroidized, as was seen else where in the SCB.

The splinters in the WEL that were seen in the optical micrograph of figure 4.6b are encircled in the SE image of figure 4.15b. The splinters in the WEL are regions of dissolving pearlite. This pearlite still sows the lamellar structure of ferrite and cementite. However, the cementite is in a state of dissolution. It is thus suggested that the growing grains of austenite could not fully cover the entire microstructure before cooling occurred, leaving regions of dissolving pearlite between the austenite grains.

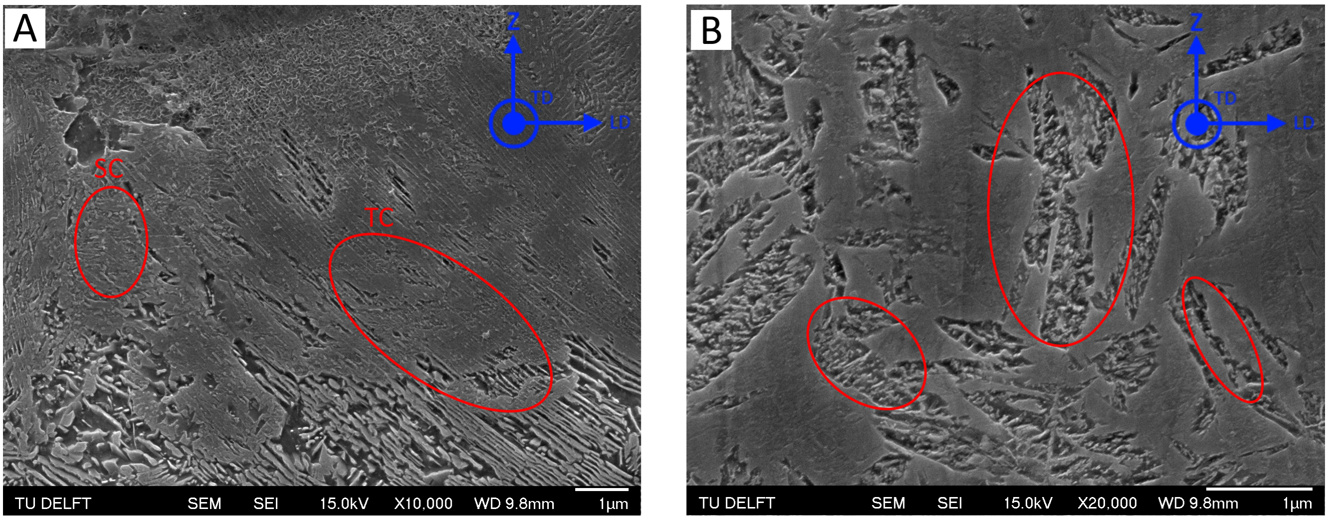

Figure 4.15: *(a): the interface between the WEL and base pearlite, showing thinning of the original cementite (TC) and spheroidization of the cementite (SC) in other regions. (b): The brown, arrow-shaped splinters in the WEL are regions of dissolving pearlite.*

4.6 SEM analysis of Micro cracking at the running surface

Several forms of microcracks were found at the SCB due to WEL formation. Additionally, Cracks were found at regions of deformed pearlite at the rail surface of the PCB. SE Imaging was done to further investigate the morphology of these cracks and to understand the mechanisms of crack initiation and growth.

4.6.1 Cracking at the interface of the WEL and the base pearlite

Figure 4.16a shows a crack growing along the interface of the WEL and the base pearlite in the SCB, as previously shown in figure 4.6c. Only small regions of pearlite are present above the crack, indicating that the WEL/pearlite interface played a critical role in the formation of this crack. No severe plastic deformation can be seen at the pearlite surrounding the crack. Figure 4.16a shows oxidation growing from the crack into the WEL. EDS analysis confirmed that both iron and oxygen were present in the crack and at the oxidation of the WEL, as shown in the spectrum in figure 4.16a. The presence of oxides thus suggests that water was present in the crack at some stage during the service life of the rail [24]. Figure 4.16b shows corrosion of the WEL and the surrounding pearlite at the crack opening at higher magnification. EDS again showed that this corrosion contained iron oxide. The presence of these oxides make it impossible to determine the initiation point of the crack. However, the WEL/pearlite interface curves upwards towards the rail surface, suggesting the crack initiated at the edge of the patch of WEL at the rail surface.

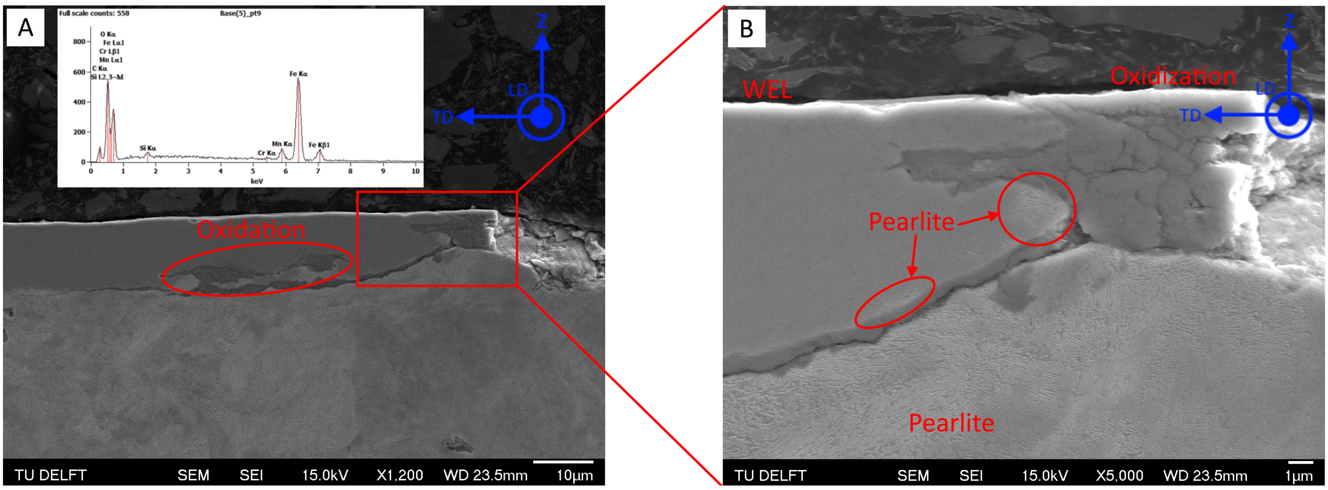

Figure 4.16: *(a): A crack growing at the interface of the WEL and the base pearlite. Oxidation is found at the upper crack flank and in the crack itself. (b): zooming in on the crack opening shows oxidation of both the WEL and the pearlite. Small regions of pearlite are also found above the crack.*

4.6.2 Crack initiation and branching at the primary contact band

Figure 4.17a shows the initial growth stage of a crack at the PCB, previously shown in figure 4.7b. The crack initiates at the rail surface and grows along the curvature of the deformed pearlite lamellae during repeated wheel-rail contacts. Figure 4.17b shows a magnification of the crack opening at the rail surface. EDS analysis showed that only a very limited amount of iron oxides were present in the crack (spectrum shown in figure 4.17b). This indicates that water might not have been present in the crack at this early stage of growth, since water is required for the formation of oxides inside a crack [24]. Figure 4.17b also shows that a region of plastically deformed pearlite (PDP) is found underneath the crack. Spallation of material exists around the crack opening. The material surrounding the crack opening at the rail surface, including the spallation, consist of severely deformed pearlite (SDP). Figure 4.17c shows a magnified SE image of this spallation containing SDP. The cementite lamellae in the SPD are severely deformed in the transverse direction of the rail. This severe plastic deformation causes the lamellae to fragment. Occasionally, spheroidization of the cementite is also observed. This suggests that the cementite is undergoing dissolution. Comparing figure 4.17c to SE imaging by Zhou et al. [89] suggests that the SDP is the initial stage of mechanical WEL formation. EDS analysis (spectrum shown in figure 4.17c) showed that this spalled material had a concentration of Mn, Si and Cr which was similar to the chemical composition of the MHH base steel, as defined in table 3.1. This confirms that the spalled material originated from the base material. Figure 4.17d shows that this severely deformed pearlite also exists at the crack flanks, at a depth of approximatly 11 μm below the rail surface. This suggest that the severe deformation of the pearlite played a role in the initiation and growth of the crack.

Figure 4.17e shows a SE image of the crack previously shown in figure 4.8d, at its point of branching. The branches have have rough and irregular flanks. Furthermore, spallation of material between the two branches and small additional cracks surrounding the central crack are shown in the figure. This suggests that a network of fine cracks exists at the point of branching. Figure 4.17f shows a magnified SE image of one of the crack branches itself. EDS measurements shows that iron oxides are present at the crack flanks and inside the crack itself (spectrum shown in figure 4.17f). This suggest that water has been present in the crack during the service life of the rail [24].

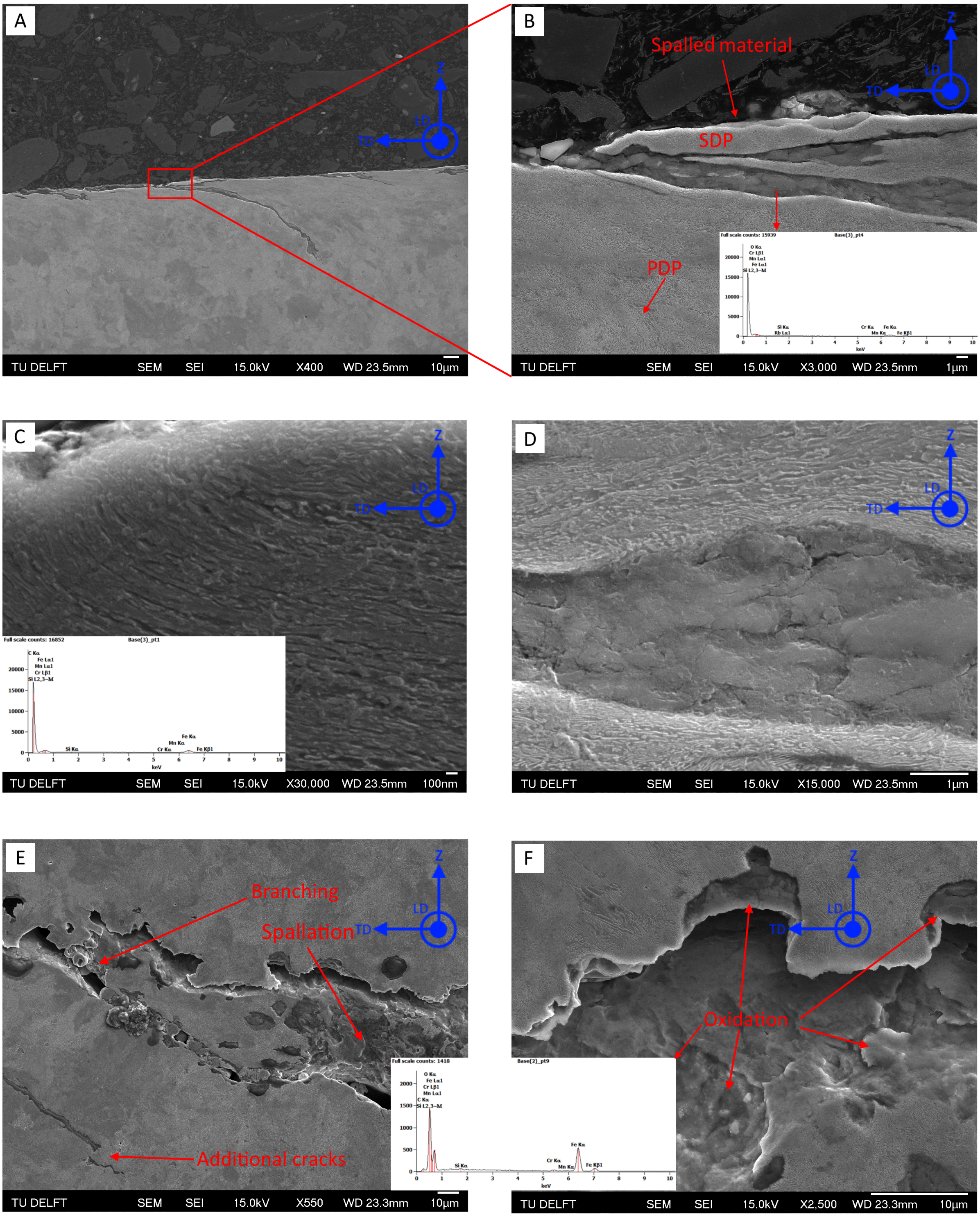

Figure 4.17: *(a): The crack initiation at the rail surface of the primary contact band follows the curvature of the deformed pearlite lamellae. (b): A magnified SE image from (a) shows the initial stages of crack growth, spallation of the material at the rail surface and pearlite in various stages of plastic deformation. The EDS spectrum indicates that iron oxides were only present in a small amount in this crack. (c): A magnified SE image showning the microstructure of the spallation from (b). Severely deformed pearlite shows fragmentation of spheroidization of the cementite laths. The EDS spectrum suggests that this spallation belongs to the MHH base material. (d): Severely deformed pearlite also exists at the crack flanks at a depth of 10 μm beneath the rail surface. (e): A SE image of a network of small cracks at the point of branching of the main crack. (f): A magnified SE image of one of the crack branches. Oxides are found inside the crack, as indicated by the EDS spectrum.*

4.7 X-ray diffraction

4.7.1 Phase identification of WEL

Figure 4.18 shows the XRD spectrum of a large patch of WEL in the TCB. Analysis of XRD spectrum showed that the blue peaks corresponded to BCC iron and that these peaks had the highest intensity of all the present peaks. This indicates that BCC iron was the main phase present in the WEL. Further analysis shows that these blue peaks are slightly asymmetric, suggesting that the BCC iron lattice has two different lattice parameters (a and c) [40]. The peak caused by the c lattice parameter has a smaller intensity than the peak of the a lattice parameter. Additionally, these peaks overlap in the XRD spectrum, thus forming one asymmetric peak [40]. It can thus be concluded that the BCC lattice is slightly tetragonal [40]. This indicates that the main phase in the WEL is martensite, which has a BCT lattice [15, 40, p.414].

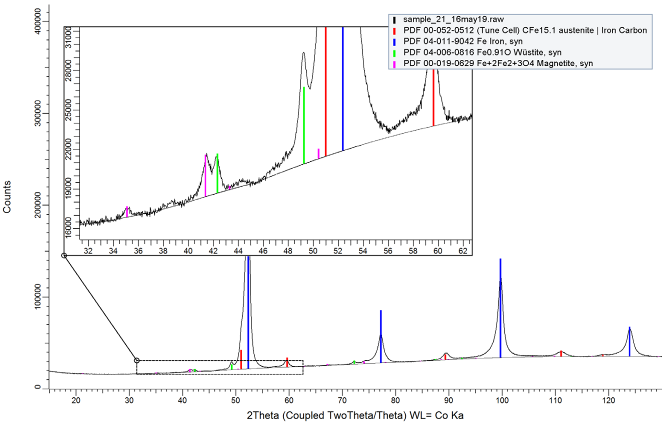

Figure 4.18: *The XRD-spectrum showing the phases present within the WEL at the rail surface of the TCB.*

Retained austenite is identified by the red peaks in the XRD spectrum, proving that at least the A_1 temperature was surpassed during the formation of the WEL. Some of the smaller peaks were identified to be iron oxides such as wüstite and magnetite, which result from corrosion during service. XRD measurements are done at the surface of the specimen. As a consequence, cementite was not identified in the XRD spectrum. This confirms the observation done by SEM that cementite had largely dissolved at the rail surface within the WEL. However, a number of peaks in the XRD spectrum remained unresolved due to there small size. These peaks could indicate the presence of small carbides in the WEL at the rail surface. Unfortunately, the crystal structure of these carbides could not be identified with XRD.

The lattice parameter of the austenite phase was determined to be 3.598 ± 0.004 Å, using a Nelson-Riley plot. A calculation estimates that this lattice parameter relates to an austenite carbon content of approximately 0.90 ± 0.10 wt.% [7, 64], as shown in appendix B2.

4.7.2 Stress analysis using the $sin^2(\psi)$ method

Table 4.2 shows the residual stresses measured in the longitudinal direction of the rail, at its surface. Appendix B2 discusses the determination in peak shift for each of these measurements. The MHH base metal has a residual compressive stress of -190.3 ± 29.0 MPa. This compressive stress is in accordance with the material design and manufacturing process [63, p. 14] and has the advantage of reducing the growth rate of RCF cracks [14], as described in section 2.1.3. The section of the rail surface which underwent only grinding (GB) had a residual tensile stress of 627.4 ± 40.9 MPa. It can thus be concluded that grinding replaces the residual compressive stress of the MHH base material with a large tensile stress. This tensile stress could enhance crack growth and thus counteracts the purpose of the compressive stress at the running surface of the MHH rail. The part of the rail surface which underwent wheel-rail contacts after grinding (SCB) had a residual stress of 223 ± 40.7. Subsequent repeating wheel-rail contacts thus reduces the residual tensile stresses created by grinding over time. However, it cannot be concluded that wheel-rail contacts will completely undo the detrimental effects of grinding since crack damage could initiate at the rail surface before the tensile stresses are sufficiently reduced. Additionally, it cannot be predicted if the residual tensile stresses will reduce completely to zero.

Table 4.2: *The longitudinal stress state at the surface of the original MHH, ground band and secondary contact band.*

Region	**Longitudinal stress [MPa]**
The MHH base metal	-190.3 ± 29.0
The ground band	627.4 ± 40.9
The secondary contact band	223 ± 40.7

Chapter 5: Discussion

5.1 The microstructures of the various WEL and BEL types at the rail surface

Cyclic grinding maintenance causes a temperature increase at the rail surface, leading to the austenization of the base pearlite under the rail surface. The austenization of the base pearlite is complete up to a depth of 40 μm. In this region, quenching after grinding transforms the austenite to a continuous layer of martensite and retained austenite [31], resulting in a White Etching Layer (WEL). The high intensity of the martensite peaks in the XRD spectrum in figure 4.18 indicate that martensite is the main phase present in the WEL. The presence of the martensitic WEL increases the hardness at the rail surface from approximately 400 HV to 1000 HV via several mechanisms. Firstly, the shear transformation from austenite to martensite causes a high dislocation density. The motion of these dislocations is hindered by the high amount of other dislocations and interstitial carbon in the BCT lattice during plastic deformation induced by subsequent wheel-rail contacts [15, p. 413]. Secondly, straining of the BCT lattice is required to accommodate carbon at the octahedral interstitial sites. This can lead to residual stresses in the material [15, p. 418]. It is unlikely that grain refinement has contributed to the hardness of the studied WEL, since this mechanism is only expected to occur when plastic deformation plays a role in the formation of the WEL [1, 39, 50, 89]. SEM only showed a few isolated locations in which the cementite lamellae in the WEL and the underlying pearlite were curved. Thus, plastic deformation at the WEL was limited due to the high yield strength of the original MHH base material. Additionally, grinding induces only a limited amount of plastic deformation compared to wheel-rail loading.

Cementite in the WEL had several morphologies. In the Ground Band (GB) thinned cementite existed under the same spacing and orientation as the lamellae of the original pearlite. This thinning indicates that the cementite has partially dissolved during heating above the A_1 temperature, as discussed in greater detail in section 5.2.2. Wheel-rail contacts after grinding have taken place in the Secondary Contact Band (SCB) and Tertiary Contact Band (TCB). Here, the cementite had partially spheroidized due to the heat input during wheel-rail contacts, as discussed in section 5.3.1. These spheres were found at the locations of the original pearlite lamellae and thus showed the inter lamellar spacing and orientation of the original cementite. Finally, the presence of cementite in the WEL close to the rail surface could not be resolved with SE imaging. Heat induced by grinding diffuses from the rail surface downwards into the material. Thus, the material at greater depth beneath the rail surface requires more time to heat up, resulting in lower peak temperatures at greater depth beneath the rail surface. This peak temperature is sustained for a shorter amount of time at greater depths below the rail surface, as discussed in section 5.2.1. It is thus expected that temperatures during grinding approach, or even surpass, the A_{cm} temperature close to the rail surface, while the temperature at greater depth below the rail surface remain far below the A_{cm} temperature. This only dissolves the cementite close to the rail surface completely or to such a large extent that it can no longer be resolved via SE imaging or XRD.

Occasionally, the base pearlite only partially austenizes since grinding imposes lower temperatures, which are sustained for a shorter amount of time, at the greater depths in the material than at the rail surface. Thus, the A_1 temperature was surpassed to a lesser extent and for a smaller amount of time at an approximate depth of 15 to 60 μm. Consequentially, the microstructure does not fully transform to austenite before quenching to martensite occurs. This results in a Brown Etching Layer (BEL), which consists of martensite, retained austenite and pearlite containing dissolving cementite [31]. Due to heating above the A_1 temperature during grinding, the cementite in this pearlite shows thinning and fragmenting, indicating that it is in dissolution. Additionally, the start of austenite growth is occasionally seen at the ferrite/cementite interface, preferably at the pearlite colony boundary [5]. Finally, the grains of martensite and retained austenite become larger and more numerous closer to the rail surface in the BEL. In these top regions of the BEL, austenization occurred to a larger extent since higher temperatures were sustained for a longer amount of time. WEL forms when these martensitic grains completely cover the original microstructure.

Figure 4.15b shows a region of WEL with splinters of dissolving pearlite. This region additionally shows a sharp transition from the base pearlite to the WEL. It is thus suggested that fast heating of the material in this region caused a rapid transformation of the base pearlite to austenite. However, quenching occurred before the pearlite was completely transformed to austenite. This left narrow regions of heavily dissolving pearlite at parts of the microstructure which were not transformed to austenite. Subsequent quenching transformed the austenite grains to grains of martensite and retained austenite. The regions of dissolving pearlite maintained their microstructure during quenching. The fraction of austenite formed during heating increases closer to the rail surface, due to the higher temperatures and longer heating times sustained here. Thus, the splinters of dissolving pearlite become smaller and less numerous closer to the rail surface. A continuous layer of WEL is formed when the pearlite has completely dissolved during austenization. The hardness of the region of WEL and dissolving pearlite depends on the fractions of WEL and dissolving pearlite and increases as the fraction of pearlite decreases.

Wheel-rail contacts at the Primary Contact Band (PCB) induced a far larger amount of plastic deformation than grinding. The early stages of Rolling Contact Fatigue (RCF) crack growth were observed in these regions of deformed pearlite, indicating that the plasticity of the material had been exhausted via ratcheting [83, p. 12]. Additionally, thinning and fragmenting of the cementite lamellae in the pearlite at the rail surface in the PCB was observed. This cementite dissolution is on of the initial stages of mechanically induced WEL formation, which is a consequence of the large plastic deformation at the PCB.

Mechanically induced WEL is described as a nanostructure of ferrite [1, 39, 50, 89]. Lojkowski et al. [39] report that these ferrite grains have a size of 15-500 nm and thus result in a high hardness. Additionally, a high dislocation density induced by severe plastic deformation attributes to the brittle character of this layer [89]. The motion of these dislocation is hindered by the numerous grain boundaries and other dislocations. The cementite of the original pearlite dissolutes during the formation of mechanically induced WEL and thus has to be facilitated elsewhere in the microstructure [1, 39, 50, 89]. Carbon is only facilitated in a limited amount in the ferrite, giving this phase a crystal structure and properties similar to martensite [39, 89]. Additional carbon is facilitated at the dislocations [39, 50], further reducing their mobility and thus the brittle character of the WEL.

5.2 The formation mechanism of the WEL and BEL

5.2.1 The temperature field induced by grinding

An analytical model was constructed to simulate the temperature field at a fixed point at the rail surface during grinding (see appendix A1.2). Figure 5.1 shows the simulated temperature field during passage of four subsequent grinding stones on one facet, as a function of time and depths below the surface [57, 86]. Frictional heat due to the abrasive action of grinding heats up the material while contact between the fixed point at the rail surface and the grinding stone exists [86]. The power input during grinding is calculated to be 19.6 kW per stone, based on micro roughness measurements of the rail surface and formula 2.2. This calculated power input is still below the maximum power input of 22 kW [65, p. 62]. The cutting depth per grinding stone was calculated to be 0.1 mm and the flash temperature at the grinding stone surface was 1250 $^{\circ}C$. This temperature is imposed on the rail surface and causes a heat flow into the rail material, leading to the temperature field shown in figure 5.1. Quenching occurs after contact with the fixed point at the rail surface and the grinding stone is removed.

Temperatures during grinding exceed the A_1 and A_{cm} temperatures and are thus sufficiently high to cause a thermally driven transformation from pearlite to austenite. Contact exists between a fixed point on the rail surface and the grinding stone for 0.08 s, at the chosen grinding train speed and grinding stone diameter. Temperatures at the rail surface increase to approximately 800 $^{\circ}C$, resulting in an average heating rate of $10^{4\circ}C/s$ at the rail surface. The equilibrium A_1 (725 $^{\circ}C$) and A_{cm} (798 $^{\circ}C$) temperatures were calculated in Thermo-Calc ©and can be surpassed during grinding, as shown in the figure. However, the A_1 and A_{cm} temperatures can increase due to high heating rates [35], delaying the nucleation and growth and of austenite and cementite dissolution. Thus, the thickness of the studied WEL and BEL is smaller than predicted by this model. Additionally, the model shows that the reached temperatures are lower at greater depths below the rail surface since heat will required longer amounts of time to diffuse to these depths. As an consequence, the A_1 and A_{cm} temperatures are surpassed to a smaller extent and for a shorter amount of time at greater depths below the rail surface. This reduces the fraction of austenite formed during heating at these greater depths and thus leads to the stratified morphology of WEL and BEL.

Quenching at the rail surface occurs via the conduction of heat into the rail after contact with the grinding stone is removed. The model shows that the average cooling rate is $6.67 * 10^3$ $^{\circ}C/s$. Thus the material at the rail surface is quenched and martensite is likely to form. If the successive grinding stone on the grinding train is applied to the same facet, reheating occurs before the material has fully cooled down. This increases the maximum temperature at the rail surface during passage of the second grinding stone with approximately 80 $^{\circ}C$, increasing the probability of forming WEL [86]. This additional temperature increase is not seen at the third and fourth grinding stone. The difference between the temperature at rail surface and the flash temperature at grinding stone is reduced due to the higher temperature at the rail surface created by the second grinding stone. This leads to a smaller heat flux during passage of the third and fourth grinding stone, stabilizing the temperature increase. Finally, it is calculated that approximately 100 μm is removed by each grinding stone, which is greater than the maximum layer thicknesses of 60 μm observed during this research. It is thus suggested that the observed layers resulted from the last grinding stone, while previously formed layers are removed.

Several inaccuracies of the analytical model can influence the predicted temperature field during grinding. Firstly, empirically determined constants are used in the formula's for the power input (2.1) and cutting depth during grinding (2.2 and 2.3). These formula's thus only approach the conditions during the grinding maintenance of the studied rail. Secondly, some of the input parameters for calculating the power input and cutting depth during grinding, such as stone mesh size and grinding train velocity, were not measured for this specific grinding maintenance and had to be taken from other reports [65, p. 59]. Thirdly, the heat flow in the rail material is described as an one dimensional semi-infinite conduction problem. The heat conduction coefficient and diffusivity of steel are assumed to be constant in this calculation. The effects of convection and radiation on the heat flow are also not considered in this model. This description can only approach the real heat flow at the rail surface during grinding. Finally, the surface roughness of the ground band is an important input parameter to determine the power input during grinding. This surface roughness can be affected by corrosion during the surface life of the rail. Nevertheless, the temperature field predicted by the analytic model is in accordance with standards for rail grinding and the results presented in this report. The power input and cutting depth predicted by the model are within the set limits for the cyclic grinding maintenance of rails [57, 65]. Additionally, the peak temperatures described by the model surpass the equilibrium A_1 and A_{cm} temperatures of the MHH steel grade, as predicted by Thermo-calc ©. This simulation result confirms that the formation of WEL and BEL at the rail surface is possible during grinding. The model predicts that the equilibrium A_1 temperature is surpassed up to a depth of 100 μm during contact with one grinding stone. This depth is slightly larger than the maximum thickness of the studied WEL and BEL, which was approximately 60 μm. The A_1 and A_{cm} temperatures can increase due to high heating rates during grinding [35]. This increase in A_1 and A_{cm} temperatures is not considered in the model and could explain why the thickness of the WEL and BEL is overestimated by the model.

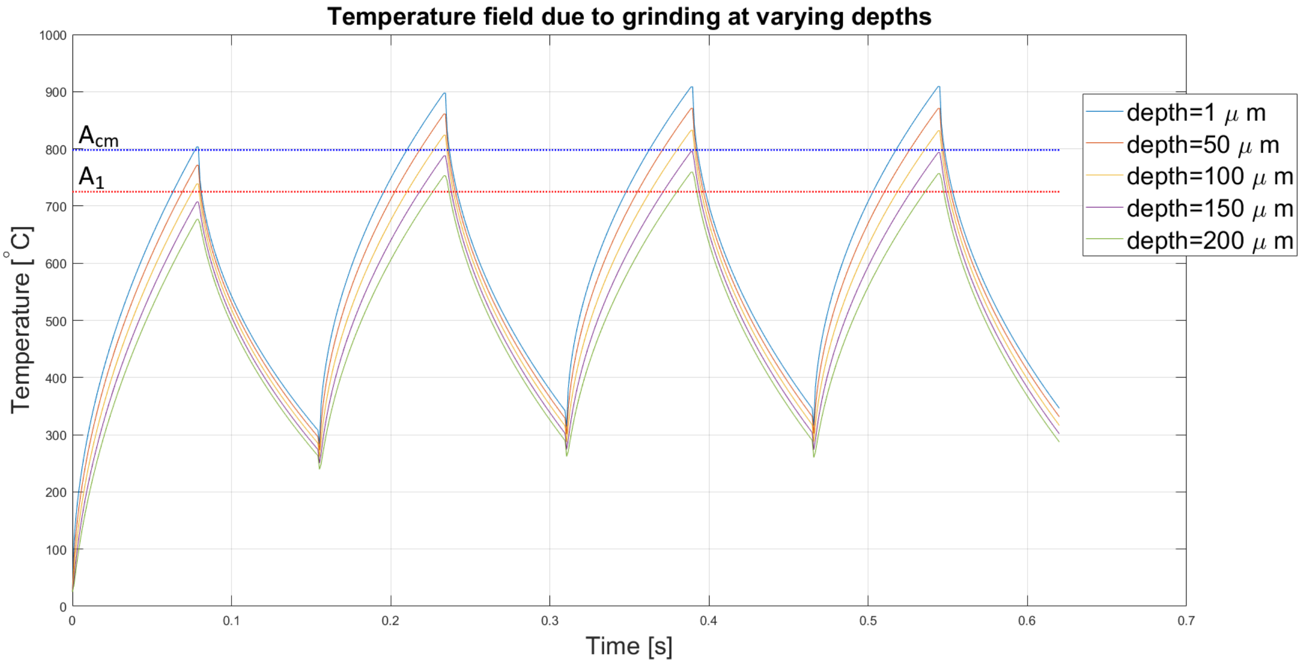

Figure 5.1: *The temperature field created by four successive grinding stones passing on the same facet. Calculations were done as a function of depth below the surface and time.*

It is unlikely that further growth of the WEL and BEL occurred due to wheel-rail contacts at the SCB or TCB after the grinding maintenance. Figure 4.10 showed that tempering of the martensite in the SCB occurred until a maximum depth of 25 μm. Tempering can occur at temperatures far below the A_1 temperature [3, 60], as will be discussed in section 5.3.2. It is thus unlikely that the A_1 temperature was surpassed during wheel-rail contacts at depths greater than the thickness of the pre-existing layer. Thus, growth of the WEL due to austenization and quenching during wheel-rail contacts is unlikely. Additionally, Vampire ©simulations predicts that the amount of creepage during wheel-rail contact is only sufficient for a temperature increase up to 200 $°C$, given that the train was moving at the maximum allowed speed and that no breaking occurred. This simulation result is in accordance with the experimental observation that the temperature increase due to creepage during wheel-rail contacts was only sufficient for tempering of the existing WEL below the A_1 temperature.

5.2.2 Microstructural changes during heating and quenching

As soon as the temperature in the material passes the A_1 temperature, austenite nucleates at the ferrite/cementite interfaces. Cementite is super saturated with carbon in solid solution. Austenite forms to facilitate some of this carbon, thus lowering the carbon concentration of the cementite towards its equilibrium composition [56, p. 261]. The nucleation of austenite preferably occurs at the pearlite colony boundary [5]. A higher Gibbs free energy is present at this combination of a ferrite/cementite interface and pearlite colony boundary [5]. The austenite will grow into the ferrite phase, while thermally driven dissolution of the cementite occurs between the A_1 and A_{cm} temperatures [37]. Carbon is removed from the cementite and diffuses into the austenite lattice [34, 37]. The driving force for this process is maintaining the equilibrium carbon concentration of the cementite [34, 37]. Li et al. [37] reported that residual cementite can spheroidize during austenization if sufficiently high temperatures are maintained for sufficiently long amounts of time. However, WEL in the GB mainly showed thinned cementite, while spherodization dominantly occurs at locations where later wheel-rail contacts took place. It can thus be concluded that the spheroidization of the cementite did not take place during austenization during grinding, but due to the heat input during repeating wheel-rail contacts afterwards. Section 5.3.1 will discuss this process in greater detail.

Quenching of the material occurs after contact with the grinding stone is removed. Thermo-Calc ©simulations show that for the given austenite carbon content 0.90 ± 0.10 wt.%, approximately 90% of the austenite is transformed to martensite during quenching to room temperature (see section 4.1). The remaining austenite will be retained. However, the true fraction of martensite could be much lower than predicted by Thermo-Calc ©. A hydrostatic pressure will be exerted on the austenite, due to a 4% increase in specific volume when transforming austenite to martensite [7, 48]. This hydrostatic pressure stabilizes the austenite [48] and hinders the formation of martensite. Thermo-calc ©simulations did not account for this hydrostatic pressure.

5.2.3 The influence of the MHH steel grade on the formation of WEL

Several aspects of the MHH base material will enhance the formation of austenite, while others will hinder it. Firstly, the inter lamellar spacing of MHH (100 nm) is small compared to other steel grades, such as R260Mn (150 nm [83, p. 68]) and R350HT (150-200 nm [31]). The area of the ferrite/cementite interface per unit of volume increases due to the small inter lamellar spacing, thus increasing the number of nucleation sites for the austenite. Additionally, the smaller inter lamellar spacing reduces the effective diffusion distance of carbon during austenization [36]. The diffusion of carbon is the rate limiting aspects of the pearlite to austenite transformation [34, 37]. Thus, the smaller inter lamellar spacing of the MHH microstructure will increase the fraction of austenite after heating to an absolute temperature, when compared to a material with a larger inter lamellar spacing. On the other hand, the chemical composition of the MHH will hinder the formation of austenite and dissolution of cementite. The A_1 and A_3/A_{cm} temperatures of MHH (725$°C$ and 798$°C$) are higher than those of R260Mn (700$°C$ and 722$°C$ [83, p. 70]) and R350HT (715$°C$ and 730$°C$ [31]). Thus MHH is expected to have a lower fraction of austenite and higher fraction of residual cementite during heating to an absolute temperature, when compared to R260Mn and R350HT. Finally, the high chromium content of the MHH steel grade (as shown in table 2.1 [12, p. 21]) could hinder the dissolution cementite during austenization. Li et al. [34] and Li et al. [37] mention that chromium is mainly facilitated in the cementite and stabilizes this phase during austenization, resulting in a higher A_3/A_{cm} temperature for the MHH than for other pearlitic rail steel grades with a lower chromium content. Thus, the WEL formed in the MHH could have a higher fraction of residual cementite than WEL found in other steel grades presented in table 2.1. Thermo-Calc ©support this theory since removal of the chromium from the MHH steel composition lowers the A_{cm} temperature from 798 $°C$ to 745 $°C$. However, no measurements were done on the studied WEL during this research to confirm if this mechanism is actually at work in the studied WEL.

The classical nucleation theory can be used to estimate if the nucleation rate of austenite in MHH is higher or lower than the nucleation rate of R260Mn or R350HT at a given temperature. The smaller inter lamellar spacing of MHH is expected to increases the number of nucleation sites and thus the nucleation rate. However, the chemical composition of the MHH increases its A_1 and A_3/A_{cm} temperatures. The higher A_1 temperature is expected to decrease the driving force for nucleation and thus the nucleation rate. The classical nucleation theory estimates the nucleation rate as [56, p. 265]:

$$\frac{dN}{dt} \propto N_0 * C_0 * exp\left(\frac{-\Delta G^*}{K * T}\right) \tag{5.1}$$

Where N_0 is the concentration of nuclei with a super critical size [56, p. 264]. A nucleus will only be stable if it exceeds this critical size [56, p. 191]. C_0 is the number of atoms in the nucleus per unit of volume [56, p. 264]. K is the Boltzmann constant and T is the absolute temperature in Kelvin. ΔG^* is the activation energy for the formation of a nucleus with a critical size and can be written as [52]:

$$\Delta G^* = \frac{\Psi}{\Delta g_v^2} \tag{5.2}$$

The nucleation of austenite removes a section of the ferrite/cementite interface. Additionally, a new ferrite/austenite interface and a new cementite/austenite interface are created during nucleation. Ψ quantifies the balance between the energy released by removal of the old interface and the energy required to form the new interfaces during nucleation [52]. This parameter is assumed to be constant for MHH, R260Mn and R350HT since the nucleation of austenite is expected to dominantly occur at the ferrite/cementite interface for all three of these steel grades. Δg_v gives the difference in Gibbs free energy per unit of volume between the new austenite phase and the old ferrite or cementite phase. This difference in Gibbs free energy is released during the formation of an austenite nucleus. Δg_v thus gives the driving force for the nucleation process. Thermo-Calc ©shows that the MHH microstructure consists of 11.6 % cementite and 88.4 % ferrite (figure 4.1). It is thus assumed that the difference in Gibbs free energy between the austenite and the ferrite will be the dominant driving force. This driving force is linearly proportional to the temperature increase above the A_1 temperature [20, 52, 56, p. 190]:

$$\Delta g_v = \alpha * \Delta T \tag{5.3}$$

ΔT is the difference between the absolute heating temperature and the the A_1 temperature in Kelvin. ΔT will decrease if the A_1 temperature of the steel grade increases, while the absolute heating temperature remains constant. Thus, a steel grade with a higher A_1 temperature will experience a smaller driving force for austenite nucleation during heating above the A_1 temperature. α depends on the chemical composition of the old ferrite or cementite phase and the new austenite phase. α is difficult to determine via experiments [20, 52]. Thus, the MHH, R260MN and R350HT steel grades are simplified to binary Fe-C systems with carbon contents as specified in table 2.1. All other atoms are assumed to be iron. The carbon concentration of these three simplified steel grades varies between 3.0 at.% and 3.5 at.%. The presence of carbon lowers the Gibbs free energy of the material via the entropy of mixing [56, p. 14]. It is assumed that the variation in carbon content of the three steel grades has a negligible influence on the entropy of mixing and thus the Gibbs free energy of the three steel grades. Therefore, α is assumed to be constant for all three steel grades.

The MHH steel grade is simulated as a material with an inter lamellar spacing of 100 nm (section 4.5.1) and a A_1 temperature of $725°C$ (figure 4.1). The nucleation rate of MHH is given by using formula 5.1:

$$\frac{dN_{MHH}}{dt} \propto N_0 * C_0 * exp\left(\frac{-\Psi}{\alpha^2 * K * T * (\Delta T_{MHH})^2}\right) \tag{5.4}$$

The R260Mn and R350HT steel grades are represented by a "Conventional Steel Grade" (CSG). It is assumed that this conventional steel grade has a inter lamellar spacing of 150 nm [83, p. 68], which is 3/2 times larger than the inter lamellar spacing of the MHH. It is assumed that the number of austenite nucleation sites is constant per unit of ferrite/cementite interface area. The total ferrite/cementite interface area per unit of volume decreases as the inter lamellar spacing increases. Thus, the larger inter lamellar spacing of the conventional steel grade reduces the number of nucleation sites with a factor 2/3. The A_1 temperature of the conventional steel grade is assumed to be $700°C$ [83, p. 70]. The nucleation rate of conventional steel grade can thus be given as:

$$\frac{dN_{CSG}}{dt} \propto \frac{2}{3} * N_0 * C_0 * exp\left(\frac{-\Psi}{\alpha^2 * K * T * (\Delta T_{CSG})^2}\right) \tag{5.5}$$

Where $\Delta T_{CSG} = \Delta T_{MHH} + 25$, given that the absolute heating temperature is constant. Combining formula 5.4 and 5.5 gives the ratio between the nucleation rate of the MHH steel grade and conventional steel grade:

$$\frac{dN_{MHH}/dt}{dN_{CSG}/dt} \propto \frac{3}{2} * exp\left(\frac{\Psi}{\alpha^2 * K * T} * \left((\Delta T_{CSG})^{-2} - (\Delta T_{MHH})^{-2}\right)\right) \tag{5.6}$$

The nucleation rate of MHH is smaller than the nucleation rate of the conventional steel grade if this ratio is smaller than 1. In this case, the reduction of the austenite nucleation rate of MHH due to the higher A_1 temperature will be larger than the increase in nucleation rate due to the larger number of nucleation sites. $\frac{dN_{MHH}/dt}{dN_{CSG}/dt}$ is smaller than 1 if the exponent in formula 5.6 is smaller than $-ln(2/3)$. Thus, the absolute heating temperature required for the nucleation rate of austenite to be lower in MHH than for conventional steel can be found by numerically solving the following equation for T:

$$\left(T - A_1^{MHH} + 25\right)^{-2} - \left(T - A_1^{MHH}\right)^{-2} < \frac{-ln(2/3) * \alpha^2 * K * T}{\Psi} \tag{5.7}$$

The found value of T is only valid if T is higher than the A_1 temperature of MHH and lower than the temperatures at which the MHH or the conventional steel grades enters the austenite/liquid region in the Fe-C phase diagram. The nucleation rate of austenite will be higher in MHH than in the conventional steel below the found value of T. The value of T cannot be fully quantified since the values of Ψ and α are unknown. Further research will be required to experimentally determine these parameters for the nucleation of austenite in pearlitic rail steel grades.

5.2.4 The role of plastic deformation during the formation of WEL

Plastic deformation plays only an minor role in the formation of WEL. The small inter lamellar spacing of the MHH steel grade causes a high hardness [59]. Additionally, grinding induces only a small amount of plastic deformation when compared to wheel-rail contacts. Thus, in only a few cases does plastically deformed pearlite surround the WEL. This plastic deformation enhances the dissolution of cementite via the several mechanisms proposed in the literature [82]. Firstly, plastic deformation causes an increase in the number of vacancies in the ferrite, which can facilitate carbon from the cementite [72]. Secondly, plastic deformation of the softer ferrite leads to strain incompatibilities with the harder cementite, leading to the fragmentation of the cementite. The smaller, fragmented cementite particles become unstable due to the Gibbs-Thomson effect and will thus dissolve [33, 61, 72]. However, SE imaging did not show fragmentation of cementite at the interface of the WEL and plastically deformed pearlite in the GB. It is unlikely that this mechanism played a role in the formation of WEL during grinding. A third mechanism for the literature describes that dislocations at the ferrite/cementite interface during plastic deformation [22, 31]. These dislocations can interact with the carbon in the cementite in two ways. Carbon can diffuse into the ferrite via the high diffusion path provided by a dislocation [31, 72]. Additionally, when a dislocation cuts a cementite particle, this interaction causes the carbon to be dragged along by the dislocation, transporting them into the ferrite matrix [49]. It is likely that dislocations aided in the dissolution of cementite at locations were plastically deformed pearlite was observed at the interface of the studied WEL. However, this contribution cannot be quantified since no dislocation density measurements were done in this study. A final balistics model by Ivanisenko et al. [22] describes that the ferrite acts as a visco-elastic medium compared to the hard cementite. The ferrite could erode parts of the cementite away during plastic deformation. However, it is uncertain if this mechanism played a role in the formation of WEL due to grinding, since only a limited amount of plasticity was observed in the studied cases.

5.3 Microstructural changes during service

5.3.1 Spheroidization of the cementite in the WEL

Spheroidization of residual cementite in the WEL in the SCB and TCB occurs due to the heat input during repeating wheel-rail contacts. These spheres are mostly located at the location of the original cementite lamellae and still show the same orientation and spacing, as shown in figure 4.14e. These cementite sphere thus likely originate from the original lamellae [28]. The lamellar structure of pearlite gives a high ferrite/cementite interface area per volume of material. Formation of spherical cementite particles can lower this interface area [28], resulting in a lower Gibbs free energy per unit of volume. Spheroidization occurs in three steps during heating below the A_1 temperature [28]. Firstly, the cementite fragments via the growth of ferrite channels into the lamella [19, 28]. Secondly, the formed fragments assume an elliptic shape, finally forming perfect spheres. The last step consists of the growth of large particles via the shrinkage of smaller particles [28]. Carbon from these small particles diffuse to the larger particles and thus further reduce the amount of ferrite/cementite interface area in the material [28]. These steps are diffusion controlled and thus require the material to be at elevated temperatures for a sufficient amount of time [19, 28]. Individual wheel-rail contacts can provide the temperatures required for cementite spheroidization [47] for only a short amount of time. However, this heating cycle is repeated at each wheel-rail contact. Thus, the spheroidization process is expected to occur step-wise with each repeating wheel-rail contact. The fraction of spheroidized cementite in the WEL is thus expected to increase during the service life of the rail.

5.3.2 Tempering of the martensite

Tempering of the martensitic WEL in the SCB reduce the original hardness of the WEL at the rail surface from 1000 HV to 850 HV. The temperatures during wheel-rail contact was estimated to be 200°C in section 4.2. Tempering of the martensite can occur at this temperature. Tempering reduces the brittleness of martensite, for example via the redistribution of carbon [3, p. 237]. Tempering occurs via several mechanisms. Firstly, carbon will be diffuse from its interstitial lattice sites in the martensite and redistributed to low energy defect sites in the martensite such as vacancies, dislocations and grain boundaries [32, 60]. Kumar et al. [32] reported that this segregation mechanism does occur in WEL. However, for the studied case it is expected that other tempering mechanisms are also at work since this mechanism is only expected to facilitate up to 0.2 wt.% of carbon [60], which is far lower than the carbon content of the rail specimen (0.78 wt.%). A second mechanism is the removal of carbon from the lattice by forming carbides. ε and η carbides form at temperatures between 100 °C of 250 °C [60]. At temperatures above 250 °C, χ carbides form [60]. These carbides subsequently transform to cementite, which will form in a lath-shaped pallets at twins and martensite plate interfaces [3, 60, p. 238]. Spheroidization and rapid coarsening of the cementite will occur if temperatures between 300 °C and 400 °C are sustained [3, 60, p. 238].

In section 4.2 it was mentioned that wheel-rail contacts induced a temperature of 200 °C at the rail surface. This temperature is sufficient to form ε and η carbides. However, the presence of these spherical-shaped carbides could not be proven via SEM, due to their small size of approximately 2 nm [60]. Additionally, no cementite was observed at the rail surface with XRD or SEM techniques. It is thus likely that the formation of new carbides during the tempering of the studied WEL remained limited to nano-scaled ε and η particles. Further characterization of the WEL would be required to give confirmation on the formation of these carbides.

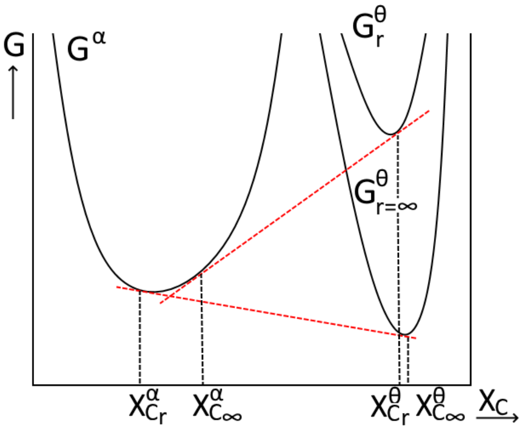

Figure 5.2: *The material can reduce its energy by growth of the cementite spheres in the martensite, reducing the interface energy and relieving the martensitic matrix.*

Spheroidization of the cementite was observed in SE imaging in WEL which underwent wheel-rail contacts after grinding. Growth of the spheroidized cementite in the WEL via the uphill diffusion of carbon from the martensite could aid in the tempering process [3, p. 244]. The driving force for this growth process comes from the Gibbs free energy gain of lowering the carbon content in the martensite and increasing the radius of the cementite particles, as schematically shown in figure 5.2. This process is known as the Gibbs-Thomson effect. Growth of the cementite is expected to occur between 300 $^\circ C$ and 400 $^\circ C$ [3, p. 244]. These temperatures are higher than the temperature of 200 $^\circ C$ estimated during wheel-rail contact. It is thus expected that tempering of the martensite via growth of the spheroidized cementite only took place in cases where higher creepage of the wheel occurred, for example due to breaking of the train.

Two final martensite tempering mechanisms are the decomposition of retained austenite into a mixture of ferrite and cementite, and recovery and recrystallization [3, 60]. These mechanisms take place at temperature ranges of $200^\circ C$ to $300^\circ C$ and above $400^\circ C$ respectively [60]. The decomposition of retained austenite will cause carbon from the martensite to be facilitated at particles of cementite [3, p. 242]. Recovery and recrystallization reduces the dislocation density and forms lath-shaped ferrite grains and spheroidal cementite particles [3, p. 245]. In Secondary Electron (SE) imaging, no evidence for these mechanisms was found. The decomposition of austenite will only occur after the formation of ε, η and χ carbides is at a developed stage [60]. Recovery and recrystallization are unlikely due to the high temperatures required for these processes [60]. It is thus unlikely that these processes played a role in the tempering of the studied martensitic WEL.

5.3.3 Formation of mechanically induced WEL

At the most severely wheel loaded section of the PCB, pearlite was found to be severely deformed, leading to the initial stages of mechanically induced WEL formation, as shown in figure 4.17c. During this process, the ferrite phase in pearlite undergoes grain refinement due to plastic deformation and forms a hard a brittle nanostructure [1, 39, 50, 89]. The cementite undergoes dissolution via the mechanical mechanisms that were already described in section 5.2.4. Carbon from the cementite is believed to be mainly facilitated in the dislocations, which pile up at the ferrite-cementite interface during the cementite dissolution process [39]. The solid solution of carbon in the ferrite lattice is mentioned [39, 89], but is expected to be limited due to the low solubility of carbon in ferrite. The formation of austenite and dissolution of the cementite due to heating above the A_1 temperature did not play a role in the formation of this WEL. Vampire ©simulations showed that the amount of slip during wheel-passage over this rail specimen is 0.628 %. This amount of slip is expected to be insufficient to elevate the temperatures in the wheel-rail contact patch above the A_1 temperature [47]. Finally, it must be noted that the formation of this type of WEL is still in its early stages. Remnants of the original pearlite lamellae can still be observed in the WEL, as shown in figure 4.17c. The dissolution of the pearlite and the growth of the mechanically induced WEL are expected to have occurred to a larger extent if the rail specimen would have experienced a larger number of wheel-rail contacts.

5.3.4 Corrosion of the surface layer

Corrosion of the WEL was most dominant at the surfaces that only experienced grinding. These surfaces had a high surface roughness and thus provided many sites for water entrapment, causing localized corrosion. The corrosion of the WEL itself had a pitting character, suggesting that microstructural defects initiate the corrosion. Surfaces that had experienced wheel-rail contacts after grinding showed far less corrosion damage, since surface irregularities and corrosion initiation were constantly removed by wear.

5.4 Fatigue properties of freshly ground rail surfaces

The cyclic grinding maintenance studied in this work is detrimental for the fatigue properties of the running surface of a rail [67]. The first factor that contributes to this is the high surface roughness created by the grinding. These surface irregularities might act as stress concentrations and thus could be initiation sites for cracks [63, p. 50]. Pitting corrosion due to water trapped at these surface irregularities can further increase these stress concentrations.

Secondly, the stress state induced by grinding further reduces the fatigue properties of the rail surface. The initial residual longitudinal compressive stress, a design feature of the MHH material to prevent fatigue cracking, was replaced by a residual longitudinal tensile stress after grinding. This stress state could enhance the growth of fatigue cracks. Several factors might have contributed to the creation of this tensile stress. Firstly, thermal expansion and shrinkage of the material during heating leads to residual thermal stresses. Secondly, a phase transformation from austenite to martensite during grinding will lead to specific volume changes, causing a tensile stress in the material surrounding the WEL [7]. Furthermore, it must be considered that grinding can also create plastic deformation at the rail surface. This deformation can be the first step in the plastic shakedown of the material, reducing the remaining plasticity of the material.

Wheel-rail contacts after grinding reduces the tensile stress at the rail surface via tempering of the martensite. Additionally, wheel-rail contacts can remove the top layer of the material by wear, changing the stress state in the surrounding material. Furthermore, wheel-rail contacts causes compressive stresses in the rail material [63, p. 75] due to the weight of passing trains. The residual tensile stresses at the running surface of the rail can be counteracted when the compressive stresses by wheel-rail contact are sufficient to cause compressive plastic straining. Although the tensile stresses are reduced over time, crack initiation and growth can occur before these stresses are reduced to a sufficiently low level.

5.5 Crack initiation and development

Crack initiation occasionally occurs at WEL at the rail surface. WEL have a low fracture toughness [32, 62], resulting in a low critical defect length required for further growth of initiated cracks [62]. Surface irregularities such as grinding marks [63] and pitting corrosion at the WEL can increase the probability of crack initiation and growth in the WEL. Subsequent growth occurs at a 45 ° angle with the rail surface due to the stress field induced by wheel-rail contact [84]. The crack reduces its angle with the rail surface as it experiences a changing stress fields at increasing distance from the wheel-rail contact point [84]. Spallation of the material above the crack can occur if the crack continues to grow in a horizontal direction, thus removing the WEL from the rail surface.

Crack initiation at the PCB could not be linked to WEL induced by grinding, since these layers were removed by wheel-rail contacts after grinding. Figure 4.7b showed that cracks at the PCB follow the curvature of the surrounding plastically deformed pearlite in their initial stages of growth. It is thus believed that ratcheting is the driving mechanism of crack initiation at this section of the running surface. During ratcheting, strain is accumulated until rupture of the material occurs [84]. Defects, precipitates, grain boundaries, surface irregularities can act as a initiation point for the crack [84]. Additionally, the initial stages of mechanically induced WEL formation were observed at the crack flanks at the rail surface. These WEL could have acted as a brittle region in the material [39], thus enhancing crack initiation at this location. Additionally, the tensile stress created by grinding might aid in the initiation of cracks at the PCB [84]. The presence of water in these crack could not be determined due to the absence of oxides. It is thus suggested that crack flank lubrication [84] did not play a role in the growth of these cracks.

The reason for initiation of the larger cracks at the PCB (figure 4.7a) cannot be determined. It is possible that these cracks were initiated before the last cyclic grinding maintenance and that complete removal of the crack during this maintenance did not occur. However, the initiation points of these cracks have already been removed by wear due to wheel-rail contacts and possibly material removal during the last grinding maintenance. Initial growth of the crack at the PCB occurs at an angle of 20° to 45° [84] and continued in this direction, due to mode I and II loading by compressive and shear stresses created by wheel-rail contact [84]. Plastic deformation of the pearlite surrounding the crack suggests that initial growth occurred due to ratcheting.

Crack growth after initiation will initially accelerate, due to mode I and II loading[84]. As the crack propagates further away from the surface, growth is expected to slow down again [84] due to friction exerted between the crack flanks [10, 63, p. 22]. However, oxides were found inside the cracks in the studied rail specimen, at this stage of growth. Oxides are only expected to form when water is present in the crack during its service life [24]. Liquids reduce the friction between crack flanks [84] and exert an extra mode I type loading on the crack when compression occurs. Formed corrosion products can aid in this, since they have a larger volume than the original metal [24]. Thus, crack growth is expected to accelerate due to the presence of liquids [84].

Cracks tend to grow away from the regions with high stress and can reduce their angle with the rail surface, since the stress field induced by wheel-rail contact changes at increasing distance from the wheel-rail contact point[84]. Mode I loading, induced by bending and shear stresses due to wheel-rail contacts and residual stresses in the rail, becomes the driving crack growth mechanism [84]. At this stage, branching of the crack can occur if the crack growth rate is sufficiently high [84]. This high growth rate can be caused by caused by residual stresses in the rail, large tangential forces due to traction or braking of the train and a low crack flank friction, possibly due to the presence of water in the crack [84]. Branching is thus an attempt of the material to dissipate the energy over several crack tips [42]. Branches could bend upwards, causing spallation of the material when reaching the surface. This can cause surface irregularities and increase dynamic loading by passing trains [67]. Another possibility is that branches bend downwards due to residual tensile stresses in the rail and grow towards the web of the rail, leading to fracture of the entire rail when exceeding the critical crack length [84]. Another possibility is crack tip shielding by other branches, which prevents further growth of some of the branches [10]. Finally, crack growth could be retarded or even arrested if the stress concentration at each of the crack branch tips is lower than the stress intensity of a single crack with the same projected length [42]. However, in the studied case crack growth has not developed far enough to predict which of these possibilities is most likely to occur [63, p. 52].

5.5.1 Spallation of the WEL during wheel-rail contacts

Cracks grow at the interface between the WEL and the base pearlite in the SCB due to stresses induced by wheel-rail contacts (figure 4.6c). Stratified layers of WEL and BEL did not show this type of cracking. Finite Element Analysis (FEA) modelling, as described in appendix A1.3, was used to gain more insight in this phenomenon. It was found that the yield strength of the WEL (estimated as 1500 MPa [79]) and the base pearlite (830 MPa [14]) are surpassed when simulating loading at the SCB. The maximum amount of plastic strain in the WEL (0.003) occurred at the rail surface and decreased to 0.0015 at the WEL/pearlite interface. The base pearlite showed a large peak in plastic strain (0.0065) at the WEL/pearlite interface. This amount of plastic strain also decreases when moving away from the rail surface, since the stresses induced by wheel-rail contact are lower here. The plastic strain of the base pearlite was 0 at a depth of approximately 210 μm. The peak of plastic strain at the WEL/pearlite interface suggests that cracks form here due to ratcheting of the base pearlite during repeating wheel-rail contacts. Figure 4.6c and d confirm that cracks grow at a depth where the FEA model predicts the largest plastic strain. Yielding of the WEL is less extensive and will not occur at lower applied stresses, while yielding of the pearlite at the WEL/pearlite interface still occurs. Thus, crack formation at the WEL/pearlite interface is more dominant than at the WEL itself under the simulated conditions.

The difference of yield strength between the WEL and softer steel grades, such as R260, is even larger than for the MHH [67]. Thus, ratcheting of the base pearlite and spallation of the WEL via crack growth at the WEL/pearlite interface might occur to an even greater extent in these steel grades [67]. However, it cannot be guaranteed that WEL will spall out of the rail surface before causing damage. RCF cracks can still be initiated at the WEL and grow into the rail head before spallation of the WEL occurs [84].

Additionally, the FEA model showed that plastic straining of stratified layers of WEL, BEL and base pearlite was lower, while the applied loads were identical. BEL is a combination of WEL and base pearlite and was thus simulated as a 50%-50% mixture of WEL and base pearlite. The mechanical properties of the BEL were calculated by applying the lever rule to the material properties of the WEL and base pearlite. Table 4.1 shows that the thickness of a stratified layer of WEL and BEL is larger than the thickness of a single WEL. Thus, adding the BEL gives an additional layer with a higher yield strength than the base pearlite. As a consequence, the BEL partially accommodates the stress previously accommodated by the WEL or the base pearlite. This lowers the stress at the WEL just below its yield strength and thus prevents plastic straining of the WEL. The yield strengths of the BEL and base pearlite are still exceeded by the applied loads. However, the plastic straining of the base pearlite is reduced to 0.0044 due to the addition of a BEL. The BEL itself shows a small amount of straining compared to the base pearlite (0.0018). It can thus be concluded that the addition of the BEL changes the stress distribution at the surface of the rails and lowers the amount of plastic strain at the interface with the pearlite. This reduction in plastic straining slows the initiation and growth of RCF cracks at the WEL/BEL or BEL/pearlite interfaces. The model thus suggests that spallation of stratified WEL and BEL will be less probable than for a single layer of WEL.

Vampire ©predicts a smaller wheel-rail contact patch size at the PCB than in the SCB. As a consequence, the stresses at the wheel-rail patch in the PCB are expected to be higher than at the SCB for identical applied loads. The forces applied to the FEA model are increased to scale this reduction in wheel-rail contact patch size. As a consequence, the FEA model shows that plastic deformation of the WEL occurs to a larger extent. It is expected that this leads to fragmentation and spallation of the WEL, due to the low toughness of this layer [32, 62]. Fragmentation of the WEL will probably lead to the rapid removal of the WEL from the PCB during repeating wheel loading. Additionally, the high stresses induced by wheel loading and the large number of wheel-rail contacts at the PCB cause wear and plastic deformation of the base pearlite to be larger here than at the SCB. This wear and plastic deformation are expected to aid in the rapid removal of the WEL.

The results of the FEA modelling are in accordance with the formation of cracks observed during optical microscopy experiments. However, it must be noted that the applied forces applied to the model were estimated based on the results of the Vampire ©wheel-rail contact simulation. These forces were also scaled to account for the smaller size of the simulated block of material. Thus, the simulated forces can deviate from the forces experienced by the studied rail. Additionally, most of the material properties of the WEL, BEL and base pearlite were taken or estimated from the literature. The estimations of these parameters can thus give deviations in the quantitate results of the simulation. Nevertheless, the model does give insight into the effects of WEL and BEL on the stress field, plastic deformation and crack formation at the rail surface and subsurface.

Chapter 6: Conclusion

A recently ground rail specimen containing white and brown etching layers and several surface cracks was investigated during this research. A number of conclusions considering their properties and formation process can be drawn:

- WEL contains martensite, retained austenite and partially dissolved cementite. The WEL has formed due to heating above the A_1 temperature during grinding and subsequent quenching. Austenite nucleates at the ferrite/cementite interface and grows until forming a continuous layer. Cementite dissolves due the diffusion of carbon into the austenite. This dissolution is less extensive at greater depths below the rail surface, due to a temperature gradient in the material. Plastic deformation only occasionally assists in the dissolution of cementite due tot the high yield strength of the MHH base material and the limited amount of plastic deformation induced by grinding. Quenching after contact with the grinding stone transforms the austenite to a brittle martensitic layer.
- BEL is a layer beneath the WEL where only partial austenization has occurred, due to lower temperatures and shorter heating at greater depths beneath the rail surface. This results in a layer existing out of martensite, retained austenite and pearlite containing dissolving cementite.
- The small inter lamellar spacing of the MHH steel grade increases the number of austenite nucleation sites and enhances austenite growth by reducing the maximum carbon diffusion length. Additionally, the role of plastic deformation in the dissolution of cementite is limited. However, the chemical composition of MHH increases the A_1 temperature, which reduces the final fraction of austenite after heating to an absolute temperature. Further research will thus be required to determine if the fraction of austenite after heating to an absolute temperature is higher or lower for MHH, when compared to conventional rail steel grades.
- The hardness of the MHH material increases with a factor 2.5 to 2 due to the formation of WEL and BEL respectively. Additionally, grinding induces tensile stresses and a high surface roughness, making the running surface of the rail susceptible to crack formation.
- Heat input during repeating wheel-rail contacts reduces the hardness of the top layer of WEL via tempering and spheroidizes the remnant cementite. Wear induced by wheel-rail contacts removes the high surface roughness and corrosion products. Grinding induced tensile stresses are reduced by repeated wheel-rail contacts due to tempering and wear. Finally, wheel-rail contact causes a peak in plastic strain at the WEL/pearlite interface, due to the difference in yield strength of the two layers. This causes RCF cracks to form at this interface, leading to spallation of the WEL. Stratified layers of WEL and BEL did not show RCF cracks at their interfaces since the BEL reduces the plastic strain of the WEL and base pearlite by accommodating parts of the stresses induced by wheel-rail contact.
- The most severely loaded section of the running surface showed the initial stages of mechanically induced WEL formation in the form of thinning and fragmenting of the cementite lamella of the original pearlite. Additionally, spallation of the WEL and crack initiation via ratcheting occurred during wheel-rail contacts. Developed cracks showed bending and branching due to a changing stress field at increasing distance from the wheel-rail contact point. Oxides were found inside the crack, indicating liquid assisted crack growth.

Several research directions remain to improve the insight into grinding induced transformations in rails and prevent its occurrence during service. Firstly, Electron BackScatter Diffraction (EBSD) and Transmission Electron Microscopy (TEM) measurements could further quantify the fraction of the different phases in the transformed layers [31]. Additionally, the role of dislocations in the formation of WEL and the mechanisms of tempering can be further investigated and quantified using this technique [31]. Secondly, mechanically induced WEL is briefly mentioned in this study, but is not discussed in great depth. Additional research will be required to deepen the understanding of the formation and properties of this type of WEL. Thirdly, larger cracks found at the running surface of the rail specimen had a morphology similar to a squat or heat-check. Further research will be required to understand which factors contributing to the shape and location of these cracks. Fourthly, the grinding process will require optimization to prevent the creation of WEL or BEL. Further research, testing and certification will be required to implement such changes in the railway industry. Finally, developing a Non-Destructive Testing (NDT) detection method for WEL can prove valuable for the railway industry in detecting damage initiation sites at an early stage, thus increasing operational life time of a rail and reducing maintenance costs.

Bibliography

1 Baumann, G., Fecht, H., & Liebelt, S. (1996). Formation of white-etching layers on rail treads. *Wear*, *191*, 133–140.

2 Bevan, A., Jaiswal, J., A., S., & Cabral, M. O. (2018). Judicious selection of available rail steels to reduce life-cycle costs. *Journal of Rail and Rapid Transit*, *0*, 1–19.

3 Bhadeshia, H., & Honeycombe, R. (2017). *Steels: Microstructure and properties* (Elsevier, Ed.).

4 Carroll, R., & Beynon, J. (2007). Rolling contact fatigue of white etching layer: Part 1 crack morphology. *Wear*, *262*, 1253–1266.

5 Castro Cerda, F., Sabiroc, I., Coulas, C., Sietsma, J., Monslave, A., & Petrov, R. (2017). Austenite formation in 0.2% c and 0.45% c steels under conventional and ultrafast heating. *Materials and Design*, *116*, 448–460.

6 Chen, H., Ji, Y., Zhang, C., Liu, W., Chen, H., Yang, Z., … Chen, L. (2017). Understanding cementite dissolution in pearlitic steels subjected to rolling-sliding contact loading: A combined experimental and theoretical study. *Acta Materialia*, *141*, 193–205.

7 Cheng, L., Böttger, A., de Keijser, T., & Mittemeijer, E. (1990). Lattice parameters of iron-carbon and iron-nitrogen martensites and austenites. *Scripta METALLURGiCA et MATERIALIA*, *24*, 509–514.

8 Davis, J. R., Mills, K. M., Lampman, S. R., Zorc, T. B., Lampman, H. F., Crankovic, G. M., … Lynn O'Keefe, K. (1990). *Handbook: Properties and selection: Irons, steels, and high-performance alloys*. Materials Park, Ohio: United States of America: American Society for Metals.

9 Dollevoet, R. (2010). *Design of an anti head check profile based on stress relief.*

10 Doquet, V., & Frelat, J. (2001). Branch crack development from the flank of a fatigue crackpropagating in mode ii. *Fatigue and Fracture Engineering Material Structure*, *24*, 207–214.

11 Ekberg, A., Akesson, B., & Kabo, E. (2014). Wheel/rail rolling contact fatigue – probe, predict, prevent. *Wear*, *314*, 2–12.

12 *Railway applications - track - rail - part 1: Vignole railway rails 46 kg/m and above*. (2011). CEN: European Committe for Standardization.

13 *Equotip portable hardness testers – leeb, rockwell and uci*. (n.d.). Proceq. Retrieved 2019, from https://www.proceq.com/compare/equotip/

14 Fau, F., Secordel, P., & Jaiswal, J. (n.d.). *Tata steel premium grades to address wear and rolling contact fatigue*. Tata Steel Europe, Hayange, France, Tata Steel Europe, Rotherham, UK.

15 Gottstein, G. (2004). *Physical foundations of materials science*. Berlin: Springler Verlag.

16 Grassie, S. (2016). Studs and squats: The evolving story. *Wear*, *366-367*, 194–199.

17 Grassie, S., Fletcher, D., Gallardo Hernandez, E., & Summers, P. (2011). Studs: A squat-type defect in rails. *Proc. IMechE*, *226*, 243–256.

18 Grinding principles: Understanding why, when and how rail grinding is performed. (2015). Retrieved 2019, from https://www.wheel-rail-seminars.com/archives/2015/pc-papers/PC-05%5C%20WRI%5C%202015%5C%20Rail%5C%20Grinding%5C%20Principles%5C%20B-Bell%5C%2020150519v2%5C%20.pdf

19 Hernández silva, D., Morales, R., & Cabañas-Moreno, J. (1992). The spheroidization of cementite in a medium carbon steel by means of subcritical and intercritical annealing. *ISIJ International*, *32*(12), 1297–1305.

20 Homogenious nucleation: Lecture 10 mse 5034. (2004). The Zang Research Group, Department of MSE, University of Utah. Retrieved 2019, from https://my.eng.utah.edu/~lzang/images/lecture-10.pdf

21 Hyzak, J., & Bernstein, I. (1976). The role of microstructure on the strength and toughness of fully pearlitic steels. *METALLURGICAL TRANSACTIONS A*, *7A*, 1217–1225.

22 Ivanisenko, Y., Lojkowski, W., Valiev, R., & Fecht, H.-J. (2003). The mechanism of formation of nanostructure and dissolution of cementite in a pearlitic steel during high pressure torsion. *Acta Materialia*, *51*, 5555–5570.

23 Al-Juboori, A., Wexler, D., Li, H., Zhu, H., Lu, C., Mccusker, A., … Wang, Z. (2017). Squat formation and the occurrence of two distinct classes of white etching layer on the surface of rail steel. *International Journal of Fatigue*, *104*, 52–60.

24 Al-Juboori, A., Zhu, H., Wexler, D., Li, H., McCusker, A., McLeod, J., … Barnes, J. (2019). Evolution of rail surface degradation in the tunnel: The role of water on squat growth under service conditions. *Engineering Fracture Mechanics*, *209*, 32–47.

25 Kalousek, J., Sroba, P., & Hegelund, C. (1989). Analysis of rail grinding tests and implications for corrective and preventative grinding. (pp. 193–204). The fourth international heavy haul railway conference. Brisbane.

26 Kalpakjiak, S. (1995). *Manufacturing engineering and technology* (Third edition).

27 KiM. (2017). *Mobiliteitsbeeld 2017*. Ministirie van Infrastructuur en Milieu.

28 Kim, K.-H., Lee, J.-S., & Lee, D.-L. (2010). Effect of silicon on the spheroidization of cementite in hypereutectoid high carbon chromium bearing steels. *Met. Mater. Int. 16.6*, 871–876.

29 Kim, S. A., & Johnson, W. L. (2007). Elastic constants and internal friction of martensitic steel,ferritic-pearlitic steel, and alpha-iron. *Materials Science and Engineering A*, *452-543*, 633–639.

30 Koshal, D. (1993). *Manufacturing engineer's reference book*.

31 Kumar, A., Agarwal, G., Petrov, R., Goto, S., Sietsma, J., & Herbig, M. (2019). Microstructural evolution of white and brown etching layers in pearlitic rail steels. *Acta Materialia*, *171*, 48–64.

32 kumar, A., Saxena, A., Kirchlechner, C., Herbig, M., Brinckmann, S., Petrov, R., & Sietsma, J. (2019). In situ study on fracture behaviour of white etching layers formed on rails. *Acta materialia*, *180*.

33 Languillaume, J., Kapelski, G., & Baudelet, B. (1996). Cementite dissolution in heavily cold drawn pearlitic steel wires. *Acta materialia*, *45*, 1201–1212.

34 Li, H., Zhang, H., Lv, Z.-f., & Zhu, Z.-f. (2017). Cementite dissolution kinetics of high carbon chromium steel during intercritical austenitization. *J. Phase Equilib. Diffus. 38*, 543–551.

35 Li, P., Li, J., Meng, Q., Hu, W., & Xu, D. (2013). Effect of heating rate on ferrite recrystallization and austenite formation of cold-roll dual phase steel. *Journal of Alloys and Compounds*, *578*, 320–327.

36 Li, Z.-D., Miyamoto, G., Yang, Z.-G., & Furuhara, T. (2011). Kinetics of reverse transformation from pearlite to austenite in an fe-0.6 mass pct c alloy and the effects of alloying elements. *1586—VOLUME 42A, JUNE 2011 METALLURGICAL AND MATERIALS TRANSACTIONS A*, *42A*, 1586–1596.

37 Li, Z., Wen, Z., Su, F., Zhang, R., & Zhou, Z. (2018). Dilatometric research on pearlite-to-austenite transformation of fe–1c–1.44cr low-alloy steel. *J. Mater. Sci. 53*, 1424–1436.

38 Limited, R. G. (2018). Vampire. Retrieved 2019, from http://www.vampire-dynamics.com/

39 Lojkowski, W., Djahanbakhsh, M., Burkle, G., Gierlotka, S., Zielinski, W., & Fecht, H.-J. (2001). Nanostructure formation on the surface of railway tracks. *Materials Science and Engineering*, *A303*, 197–208.

40 Luo, Q. (2016). A new xrd method to quantify plate and lath martensites of hardened medium-carbon steel. *Journal of Materials Engineering and Performance*, *25 (6)*, 2170–2180.

41 Malkin, S., & Guo, C. (2007). Thermal analysis of grinding. *Annals of the CIRP*, *56*, 760–782.

42 Meggiolaro, M., Miranda, A., Castro, J., & Martha, L. (2005). Crack retardation equations for the propagation of branched fatigue cracks. *International Journal of Fatigue*, *27*, 1398–1407.

43 Mills, A. (2014). *Basic heat and mass transfer*. Essex: Pearson Edication Limited.

44 *Miniprof bt rail*. (n.d.). Greenwood Engineering. Retrieved 2019, from https://www.greenwood.dk/miniprofbtrail.php

45 Mittemeijer, E., & Welzel, U. (2013). *Modern diffraction methods*. Wiley VCH.

46 Moser, A., & Pointner, P. (1990). Head-hardened rails produced from rolling heat. *TRANSPORTATION RESEARCH RECORD*, *1341*, 70–74.

47 Naeimi, M., Li, Z., Dollevoet, R., Wu, J., Petrov, R. H., & Sietsma, J. (2015). Computation of the flash-temperature at the wheel-rail contact using a 3d finite element model and its comparison with analytical methods.

48 Nakada, N., Ishibashi, Y., Tsuchiyama, T., & Takaki, S. (2016). Self-stabilization of untransformed austenite by hydrostatic pressure via martensitic transformation. *Acta Materialia*, *110*, 95–102.

49 Nematollahi, G. A., Grabowski, B., Raabe, D., & Neugebauer, J. (2016). Multiscale description of carbon-supersaturated ferrite in severely drawn pearlitic wires. *Acta materialia*, *111*, 321–334.

50 Newcomb, S., & Stobbs, W. (1984). A transmission electron microscopy study of the white-etching layer on a rail head. *Materials Science and Engineering*, *66*, 195–204.

51 NOS. (2019). Van veldhoven: In 2040 elke 10 minuten een trein tussen negen steden. Retrieved 2019, from https://nos.nl/artikel/2270726-van-veldhoven-in-2040-elke-10-minuten-een-trein-tussen-negen-steden.html

52 Offerman, S., van Wilderen, L., van Dijk, N., Sietsma, J., Rekveldt, M. T., & van der Zwaag, S. (2003). In-situ study of pearlite nucleation and growth during isothermal austenite decomposition in nearly eutectoid steel. *Acta Materalia*, *51*, 3927–3938.

53 Österle, W., Rooch, H., Pyzalla, A., & Wang, L. (2001). Investigation of white etching layers on rails by optical microscopy, electron microscopy, x-ray and synchrotron x-ray diffraction. *Materials Science and Engineering*, *A303*, 150–157.

54 Pan, R., Ren, R., Chen, C., & Zhao, X. (2017). The microstructure analysis of white etching layer on treads of rails. *Engineering Failure Analysis*, *82*, 39–46.

55 Popović, Z., Lazarević, L., Brajović, L., & Vilotijecić, M. (2015). The importance of rail inspections in the urban area -aspect of head checking rail defects. *Procedia Engineering*, *117*, 596–608.

56 Porter, D., Easterling, K., & Sherif, M. (2009). *Phase transformations in metals and alloys* (Third Edition). Boca Raton: CRC Press, Taylor and Francis Group.

57 ProRail. (2018). *Richtlijn mechanische oppervlaktebewerkingen spoorstaven*. Version 001.

58 Rasmussen, C. J., Faester, S., Dhar, S., Quaade, J. V., Bini, M., & Danielsen, H. K. (2017). Surface crack formation on rails at grinding induced martensite white etching layers. *Wear*, *384-385*, 8–14.

59 Sahay, S., Mohapatra, G., & Totten, G. (2009). Overview of pearlitic rail steel: Accelerated cooling, quenching, microstructure, and mechanical properties. *Journal of ASTM International*, *6*, 1–26.

60 Samuels, L. (2014). Tempering of martensite. *Metalogr. Microstruct. Anal. 3*, 70–90.

61 Sauvage, X., Copreaux, J., Danoix, F., & Blavette, D. (2000). Atomic-scale observation and modelling of cementite dissolution in heavily deformed pearlitic steels. *Philosophical Magazine A*, *80*, 781–796.

62 Saxena, A., Kumar, A., Herbig, M., Brinckmann, S., Dehm, G., & Kirchlechner, C. (2019). Micro fracture investigations of white etching layers. *Materials and Design*, *180*, 1–9.

63 Schotsman, B. (2017). *Spalling defects in mhh steel rails* (Hogeschool Utrecht).

64 Seo, E., Cho, L., & De Cooman, B. (2014). Application of quenching and partitioning (q and p) processing to press hardening steel. *The Minerals, Metals and Materials Society and ASM International*, *45A*, 4022–4038.

65 Slot, H. (2016). *Tno 2016 r11117: Rail grinding- more stringent requirements for the ground surfaces*. TNO.

66 Srivastava, J. P., Sarkar, P. K., & Ranjan, V. (2014). Contact stress analysis in wheel–rail by hertzian method and finite element method. *J. Inst. India. Ser. C*, *95 (4)*, 319–325.

67 Steenbergen, M. (2016). Rolling contact fatigue in relation to rail grinding. *Wear*, *356-357*, 110–121.

68 Steenbergen, M. (2015). Squat formation and rolling contact fatigue in curved rail track. *Engineering Fracture Mechanics*, *143*, 80–96.

69 Steenbergen, M., & Dollevoet, R. (2013). On the mechanism of squat formation on train rails – part i: Origination. *International Journal of Fatigue*, *47*, 361–372.

70 Steenbergen, M., & Messaadi, M. (2018). Stratified surface layers on rails. *Wear*, *414-415*, 151–162.

71 *Surftest sj-210- series 178-portable surface roughness tester*. (n.d.). Mitutoyo. Retrieved 2019, from https://ecatalog.mitutoyo.com/Surftest-SJ-210-Series-178-Portable-Surface-Roughness-Tester-C1794.aspx

72 Takahashi, J., Kosaka, M., Kawakami, K., & Tarui, T. (2012). Change in carbon state by low-temperature ageing in heavily drawn pearlitic steel wires. *Acta Materialia*, *60*, 387–395.

73 Takahaski, J., Kawakami, K., & Ueda, M. (2010). Atom probe tomography analysis of the white etching layer in a rail track surface. *Acta materialia*, *58*, 3602–3612.

74 Thyssen Stahl, A. (1989). *Oberbaumaterial.*

75 *D4.1.5gl: Definitive guidelines on the use of different rail grades*. (2009). INNOTRACK.

76 Toribio, J., González, B., Matos, J.-C., & Ayaso, F.-J. (2016). Influence of microstructure on strength and ductility in fully pearlitic steels. *Metals*, *6*(318).

77 Treinreiziger.nl. (2018). Meer treinreizigers in 2017. vooral rond amsterdam. Retrieved 2019, from https://www.treinreiziger.nl/meer-treinreizigers-2017-vooral-rond-amsterdam/

78 van der Voor, G., & Roosz, A. (1984). Measurement of the interlamellar spacing of pearlite. *Metallography*, *17*, 1–17.

79 Varshney, A., Verma, D., & Sangal, S. (2015). High strength high carbon low alloy pearlite-ferrite-tempered martensite steels. *Trans Indian Inst Met*, *68(1).*

80 Wickens, A. (1998). The dynamics of railway vehicles-from stephenson to carter. *Proceedings of the Institution of Mechanical Engineers, Part F: Journal of Rail and Rapid Transit*, *212*, 209–217.

81 Wikipedia. (2019). Electrical discharge machining. Retrieved 2019, from https://en.wikipedia.org/wiki/Electrical_discharge_machining

82 Wild, E., Wang, L., Hasse, B., Wroblewski, G., T. ad Goerigk, & Pyzalla, A. (2003). Microstructure alterations at the surface of a heavily corrugated rail with strong ripple formation. *Wear*, *254*, 876–883.

83 Wu, J. (2018). *Microstructure evolution in pearlitic rail steel due to rail/wheel interaction*. Tu Delft.

84 Zerbst, U., Lundén, R., Edel, K., & Smith, R. (2009). Introduction to the damage tolerance behaviour of railway rails – a review. *Engineering Fracture Mechanics*, *76*, 2563–2601.

85 Zhang, H., Ohsaki, S., Mitao, S., Ohnuma, M., & Hono, K. (2006). Microstructural investigation of white etching layer on pearlite steel rail. *Materials Science and Engineering*, *A421*, 191–199.

86 Zhang, Z., Shang, W., Ding, H., Guo, J., Wang, H., Liu, Q., & Wang, W. (2016). Thermal model and temperature field in rail grinding process based on a moving heat source. *Applied Thermal Engineering*, *106*, 855–864.

87 Zhao, X., & Li, Z. (2011). The solution of frictional wheel–rail rolling contact with a 3d transient finite element model: Validation and error analysis. *Wear*, *271*, 444–452.

88 Zhao, X., Guo, J., Wang, H., Wen, Z., Lui, Q., Zhao, G., & Wang, W. (2016). Effects of decarburization on the wear resistance and damage mechanisms of rail steels subject to contact fatigue. *Wear*, *364-365*, 130–143.

89 Zhou, Y., Peng, J., Luo, Z., Cao, B., Jin, X., & Zhu, M. (2016). Phase and microstructural evolution in white etching layer of a pearlitic steel during rolling–sliding friction. *Wear*, *362-363*, 8–17.

Appendix A1: Description of the computer simulations

A1.1 Vampire wheel-rail contact simulation

Vampire ©software simulates rail vehicle behaviour for specified track and vehicle geometries [38] via a multi-body dynamics model. For this study, emphasis was placed on the wheel-rail interaction. Two types of simulation were done.

Firstly, the lateral wheel-rail contact position was plotted as a function of the lateral displacement of the train. The measured rail profile, shown in figure A1.1 was used for the upper leg of the curve. A nominal 54E 5 profile was used for the lower leg. The unworn S1002-E30p5 wheel profile of a VIRM II-mBvk car was taken. Wear of the wheel profile was not taken into account, since re-profiling of the wheel occurs every ten weeks. The result of this simulation was shown in figure 4.3.

Vampire ©shows that contact between the wheel and the rail will occur at the primary contact band instead of the top of the rail, due to the inertia and of the train in the curve. The contact poit will occasionally shift to the secondary or tertiary contact band, due to a spread in the up-hill speed of the trains on this section of track [63, p. 30] or a lateral ossilation motion of the train. At the SCB, the wheel-rail contact patch will have a larger size than in the PCB, while contact in the TCB will mainly occur at the grinding facet edges. Flange contact only occurs at large outwards displacements of the train. The gauge corner only experiences contact at the edges of its grinding facets.

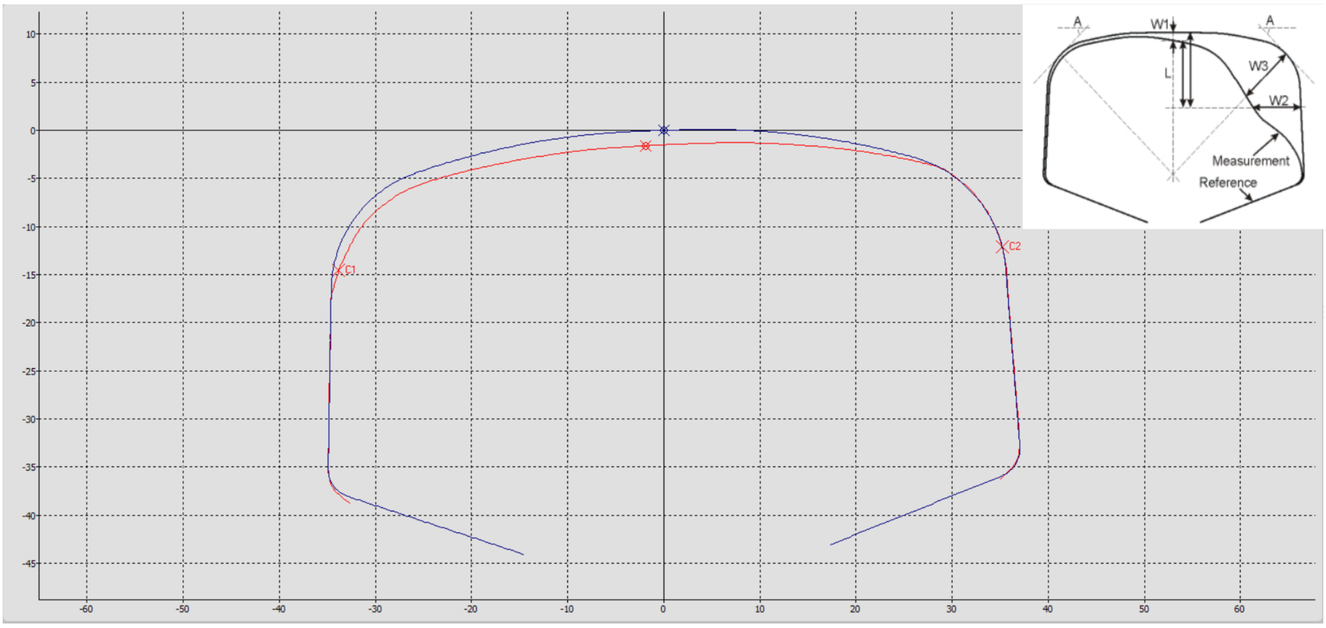

Figure A1.1: *The profile measurement of the rail specimen is shown in red. The blue line shows the original rail profile. Resolution of the measurement is +/- 2.5 µm.*

In the second simulation, a model of the track at Blauwkapel was build. Figure A1.2 schematically shows design of this track and the approximate location of the extracted rail specimen. A VIRM II-mBvk car was simulated to run over this track at 140 km/h. The friction coefficient between the wheel and rail was taken as 0.3. The interaction forces and creep were calculated as a function of the travelled distance at each of the four wheels at the upper leg of the curve. Additionally, the size, shape and location of the wheel rail contact point were calculated.

The results of the Vampire ©simulation showed that longitudinal traction forces were mainly exerted by the front wheels on each bogie, since they had traction motors applied to them. Traction forces increased in the curve and peaked at the transition form the curve to a straight section, at the location of the rail specimen. Lateral forces were largest in the curve and were exerted by the rear wheels on each bogie, since only these wheels made flange contact. Finally, the weight of the train, which was initially equally distributed on both wheels on each bogie, moved to the rear wheels on each bogie. Creepage of the wheels increased when entering the curve and remained constant until existing the curve again. The total creepage, which is calculated from the longitudinal an transverse creepage via Pythagoras theorem, was largest at the rear wheel of each bogie, at a value of 0.628%.

The following selected values of the simulated parameters would maximize loading of the rail during wheel-rail contact:

- Maximum traction force: $T_{max} = 25.65kN$
- Maximum lateral force: $Y_{max} = 8.72kN$
- Maximum vertical force: $Z_{max} = -109.4kN$
- Maximum total creepage: $\zeta = 0.628\%$
- Average lateral wheel position point: at the primary contact band, 736.0 mm form the rail centre.
- Minimum wheel contact patch area: $A = 91.91mm^2$
- Ellipticity of the wheel contact patch (length/width): 2.656

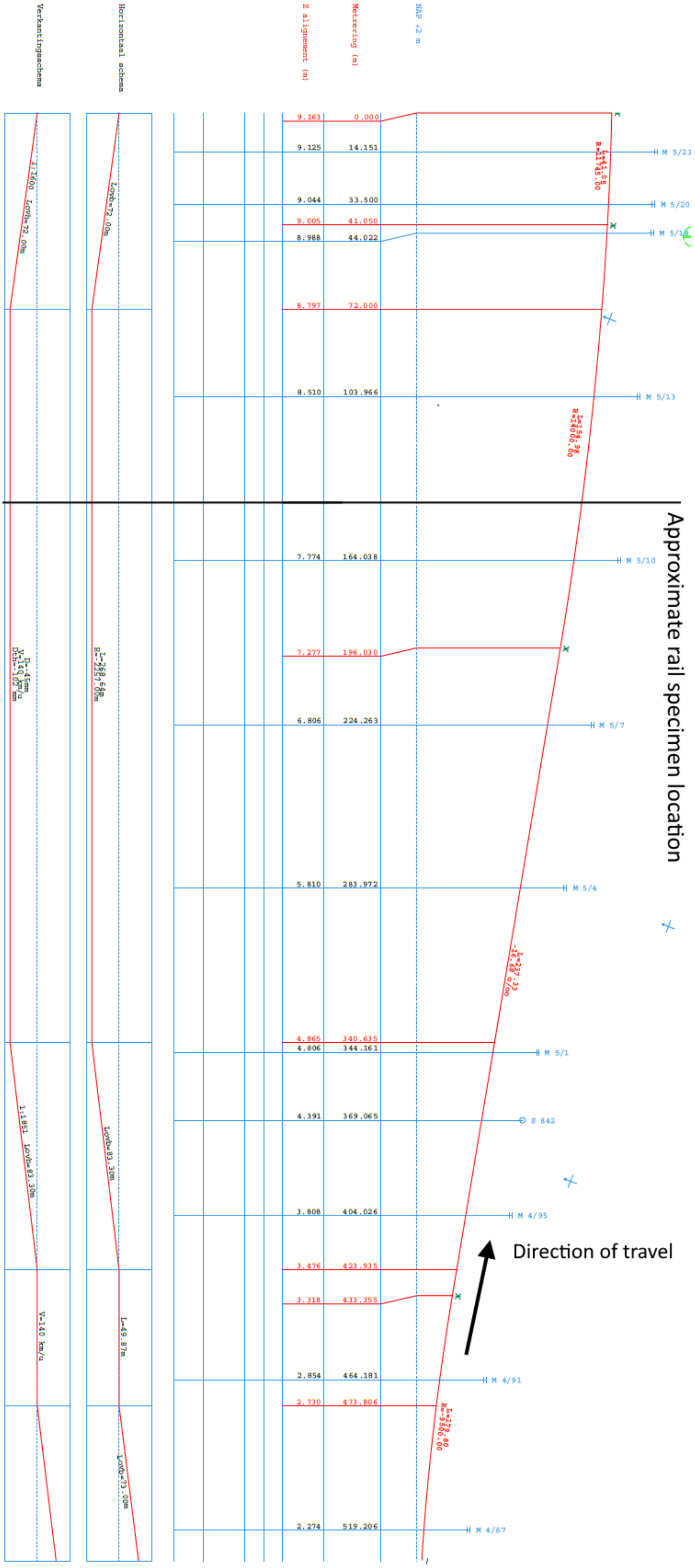

Figure A1.2: *A schematic drawing of the track design at Blauwkapel. The approximate location of the extracted rail specimen is marked in the figure.*

A1.2 Matlab model: Temperature profile during grinding

A model was build in Matlab ©to estimate the temperature field during grinding, based on the surface quality of the rail specimen. This section of the text aim to describe this model in detail. Figure A1.3 gives a schematic representation of the modelled grinding process.

A1.2.1 List of constants

Several variables were used in this simulation. These were assumed to remain constant during the entire grinding operation.
Measurements taken from the rail surface:

- $b = 6 * 10^{-3}$, the narrowest facet width in m.
- $R_a = 7.1 * 10^{-6}$, a roughness value in m, chosen in the range of measurements from the ground band.

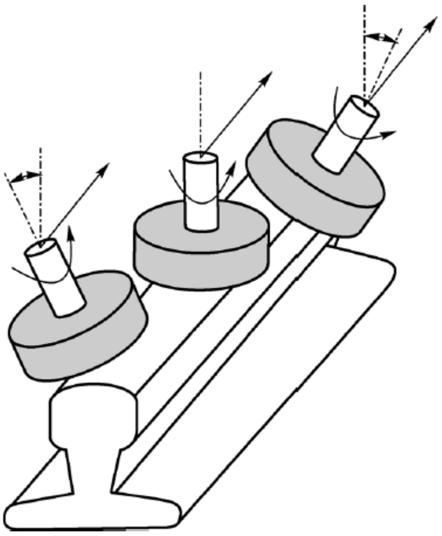

Figure A1.3: *A schematic representation of the grinding process.*

Material properties:

- $\lambda = 46$, the heat conduction coefficient of steel in W/mK [57, p. 27].
- $\varepsilon = 0.55$, the energy participation constant [-] [57, p. 27].
- $\alpha = 1.33 * 10^{-5}$, diffusivity of steel in m^2/s [57, p. 27].

Grinding process parameters:

- $d_e = 0.260$, grinding stone diameter in m [65, p. 59].
- $v_w = 3.333$, forward speed of the grinding train in m/s [63, p. 32].
- $n = 3600$, rotational speed of the grinding stone rpm [65, p. 59].
- $v_s = \pi * n * d_e = 75.4$, calculated tangential speed of the grinding stone m/s [65, p. 59].
- $d_{gs} = 0.25$, estimated distance between two successive grinding stones m.
- $C = 0.45 * 10^6$, number of contact points for mesh 16 grinding stone m^{-2} [65, p. 59].
- $r = 15$, width/thickness ratio of grinding chip [-] [65, p. 59].
- $c_{vw} = 13.99 * 10^9$, specific grinding energy in j/m [57, p. 27].
- $T_0 = 25$, the ambient temperature in $^\circ C$.

A1.2.2 Equations for describing the grinding process

Malkin and Guo [41], Koshal [30], Kalpakjian [26] and Kalousek et al. [25] defined a number of equations to describe the grinding process. The cutting depth of a single grinding stone m can be calculated via:

$$a_e \leq d_e * \left(\frac{4R_a^2 * v_s * Cr}{v_w} \right)^2 \tag{A1.1}$$

This value can subsequently be used to calculate the power direct into the grinding stone in W:

$$P = ae * b * cvw * vw^{0.672} \tag{A1.2}$$

Finally, the flash temperature at the grinding stone surface in $^\circ C$ is given as:

$$T_{surf} = T0 + \frac{(1.13 * epsilon * \sqrt{\alpha} * (\frac{P}{b})^{3/4} * (\frac{d_e}{c_{vw}})^{-1/4} * v_w^{-0.33225})}{\lambda} \tag{A1.3}$$

A1.2.3 Heat conduction under the surface

The flash temperature at the grinding stone surface calculated in equation A1.3 is imposed on the rail surface and causes a heat flux into the material. This heat flux is calculated in W/m^2 as:

$$q_g = \frac{\lambda * (T_{surf} - T_0)}{\sqrt{\pi * \alpha * t_g}} \tag{A1.4}$$

Here, t_g is the time that contact exists between a fixed point on the rail surface and the passing grinding stone. This value can be calculated in s via:

$$t_g = \frac{d_e}{v_w} \tag{A1.5}$$

Subsequently, the temperature during grinding in $°C$ is calculated as a function of distance below the rail surface and time [43, p. 169]. This distribution is approached as a one dimensional semi-infinite heat conduction problem. The effects of convection and radiation are neglected. It is further assumed that no internal heat is generated in the material.

$$T_g(z,t) = T_0 + \frac{q_g}{\lambda} * [(\frac{4*\alpha*t}{\pi})^{1/2} * \exp(\frac{-z^2}{4*\alpha*t}) - z * erfc(\frac{z}{(4*\alpha*t)^{1/2}})] \tag{A1.6}$$

Here z is the depth below the surface in m. After passing of the grinding stone, cooling of the material at the rail surface via conduction of heat into the remaining rail material is simulated. The heat flux during cooling is estimated by:

$$q_c = \frac{\lambda * (T_{surf} - T(z=0, t=t_g))}{\sqrt{\pi * \alpha * t_c}} \tag{A1.7}$$

Here, t_c is the time until a subsequent grinding stone passes over the fixed point. For this simulation, a worst case scenario has been chosen in which subsequent grinding stones pass over the same facet [86]. The simulation ends when t_c has expired after passing of the last simulated grinding stone. The value of t_c is given as:

$$t_c = \frac{d_{gs}}{v_w} \tag{A1.8}$$

The temperature field during cooling is calculated by reusing equation A1.6:

$$T_c(z,t) = T_g(z, t=t_g) + \frac{q_c}{\lambda} * [(\frac{4*\alpha*t}{\pi})^{1/2} * \exp(\frac{-z^2}{4*\alpha*t}) - z * erfc(\frac{z}{(4*\alpha*t)^{1/2}})] \tag{A1.9}$$

A layer of material is removed with passing of each subsequent grinding stone. The model accounts for this by making a jump in the temperature field from $z = 0$ to $z = a_e$ before contact with a new grinding stone occurs. Thus, The temperature at a depth of a_e is set as the new surface temperature. All the temperature values of the material above $z = a_e$ are discarded.

The heat input during subsequent grinding stone passage is calculated by replacing T_0 in equation A1.4 with $T_c(z = 0, t = t_g + tc)$. The simulation is then repeated from A1.6 onwards for each subsequent grinding stone.

A1.2.4 Brief summary of results

Using the measured values for the surface roughness and width of a grinding facet, a temperature field as shown in figure A1.4 is obtained. The power input for grinding is calculated to be 19.6 kW per stone, which is still below the maximum power input of 22 kW [65, p. 62]. The cutting depth per grinding stone was calculated to be 0.1 mm and the flash temperature at the grinding stone surface was 1250 $°C$. This temperature is imposed on the rail surface and causes a temperature increase in the rail material. The A_1 and A_{cm} temperatures, as calculated by Thermo-Calc ©, were surpassed at a depth of 160 μm and 1 μm respectively during passage of the first grinding stone.

The model additionally suggests that heat input during grinding can be reduced in several manners. Firstly, reducing the power output of the grinding stone motors will reduce the rotational speed of the stones and thus the frictional heat generated. However, the surface roughness after grinding will increase when reducing the rotational speed, possibly exceeding geometrical tolerances [65, p. 64]. Secondly, an increase in grinding train velocity and

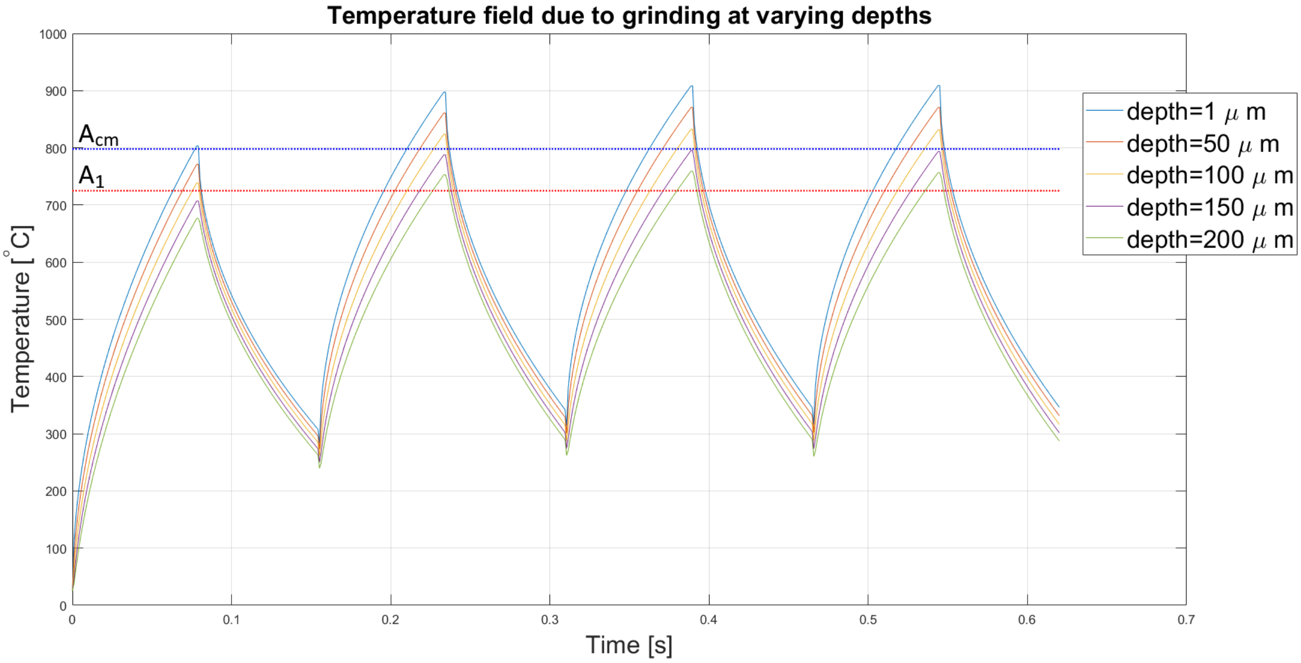

Figure A1.4: *The temperature field created by four successive grinding stones passing on the same facet. Calculations were done as a function of depth below the surface and time.*

smaller grinding stone diameter will reduce the contact time during grinding stone passage, reducing the available time for heating. Thirdly, a finer grinding stone mesh will reduce frictional heating during grinding. All of the before mentioned measures have the disadvantage of reducing the cutting depth during grinding, thus increasing the duration of cyclic grinding maintenance and the costs of this maintenance. Finally, it should be avoided to apply subsequent grinding stones on the same or adjacent grinding facets. This prevents reheating of the material before cooling is completed, which leads to a higher peak temperature during contact with the subsequent grinding stone [86]. Implementation of these suggestions will require further research, design and certification of the grinding process.

A1.3 Finite Element Analysis of stress distribution in stratified layers

Figure 4.6c shows crack growth along the interface of the WEL and base pearlite, suggesting that a stress concentration exists at this interface. Stratified layers of WEL and BEL did not show this behaviour. A Finite Element Analysis (FEA) in Comsol Multiphysics 5.4 ©software was done to explain this behaviour. Two 2000 μm*500 μm*235 μm blocks were constructed. The first of these blocks contained a WEL with a thickness of 35 μm at its top surface. The underlying 200 μm consisted out of pearlite. The second block was comprised out of a 35 μm layer of WEL with 20 μm of BEL and 180 μm of base pearlite underneath. The selected material properties for each of the layers are presented in the list below. In this list, η is the linear hardening exponent.

Material properties base pearlite (MHH steel grade):

- E=200 GPa [76].
- σ_y=830 MPa [14].
- η= 2.5 MPa, taken from [76].
- σ_{uts}=1280 MPa [12, 14, p. 21].
- ν=0.29 [29].

Material properties of the WEL, simulated as martensite in rail steel:

- E=210 GPa [29].

- σ_y=1500 MPa [79].
- η= 6 MPa, taken from [79].
- σ_{uts}=1700 MPa, taken from [79].
- ν=0.29 [29].

Material properties BEL, simulated as a mixture of 50% base pearlite and 50% martensite:

SE imaging showed that BEL is a mixture of martensite, retained austenite and dissolving pearlite. Thus BEL was simulated to be a mixture of 50% WEL and 50% base pearlite. The material properties of the BEL were calculated by applying the lever rule to the material properties of the WEL and base pearlite, resulting in the following list of material properties:

- E=205 GPa.
- σ_y=1165 MPa.
- η= 4.25 MPa.
- σ_{uts}=1440 MPa.
- ν=0.29.

The results of the Vampire ©wheel rail contact simulation could not be used to determine the forces exerted on the block of material, since the blocks of this simulation are located at the SCB, while vampire ©calculates the forces at the PCB. Vampire ©predicts a larger wheel-rail contact patch at the SCB than at the PCB, thus resulting in lower contact stresses at the SCB. The forces to apply to the finite element model at the SCB were thus estimated, based on the results of the Vampire ©contact model. The top area of the block was taken smaller than the original wheel-rail contact patch size. Thus, scaling of the wheel-rail contact forces by the area of the block and the area of the wheel-rail contact patch resulted in the forces to be applied to the finite element model. Finally, the following forces were applied to the model:

- Scaled traction force: 94.9 N.
- Scaled transverse force: 7.53 N.
- Scaled weight of the train: -920 N.

These force were applied to the top surfaces of each block. Additionally, both blocks were constrained at their both side. The isotropic linear elastic behaviour and the isotropic linear hardening behaviour in the plastic regime were modelled. The mesh size setting in Comsol ©was set to ”Finer”.

A1.3.1 Brief summary of results

Figure A1.5a shows the von Mises stress distribution at a cross-section in the block of WEL and base pearlite. The yield strengths of both the WEL and base pearlite are surpassed at the applied loads. A stress concentration is seen at the WEL, since this layer can take up a larger amount of stress before yielding than the base pearlite. Figure A1.5b shows the von Mises stress distribution in the stratified layer of WEL and BEL. The stress intensity at the WEL has reduced to below the yield strength due to the addition of a BEL. Table 4.1 shows that stratified layers of WEL and BEL have a larger thickness than single WEL. Thus, the BEL ads a layer of material with a higher yield strength than the base pearlite. The BEL thus accommodates some of the stresses that were previously accommodated in the WEL and base pearlite.The yield strength of the base pearlite and the BEL are both surpassed at the applied load levels. Thus, the stresses accommodated by the WEL, BEL and base pearlite reduce step-wise when moving away form the rail surface.

Figure A1.6a shows the plastic strain in the block containing the WEL and base pearlite as a function of depth below the surface. It is seen that only a limited amount of plastic straining occurs in the WEL itself. At the interface with the base pearlite, the plastic strain suddenly increases since the yield stress of the base pearlite is surpassed. This strain decreases with increasing depth since the stresses create by wheel-rail contact also decrease here. Figure A1.6b shows that the addition of a BEL prevents plastic straining in the WEL. Additionally, the amount of plastic strain in the base pearlite is significantly reduced, when compared to figure A1.6a. The BEL itself shows a small amount of plastic straining when compared to the base pearlite.

It can thus be concluded that the highest stresses occur at the rail surface and decrease at increasing depth beneath the rail surface. These stresses will only cause a limited amount of plastic deformation of the WEL. However, a peak in plastic straining occurs at the WEL/pearlite interface due to the lower yield strength of the base pearlite. A crack will form at this interface due to ratcheting during repeating wheel-rail contacts. The location of this crack is in accordance with the cracking seen in figure 4.6c and d. Inserting a BEL between the WEL and the base pearlite reduces the stresses in both the WEL and the base pearlite, since BEL is simulated as a mixture of WEL and pearlite and thus has a higher yield strength than the base pearlite. As a consequence, the stress concentrations at the WEL and WEL/pearlite interface are lowered, thus reducing yielding of the WEL and pearlite. The lower amount of plastic straining reduces the initiation and growth during wheel-rail loadings.

Stresses at the PCB are expected to be higher than in the SCB. Vampire ©predicted a smaller wheel-rail contact patch size exists in the PCB than in the SCB. Thus identical forces applied by the wheel on the rail will induce a higher stress in the PCB than in the SCB. To simulate this, the forces predicted by Vampire ©in section A1.1 were applied to the FEA model. The forces were scaled by the size of the wheel-rail contact patch given by Vampire ©and the surface area of the simulated block of material. The FEA model shows that plastic deformation of the WEL increases due to the larger stresses. It is expected that this leads to fragmentation and spallation of the WEL, due to the low toughness of this layer [32, 62]. Fragmentation of the WEL will probably lead to the rapid removal of the WEL from the PCB during repeating wheel-rail contacts.

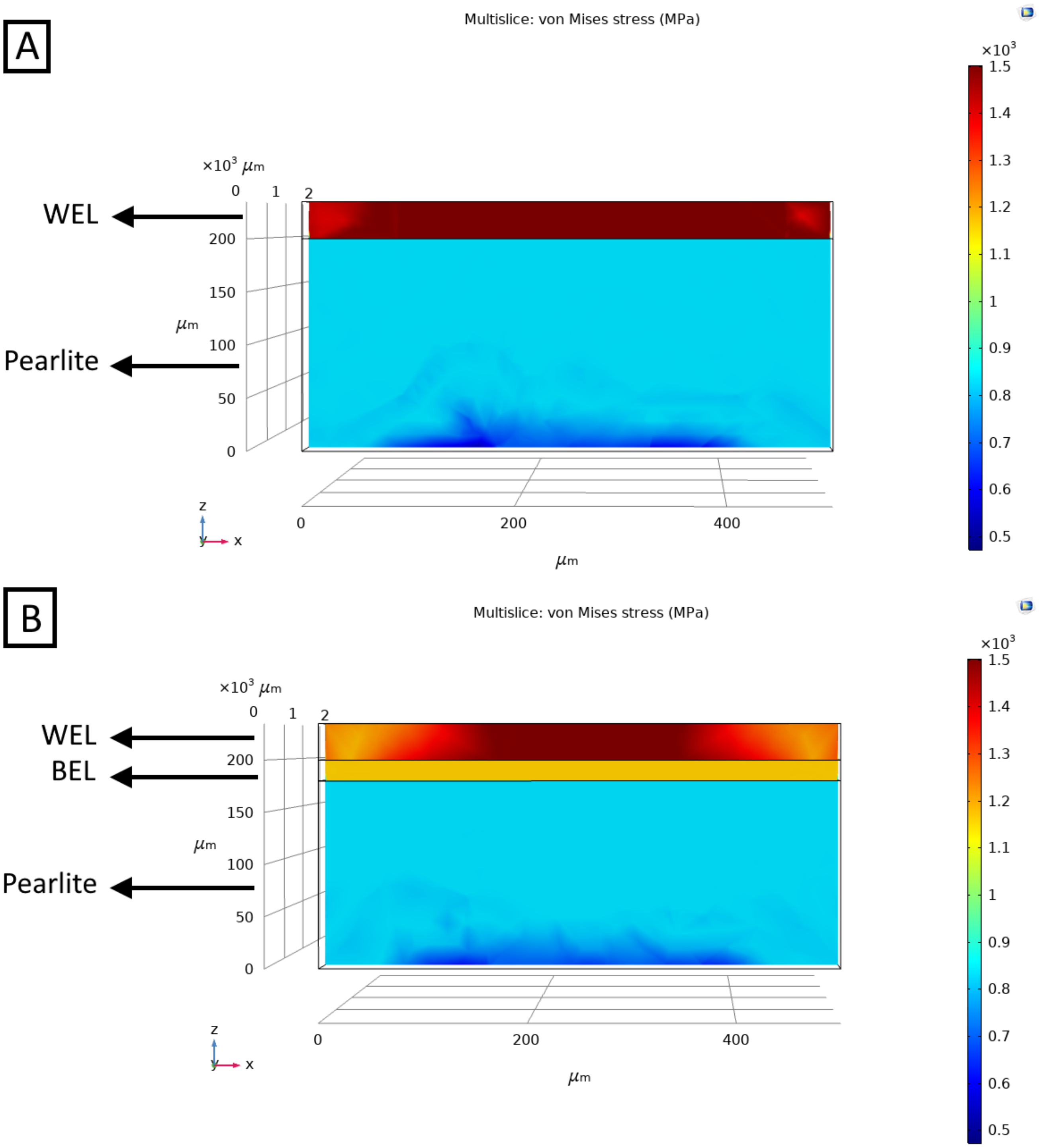

Figure A1.5: *The von Mises stress distribution in a layer of WEL and base pearlite (a) and stratified layers of WEL, BEL and base pearlite (b).*

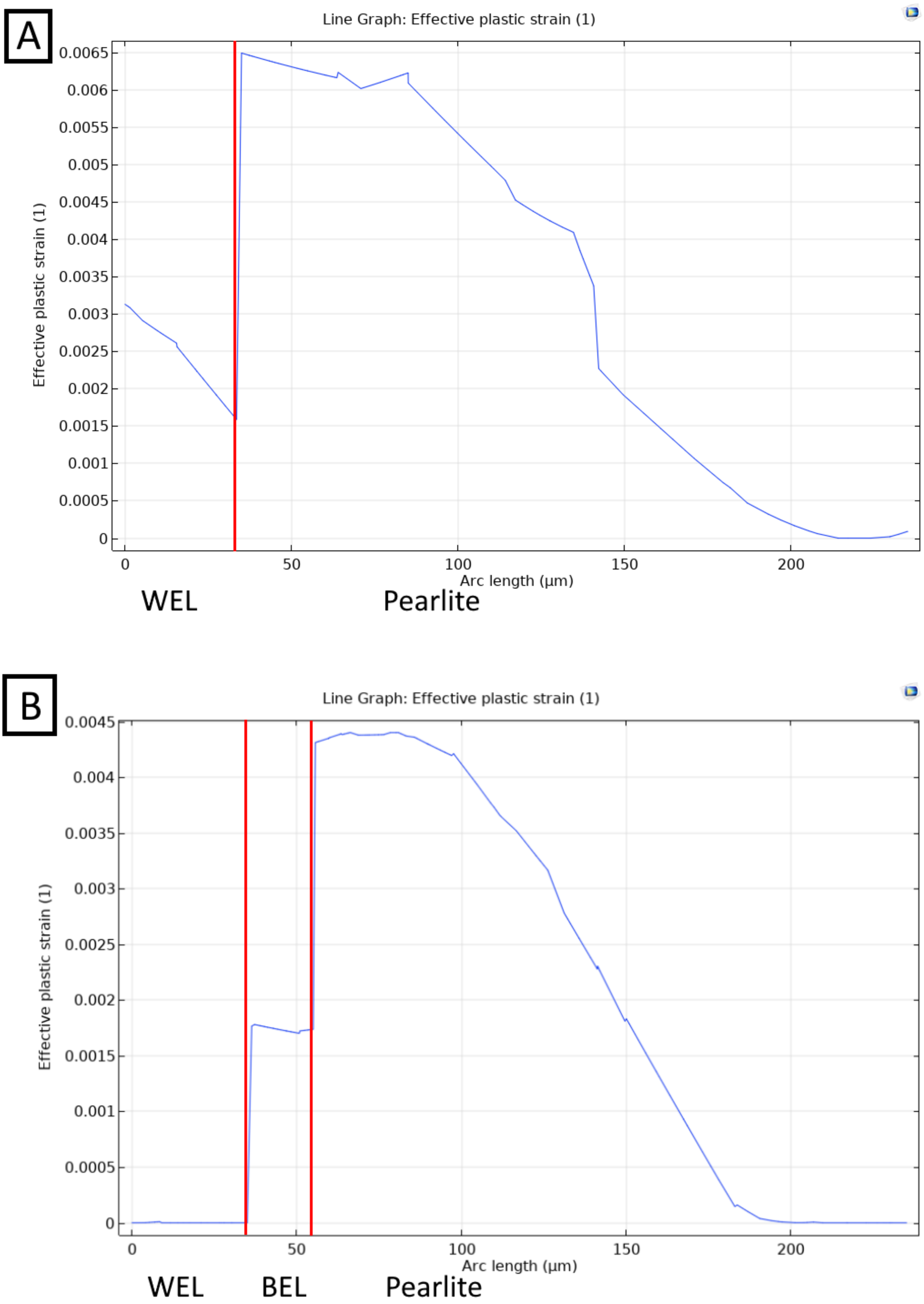

Figure A1.6: *The plastic strain in a layer of WEL and base pearlite (a) and stratified layers of WEL, BEL and base pearlite (b).*

Appendix B2: Analysis of the XRD measurements

B2.1 Determining the carbon content of austenite

B2.1.1 Determining the lattice parameter of austenite

Phase analysis on a patch of WEL in the tertiary contact band was done using a Bruker D8 Advance diffractometer with Bragg-Brentano geometry. A graphite monochromator and Vantec position sensitive detector were used during this analysis. Co Kα radiation was created at 45 kV and 35 mA. The 2θ step size was set at 0.035° and measurements were done every 4 seconds.

Fitting with Pearson VII was used to determine the austenite peak positions from the XRD spectrum shown in figure B2.1. Determination of the $\{111\}$ austenite peak position was difficult, since it overlapped with the a and c peaks of martensite and the wüstenite peak, as shown in the magnification of figure B2.1. Figure B2.2 Shows the fitting of each of the austenite peaks, resulting in the peak positions and Nelson-Riley plot shown in figure B2.3.

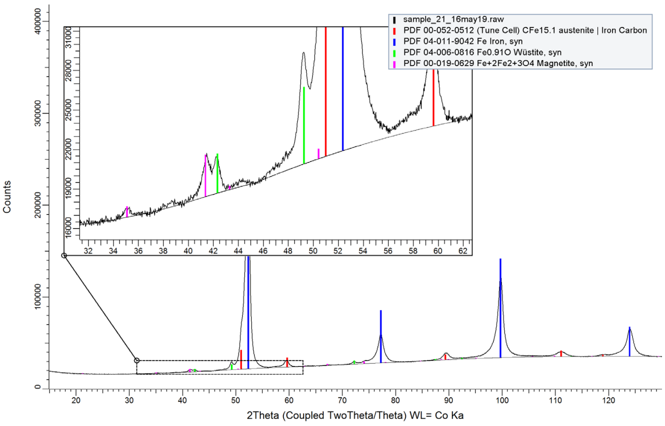

Figure B2.1: *The XRD-spectrum showing the phases present within the WEL at the rail surface at the TCB.*

The lattice parameter was determined to be 3.598 ± 0.004 Å. The large scatter in the Nelson-Riley plot indicates that the found lattice parameter is not the stress-free lattice parameter. A residual stress due to the phase transformation form austenite to martensite is present in the material [7], reducing the lattice parameter of austenite.

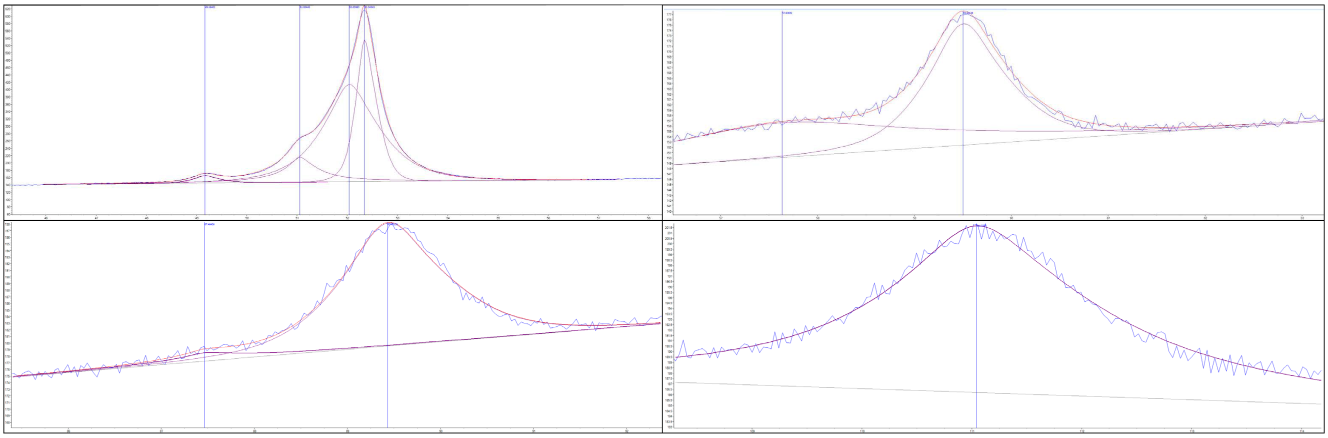

Figure B2.2: *Determination of the peak position of the four austenite peaks using Pearson VII fitting.*

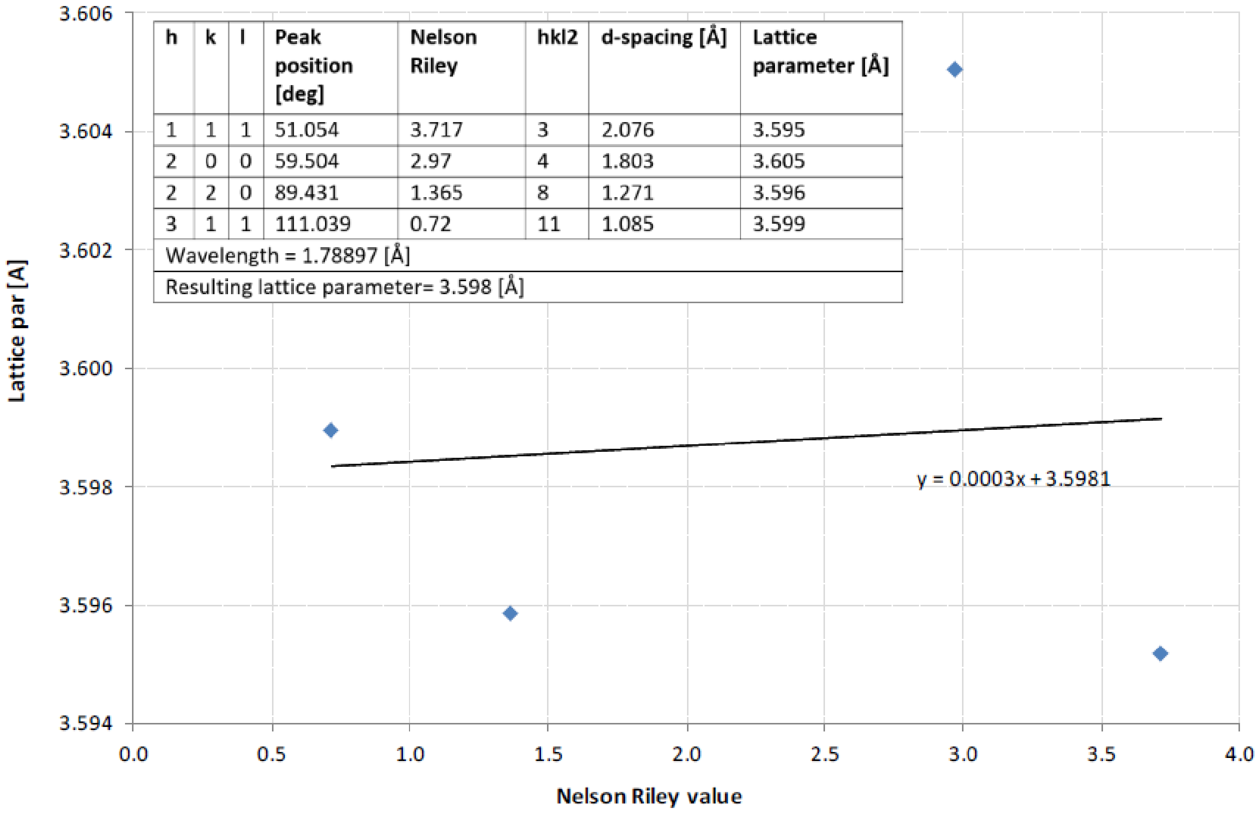

h	k	l	Peak position [deg]	Nelson Riley	hkl2	d-spacing [Å]	Lattice parameter [Å]
1	1	1	51.054	3.717	3	2.076	3.595
2	0	0	59.504	2.97	4	1.803	3.605
2	2	0	89.431	1.365	8	1.271	3.596
3	1	1	111.039	0.72	11	1.085	3.599
Wavelength = 1.78897 [Å]							
Resulting lattice parameter= 3.598 [Å]							

Figure B2.3: *The Nelson-Riley plot, used to determine the austenite lattice parameter. The large spread in the data shows that the lattice parameter is influenced by residual stresses in the material.*

B2.1.2 Determining the carbon content of austenite

A formula for the dependence of austenite lattice parameter on the carbon content is given by Cheng et al. [7]. This formula considers the compressive stresses exerted on the retained austenite due to the 4% volume increase of the transformed martensite [7]. The effect of manganese and chromium alloying elements were given by Seo et al. [64]. The effect of silicon was found to to be negligible. The following formula was derived by combining these sources:

$$a_\gamma = 0.3556 + 0.0045X_C + 0.00006 * X_{Cr} + 0.00095 * X_{Mn} \tag{B2.1}$$

Here, a_γ is the measured lattice parameter of austenite and X_C, X_{Cr} and X_{Mn} are the content of the respective alloying elements in wt.%. When assuming that the manganese and chromium content have a constant value as specified in table 3.1, the dependence of the austenite lattice parameter on the carbon content becomes:

$$a_\gamma = 0.3565 + 0.0045X_C \tag{B2.2}$$

By using this method, the carbon content in the austenite is determined to be 0.90 ± 0.10 wt.%.

B2.2 Determination of the stresses at the rail surfaces

Stresses at the rail surface were measured using the $sin^2(\psi)$ method [45]. A Bruker D8 Discover with an Eulerian cradle and parallel beam geometry was used for these measurements. Co Kα radiation was created at 45 kV and 25 mA. A square area with sides of 2 mm was exposed to this radiation. Specimen preparation and determination of the shift in peak position was done differently for each measured sample and will thus be discussed here.

The specimen for the MHH base material was taken from the field side of the rail head, as shown in figure 3.2b. It was assumed that effects of hot rolling and heat treatment would be similar at the field side and at the actual running surface. Specimen preparation was done by grinding with 80, 180, 320, 800, 1200 and 2000 grid paper and polishing with 3 and 1 μm diamond polish, in order to remove the heavy corrosion present on this surface. After measurements, the $\{100\}$ 2θ peak was fitted with Peason VII to determine the peak locations. Figure B2.4a shows the resulting shift in peak position.

The specimen containing the ground and wheel loaded surfaces only required mild grinding with 2000 grid paper. After measuring, the peak locations of the $\{100\}$ 2θ peak in the ground surface was determined by finding the centre of gravity. The resulted in the peak shift shown in figure B2.4b. The location of the $\{100\}$ 2θ peak in the wheel loaded section of the surface (SCB) required Pearson VII fitting of the a and c peaks of the martensitic lattice, as shown in figure B2.4c. Finally, the stresses in the longitudinal direction of the rail were calculated with a $1/2S^2$ value of 5.76 1/TPa for all measurements. The results of these measurements are shown in table 4.2.

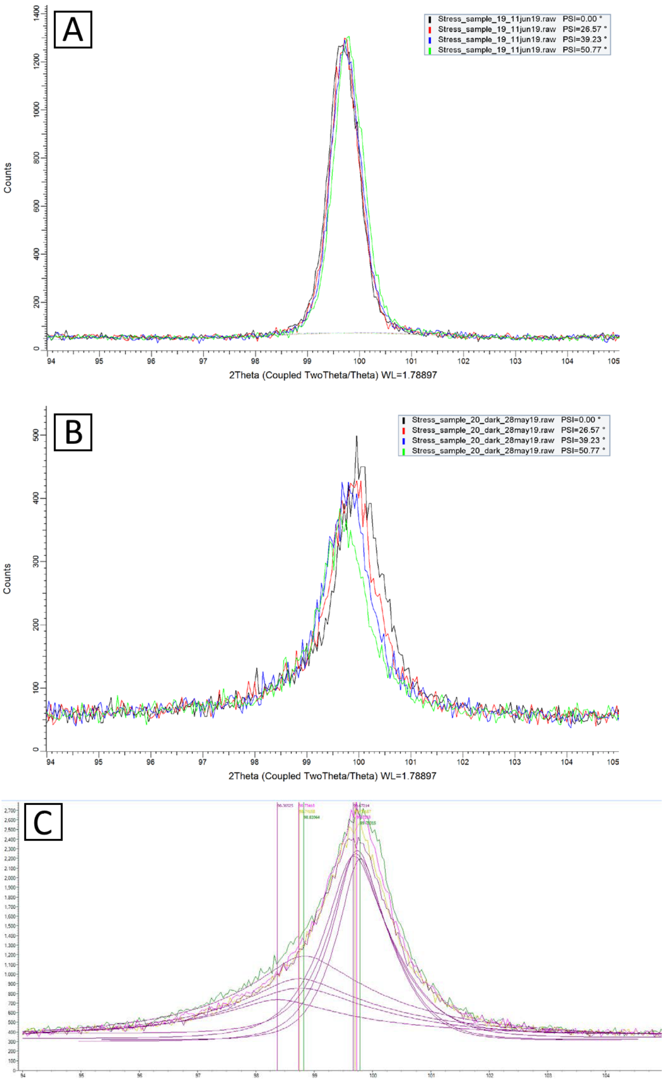

Figure B2.4: *The shift in $\{100\}$ 2θ peak position for the original MHH (a), the ground band (b) and secondary running band (c). The latter peak required fitting with two Pearson VII functions to account for the asymmetry caused by the a and c peaks of the orthorhombic martensite lattice.*